Propagation of ultrashort light pulses in tapered fibers and photonic crystal fibers

Dissertation

zur

Erlangung des Doktorgrades (Dr. rer. nat)

der

Mathematisch-Naturwissenschaftlichen Fakultät

der

Rheinischen Friedrich-Wilhelms-Universität Bonn

vorgelegt von

Rui Zhang

aus

Harbin, V. R. China

Bonn, Germany, 2006

Angefertigt mit Genehmigung der Mathematisch-Naturwissenschaftlichen Fakultät
der Rheinischen Freidrich-Wilhelms-Universität Bonn

First Referent: Prof. Dr. H. Giessen

Second Referent: Prof. Dr. J. Kroha

Tag der Promotion: 11 August 2006

Abstract

In this dissertation we studied the propagation characteristics of tapered fibers and photonic crystal fibers.

This thesis starts with the basic principles of linear and nonlinear optics, which are used to explain the generation mechanisms of supercontinuum radiation. Using a split-step Fourier method, the nonlinear Schrödinger equation is solved to simulate the spectral and temporal properties of the supercontinuum generation.

We simulated the evolution of the transverse intensity distribution, the nonlinear parameter γ, and the GVD of the fiber mode in the taper transition region of a tapered fiber. A complete model of propagation characteristics in tapered fibers was constructed.

In the design to tailor the group velocity dispersion of tapered fibers, we immersed the fibers in transparent liquids (such as acetonitrile, pentane, hexane, and liquid Series AAA from Cargille Labs). Spectrum simulations demonstrate that such a tapered fiber is capable to generate a supercontinuum with an extremely broadened spectrum, ranging from 700 nm to 2000 nm.

We designed a tapered fiber with elliptical cross section in the waist region, which maintains an incident linear polarization state throughout the propagation path and generates a highly polarized supercontinuum. The birefringence and group velocity dispersion as a function of wavelength of the fiber were calculated by using Mathieu functions.

We designed a new nonlinear fiber to generate supercontinuum radiation with dramatically broadened spectrum by filling a highly nonlinear liquid into hollow photonic crystal fibers. The liquid-core photonic crystal fiber with carbon disulfide

and nitrobenzene filled into the core exhibits an extremely high nonlinear parameter γ, which can be more than 20 times larger than that of a conventional PCF. Simulation shows that the spectrum generated by this new nonlinear fiber ranges from 700 nm to more than 3000 nm. In order to accomplish this task, we had to determine a complete quantitative response function in the femtosecond and picosecond regime for the first time.

List of Publications:

Scientific Journals

1. R. Zhang, J. Teipel, X. Zhang, D. Nau, and H. Giessen, "Group velocity dispersion of tapered fibers immersed in different liquids," Opt. Express **12**, 1700-1708 (2004).
2. R. Zhang, X. Zhang, D. Meiser, and H. Giessen, "Mode and group velocity dispersion evolution in the tapered region of a single-mode tapered fiber," Opt. Express **12**, 5840-5849 (2004).
3. R. Zhang, J. Teipel, and H. Giessen, "Theoretical design of a liquid-core photonic crystal fiber for supercontinuum generation," Opt. Express **14**, 6800-6813 (2006).
4. R. Zhang and H. Giessen, "Polarization maintaining tapered fiber," submitted (2006).

Conferences

1. R. Zhang, S. Pricking, X. P. Zhang, and H. Giessen, "Mode and group velocity dispersion evolution in the tapered region of a single-mode tapered fiber," Frühjahrstagung der DPG Berlin 2005 [talk Q 15.2].
2. S. Pricking, R. Zhang, D. Türke, and H. Giessen, "Group velocity dispersion measurements of tapered fibers immersed in different liquids," Frühjahrstagung der DPG Berlin 2005 [talk Q 15.1].
3. R. Zhang, J. Teipel, D. Türke and H. Giessen, "Generation of white light laser radiation in tapered fibers," Photon. West 2006, San Jose, California, USA [invited talk 6101A-83].
4. R. Zhang, J. Teipel, and H. Giessen, "Supercontinuum Generation using a Liquid-core Photonic Crystal Fiber," Frühjahrstagung der DPG Frankfurt 2006 [talk Q 55.2].
5. R. Zhang and H. Giessen, "Polarization maintaining tapered fiber," Frühjahrstagung der DPG Frankfurt 2006 [talk Q 55.5].
6. R. Zhang, J. Teipel, D. Türke and H. Giessen, "White light generation in tapered fibers: basic research and applications," Photon. Europe 2006, Strasbourg, France [invited talk 6190-12].

Contents

Section 1 Introduction

Supercontinuum generation has become a very active research topic over the last few years [1-5], describing the generation of broadband white light by launching an ultrashort pulse through a nonlinear medium. High nonlinear effects occurring in the medium lead to the conversion of the one-color input pulse to multicolor generation. Since its discovery in the late 1960s by Alfano [6], supercontinuum (SC) generation has found numerous technological applications in optical coherence tomography, spectroscopy, pump-probe measurements, optical frequency metrology, and so on [7-11]. The applications take advantage of the unique properties of the generated supercontinuum: it has a dramatically broadened spectrum with a small beam divergence as good as that of a monochromatic laser beam and simultaneously has a short coherence length comparable with a light bulb [12]. Fibers, due to its small beam divergence, high brightness, and low requirement for pulse energies, become one of the most topical appliances to generate a supercontinuum.

The most common fibers, which are used to produce supercontinuum, are photonic crystal fibers (PCFs) (also called holey fiber, hole-assisted fiber, or microstructured fiber) [13-18] and tapered fibers [1,2,19-24]. The photonic crystal fiber was first demonstrated by P. Russell in 1996. It consisted of a hexagonal lattice of air holes in a silica fiber, with a central pure silica core where light is guided. In 2000, J. K. Ranka et al. for the first time employed photonic crystal fibers to generate a supercontinuum, the spectrum of which ranges from 500 nm to 1600 nm [16]. A tapered fiber can be fabricated by drawing a conventional telecommunication fiber over a moving flame. It consists of a narrow waist region, with a diameter of several micrometers or even sub-micrometers, connected on both sides by the fibers, whose diameters increase gradually. The supercontinuum is generated in the waist region. T. Birks et al. for the first time realized supercontinuum generation in a tapered fiber in the year 2000.

Supercontinuum generation is a complex nonlinear phenomenon, and the mechanisms behind SC generation arise from the interaction between dispersion and nonlinear effects. The dispersion is generally categorized as material dispersion and waveguide dispersion. The origin of material dispersion, on a fundamental level, relates to the characteristic resonance frequencies at which the fiber material absorbs the electromagnetic radiation through vibrational modes of electrons [25]. The waveguide dispersion is caused by the dependence of the phase and group velocities

on core radius, numerical aperture, and wavelength [26]. Nonlinear effects include self-phase modulation [27-29], four wave mixing [30-33], cross phase modulation [34-37], stimulated Raman scattering [32,38-40], and so on. The nonlinear effects are induced by changes in the refractive index when intense pulses propagate through the nonlinear medium. The first physical explanation on the initial stage to generate supercontinua was discovered by A. V. Husakou, *et al*. in 2001 [41]. They demonstrated that soliton splitting is the main process leading to the generation of supercontinuum [41-43]. G. Genty et al. presented a further description of the generation mechanism in 2004, demonstrating that the stimulated Raman scattering plays an important role during soliton splitting, and explaining how cross-phase matching shifts the dispersive waves in the visible region further towards the blue [40] [35].

Due to the complexity of supercontinuum generation, numerical simulations of the pulse-propagation characters along the fiber become indispensable to analyze the generation mechanisms and to design a proper fiber structure for a certain application. In 2002, J. M. Dudley et al. presented numerical simulations for the supercontinuum generation and its coherence properties by solving the nonlinear Schrödinger equation [44]. The nonlinear Schrödinger equation, derived from the Maxwell equations, is well suited for studying broad-band pulse propagation problems and can be numerically solved by the split-step Fourier method [25] [45,46].

To generate the supercontinuum radiation, two prerequisites should be satisfied. First, the optical power density should be high enough to excite nonlinear effects in the fiber material, which depend on higher orders of the electric field of the light. This condition can be realized by focusing the incident pulse into small-area fibers, such as photonic crystal fibers and tapered fibers. Secondly, the fiber should be pumped in the anomalous dispersion regime, where blue light travels faster than red. This can be realized by design of the fiber structure and selection of the pumping wavelength.

Many publications focus on supercontinuum generation in photonic crystal fibers (PCFs) since it is easy to design their group velocity dispersion (GVD) and possible to fabricate photonic crystal fibers with long interaction length. However, tapered fibers also show a large potential to become a competitor to photonic crystal fibers due to their long-term stability and simple manufacturing process [1,2]. Recently, the group velocity dispersion in tapered fibers was tailored by immersing the fiber into chemical liquids [19,24], and the interaction length in tapered fibers can

be increased by slicing together several fibers. These progresses make tapered fiber very suitable for the construction of white light sources.

In this dissertation, the principle of white light generation in tapered fibers and photonic crystal fibers with incident pulse durations in the femtosecond range will be discussed. I will also demonstrate some new technologies to design and improve the spectral characteristics of supercontinuum generation.

I start with the basic principles of pulse propagation in normal fibers in section 2.1 by introducing optical communication, fiber classification, fiber parameters, material and doping, dispersion characteristics, and fiber loss.

In section 2.2, the properties, fabrication process, and experimental setup of tapered fibers are discussed. Tapered fibers offer the possibility to achieve supercontinuum generation with initial peak intensities that are two orders of magnitude lower than that required in common optical fibers.

In section 2.3, I will review the principles of linear optics in tapered fibers, the origin of which is relative to the disturbance of the internal charge distribution of atoms. The exact eigenvalue equation, which describes the propagation characteristics in tapered fibers, is discussed in connection with the classical mathematical description of electrodynamics. Leakage power into the air when the pulse propagates in the tapered fiber is also presented.

In section 2.4, I will discuss the nonlinear processes in the waist region of tapered fibers, which induce the mechanisms responsible for the supercontinuum generation. The deviation of the nonlinear pulse-propagation equation, which governs propagation of optical pulses in nonlinear dispersive fibers, is presented. I will also introduce the fundamentals of several nonlinear optical effects, such as self-phase modulation, optical solitons, cross phase modulation, four wave mixing, and Raman inelastic scattering.

In section 2.5, I will introduce the split-step Fourier method, which is applied to theoretically study the pulse-propagation problem. The implementation of this method is discussed in detail. The numerical simulations on the supercontinuum generation are compared with experimental results. I found that simulations can not only adequately model the width of the generated spectrum, but also precisely predict the positions of distinct spectral peaks.

In section 2.6, I will discuss physical mechanisms during supercontinuum generation are discussed in detail. The initial stage of supercontinuum is induced by a soliton splitting generate red-shifted Raman solitons and dispersive waves in the

visible region. Soliton self-frequency shift, cross phase modulation, and four wave mixing lead to further broadening.

In section 3, the propagation characteristics in the taper transition region, where the diameter is varying along the fiber, are presented by solving the scalar equation and the full vector Maxwell equation. I will also describe the evolution of the radial distribution of the light intensity, the nonlinear parameter, and the group velocity dispersion. Knowing the propagation characteristics in the taper transition region, I build a complete model of light propagation and nonlinear interaction processes in tapered fibers.

In section 4, I demonstrate a considerably simple way to control the group velocity dispersion (GVD) characteristics of a tapered fiber. I fill the environment of the tapered fiber with a selected chemical liquid which provides a suitable refractive index. The tapered fiber immersed in liquids possesses favorable group velocity dispersion properties in the anomalous dispersion region. The spectral simulation demonstrates that such a fiber is capable to generate a supercontinuum with a dramatically broadened spectrum due to the dual zero dispersion wavelengths lying in the near infrared region.

In section 5, I designed a tapered fiber with elliptical cross section in the waist region, which maintains an incident linear polarization state throughout the propagation path and generates a highly polarized supercontinuum. A supercontinuum with linear polarization state can find application in CARS microscopy, OPO systems, gas sensors, *etc*, which are hard to construct from conventional tapered fibers. The propagation constant and group velocity dispersion were calculated based on the Maxwell equations using Mathieu functions. The zero dispersion wavelength of the odd dominant mode is located at a larger wavelength than that of the even dominant mode.

In section 6, I will show the new design of a high nonlinear fiber by filling the core a hollow-core photonic crystal fiber with highly nonlinear liquids, such as carbon disulfide and nitrobenzene. The fiber is shown to have an extremely high nonlinear parameter γ in the order of 2.45 /W/m. The group velocity dispersion curve of the fiber exhibits an anomalous dispersion in the near infrared, and its zero-dispersion wavelength is around 1.55 μm in the telecommunication window. This leads to potentially significant improvements and a large bandwidth in supercontinuum generation. The spectral properties of the supercontinuum generation in liquid-core photonic crystal fibers are simulated by solving the nonlinear Schrödinger equation.

The results demonstrate that the liquid-core PCF is capable to generate dramatically broadened spectra in a range from 700 nm to 3000 nm.

Section 2 Supercontinuum generation in tapered fibers

2.1 Pulse propagation in common telecommunication fibers

The research on optical fiber is one of the most interesting and important topics in the field of global and local communication systems [47]. A basic fiber communication system primarily consists of the following components: a transmitting device, which generates the light signal; an optical fiber, which carries the light beam loaded with information; a number of repeaters, which boost the signal strength to overcome the fiber losses; and a receiver, which accepts the light signal transmitted, as shown in Figure 2.1.1.

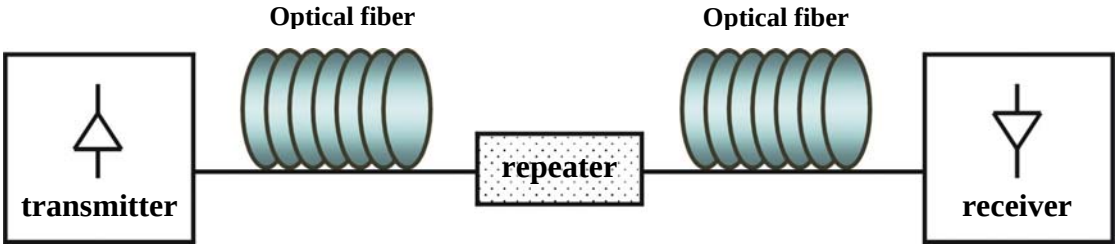

Fig. 2.1.1. Typical fiber optical fiber communication system, which consist of an optical transmitter (laser diode or LED), the transmission medium (optical fibers), a repeater and an optical receiver (photodetector). The light is launched through the link.

As the heart of a communication system, optical fibers have been paid a great attention to. Generally, an optical fiber is made of a central dielectric core of a high refractive index, a cladding with a lower refractive index, a buffer and a jacket, as shown in Figure 2.1.2. Such a fiber is known as step-index fibers, as opposed to graded-index fibers, where the core refractive index decreases gradually from the center [48]. For the purpose of low-loss transmission and easy fabrication, pure silica glass synthesized by fusing SiO_2 molecules is generally chosen as the material of optical fibers.

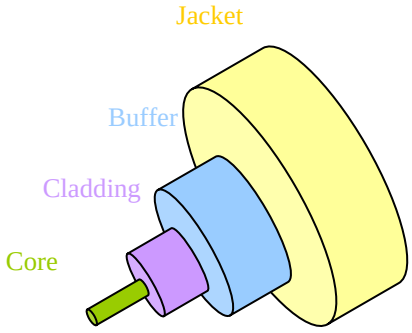

Fig. 2.1.2 A typical single mode fiber, which consist of core, cladding, buffer and jacket.

The optical fibers as transmission media have developed and improved rapidly over the last few years. Compared with traditional communication system, optical fibers possess the following advantages [47]:

(1) *Wide transmission bandwidth.* The principal material in fiber fabrication is fused silica, whose optical carrier wavelengths are between 0.8 μm and 1.65 μm. This property makes a fiber possible to support a wide transmission bandwidth (0.1-1000 GHz). With such a large potential of its capacity, optical fiber becomes irreplaceable in the field of communication system.

(2) *Long distance signal transmission*. The low attenuation and superior signal integrity found in optical systems allow much longer intervals of signal transmission than electronic systems. With the development of the fiber fabrication, the loss of the glass fibers nowadays have been reduced to 0.15 dB/km in the telecom window around 1.55 μm.

(3) *Impervious to electromagnetic interference*. The fiber communication system is hardly influenced by external electric or magnetic fields, and immune to radiation outside of the fibers, which prevents the system from corruption of data and avoids to produce electromagnetic pollution.

In this chapter, basic characteristics of the pulse propagation in optical fibers are introduced. In section 2.1.1 I deal with the classification of optical fibers and some important fiber parameters. Section 2.1.2 introduces the material and doping, which are selected to be transparent at optical frequencies. Section 2.1.3 discusses the characteristics of chromatic dispersion in step index optical fibers because of its importance in the nonlinear effect with ultrashort incident pulse. Section 2.1.4 describes the mechanisms responsible to the fiber loss, which relate to a wide range of intrinsic material and to fiber manufacturing properties.

2.1.1 Classification of optical fibers and fiber parameters

Generally, optical fibers are classified into two types: the single-mode fiber (SMF) and the multimode fiber (MMF) [48]. A SMF can support only the lowest order propagating mode (fundamental mode) at the wavelength of interest. It is used to guide light for long-distance telephony and multichannel television broadcast systems. The refractive index profiled of a SMF is usually a step-index type. Multimode fiber, through which numerous modes or light rays simultaneously propagate, is used to guide light for short transmission distances, such as in LAN systems and video surveillance.

To specifically describe optical fibers, some parameters, which affect the communication system's operation, are designed as follows: [49].

(i) n_1 and n_2 are the refractive indices of the core and cladding (see figure 2.1.3).

The refractive-index difference between the core and the cladding Δ, which is realized by the different use of dopants, such as GeO_2 and P_2O_5, can be defined as: $\Delta = \frac{n_1 - n_2}{n_1}$.

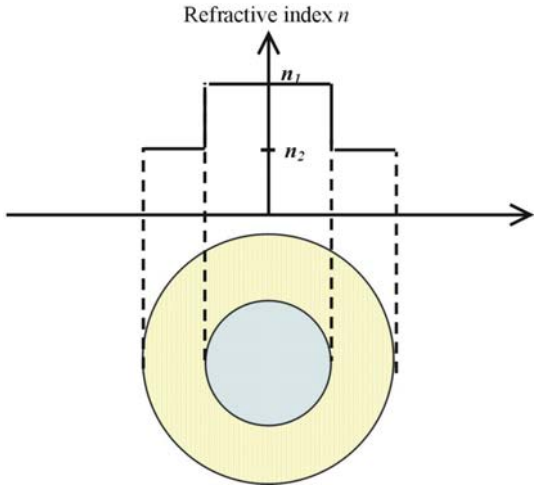

Fig. 2.1.3 Refractive index distribution of a step-index optical fiber

(ii) *V*, the so called normalized frequency, is the parameter to determine the number of modes supported by the fiber, defined as

$$V = \frac{2\pi}{\lambda} r \sqrt{n_1^2 - n_2^2}\,, \tag{2.1.1}$$

where r is the radius of the core, λ is the free-space wavelength of the light source. For a step-index fiber, only the lowest order mode (fundamental mode) propagates in the fiber if V is smaller than 2.405. Optical fibers designed to satisfy this condition are called single- mode fibers. The critical value of the *V*-parameter 2.405 is determined by solving the Maxwell equation in optical fibers.

(iii) Numerical aperture *NA*, which is a measure of the light gathering power of the optical fiber, can be defined by the following equation:

$$NA = \sqrt{n_1^2 - n_2^2}\,. \tag{2.1.2}$$

It can be considered as representing the size or "degree of openness" of the input acceptance cone, the half angle of which is θ, as shown in Figure 2.1.4. If $sin\theta$ is smaller than the numerical aperture *NA*, the incident light will be guided through the fiber. The value of numerical aperture lies between 0 and 1. With a numerical aperture of 0, the fiber gathers no light and with a numerical aperture of 1, the fiber gathers all the light that falls onto it.

(iv) Attenuation α represents the reduction of signal strength during transmission and mathematically it is given by

$$\alpha = -\frac{10}{L}\log(\frac{P_T}{P_0}), \tag{2.1.3}$$

in units of dB/km (decibel units), where P_{int} is the power launched at the input end of a fiber with length L and P_{out} is the transmitted power. Nowadays fused silica fibers have losses of less than 0.15 dB/km at 1.55 μm, corresponding to more than 97% transmission over 1 km. The mechanisms responsible for the attenuation are the material absorption and Raleigh scattering dominantly. We discuss the loss mechanisms in detail in Section 2.1.3. When it is necessary for an optical fiber to guide light over long distances, a series of repeaters are used to overcome attenuation. The repeaters, which are inserted along the length of fiber, boost the pulse intensity to reconstruct it to its original quality.

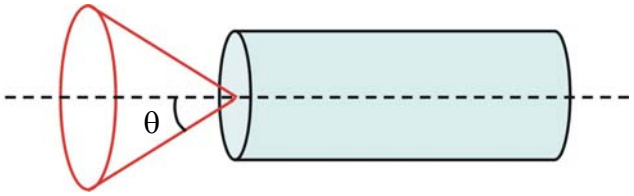

Fig. 2.1.4 Illustration of acceptance angle related to numerical aperture NA

2.1.2 Material and doping

The materials, which are used to make optical fibers, should be transparent to optical frequencies and inexpensive in fiber fabrication. And in the case of long-range communication they should make possible repeater separation distances on the order of kilometers. Pure silica glass synthesized by fusing SiO_2 molecules is found to satisfy the requirements above. Besides those advantages, fused silica is of negligible thermal expansion, excellent thermal shock resistance and good chemical inertness, which make it easier to work with.

The refractive index difference between the core and the cladding is realized by doping the core material with dopants such as GeO_2 and P_2O_5 [25], the refractive indices of which are larger than that of pure silica, and doping the cladding with materials such as boron and fluorine, which decreases the refractive index of pure silica. The amount of dopants added to the fiber must be taken into account in the designation of an optical fiber for different purposes. More dopants in the core of fiber result in higher refractive index difference and stronger compositional fluctuations. For example, for the purpose to design a long-haul transmission fiber, the higher refractive index difference, which increases the numbers of guiding modes along the

fiber, leads to higher group delay and reduces output intensity, and the stronger compositional fluctuations increase the fiber loss through the dopants scattering.

2.1.3 Fiber loss mechanisms

The mechanisms which contribute to the loss in an optical fiber can be categorized as intrinsic, extrinsic and, radiative losses [25,50].

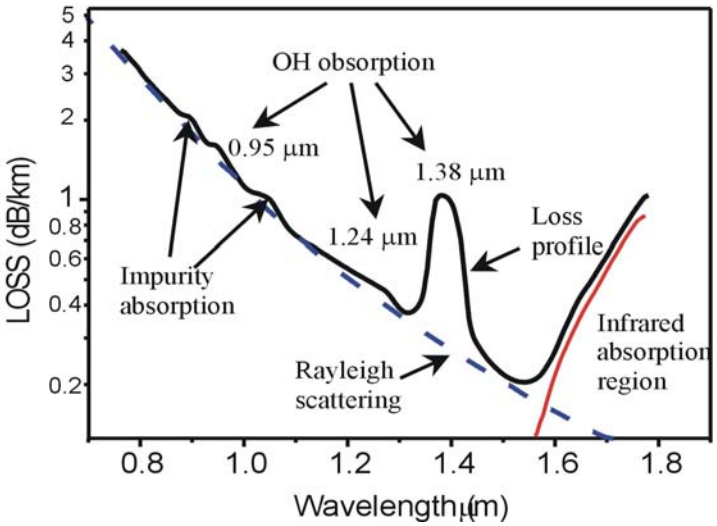

Fig. 2.1.5 Measured loss spectrum (black solid) of a single mode silica fiber. The blue dashed curve shows the contribution resulting from Rayleigh scattering, and the red solid curve illustrate the loss profile arising from infrared absorption

Intrinsic losses can be further subdivided into infrared absorption and Rayleigh scattering in the wavelength regions of interest to optical communication. Infrared absorption arises from the interaction of the light with the components of the glasses used in fiber manufacture. For silica fiber, the lattice vibrational modes of silicon-oxygen bonds produce absorptive resonances between 7 and 11 μm, which, due to the anharmonic coupling between those modes, further generate an infrared absorption tail extending into the transmission wavelength region. Rayleigh scattering arises from the composition and density fluctuations of the fiber material during manufacture. The resulting inhomogeneous refractive index scatters light in all directions. The loss due to Rayleigh scattering is proportional to $1/\lambda^4$, where λ is the wavelength of the propagating lightwave. The addition of dopants into the fiber results in higher inhomogeneities in the refractive index distribution, which increases the Rayleigh scattering loss. Figure 2.1.5 shows the measured loss spectrum of a single-mode silica fiber [4,25]. Fiber losses increase rapidly as wavelength decreases and reach a level of a few dB/km in the visible region, which is caused by the Rayleigh scattering. The absorption at wavelengths longer than 1.6 μm comes from infrared absorption by

silicon-oxygen bonds in the glass; as the plot shows, the absorption increases sharply with longer wavelengths in the near infrared. As a result, silica-based fibers are rarely used for communications at wavelengths longer than 1.65 μm. The rapid decrease in scattering at longer wavelengths makes minimum value of loss about 0.2 dB/km near 1.55 μm, where both Rayleigh scattering and infrared absorption are low.

Extrinsic absorption arises generally from the presence of transition metal ions impurities and OH ions dissolved in glass [25]. All of them have strong absorption in the visible and near infrared region, therefore, their concentration should be reduced to a low level so that they contribute negligibly to the fiber loss.

Radiative losses, relative to the waveguide structure, arise fundamentally from geometrical irregularities, bending losses, microbending losses, and defects at joints between fibers, which couple the guided modes with the radiation modes propagating in the cladding [50]. The geometrical irregularities introduced in fiber manufacture include core-cladding interface irregularities, diameter fluctuations and so forth. Bending loss occurs if the fiber is not absolutely straight. Microbending losses are induced in the process of jacketing, where the fiber is subjected to microscopic deviations of the fiber axis from the straight condition. Defects at joints arise from the mismatch of the mode field intensity distribution when coupling light into a fiber. With careful design and fabrication, all of the radiative losses can be reduced to small value.

2.1.4 Dispersion

Pulse dispersion is one of the factors which limit the information-carrying capacity of a fiber communication system. A laser pulse, which is even considered as monochromatic, actually contains a continuum of wavelengths in a small range. Each frequency components of the pulse travels at different velocity given by $c/n(\lambda)$, which results in the pulse-broadening in the time domain (expression of $n(\lambda)$ shown in Eq. (2.1.4)). The mechanisms responsible for the dispersion are generally categorized as material dispersion and waveguide dispersion.

The origin of material dispersion, which leads to the refractive index variations with wavelength, on a fundamental level, relates to the characteristic resonance frequencies at which the fiber material absorbs the electromagnetic radiation through vibrational modes of electrons. Far from the material resonances, the refractive index of doped silica can be approximated by the following Sellmeier equation [51]:

$$n^2(\lambda) - 1 = \sum_{j=1}^{3} \frac{A_j \lambda^2}{\lambda^2 - \lambda_j^2}, \tag{2.1.4}$$

where λ is the wavelength in unit mm, λ_j represents the resonance wavelength and A_j is the strength of jth resonance. The sum in Eq. (2.1.4) takes into account all material resonances that contribute to dispersion. The corresponding values of the coefficients λ_j and A_j for different doped silica fiber are shown in Table 2.1.1 [51].

Fibers	Dopant (%)	λ_1^2	λ_2^2	λ_3^2	A_1	A_2	A_3
1	Pure silica	0.004679148	0.01351206	97.93400	0.6961663	0.4079426	0.8974794
2	GeO_2 (6.3)	0.007290464	0.01050294	97.93428	0.7083952	0.4203993	0.8663412
3	GeO_2 (19.3)	0.005847345	0.01552717	97.93484	0.7347008	0.4461191	0.8081698
4	B_2O_3 (5.2)	0.004981838	0.01375664	97.93353	0.6910021	0.4022430	0.9439644
5	B_2O_3 (10.5)	0.005202431	0.01287730	97.93401	0.7058489	0.4176021	0.8952753

Table 2.1.1. Values of coefficients in Sellmeier equation for different doped silica fiber

The waveguide dispersion, which can occur in the absence of any material dispersion, is caused by the dependence of the phase and group velocities on core radius, numerical aperture, and wavelength. The waveguide dispersion relating to the fiber structure can be calculated by solving the eigenvalue equation of the propagating mode in the fiber, which is discussed in detail in Section 2.3.2.

2.2 Introduction of tapered fibers

White light continuum generation using femtosecond and picosecond laser pulses has many applications in optical coherence tomography, spectroscopy, pump-probe measurements, optical frequency metrology, and so on [7-11]. To generate supercontinuum sources, highly nonlinear optical effects are indispensable, and therefore very high optical power densities (Gigawatts/cm^2) are required. This can be realized by focusing the incident pulse on small-area fibers, such as photonic crystal fibers [13-18] and tapered fibers [1,2,19-24], which offer the possibility to form a supercontinuum with initial peak intensities two orders of magnitude lower than that required in normal optical fibers.

Supercontinuum generation in photonic crystal fibers (PCF) is currently a very topical issue. Tapered fibers as nonlinear elements to generate white light radiation are used less frequently, because there are two seemingly disadvantageous facts [2]. First, a suitable group velocity dispersion (GVD) design is more complicated than in PCFs. Second, the tapering process restricts the interaction length of the fiber [2] to several ten centimeters. Recently, the group velocity dispersion in tapered fibers was tailored by immersing the fiber with chemical liquids [19,24], and the interaction length in tapered fibers was increased by slicing several fibers [52]. Those progresses make tapered fiber a very cheap and convenient source for the generation of white light.

In this section, the general characteristics of tapered fibers are discussed. Section 2.2.1 introduces the fabrication process and the fiber profile of tapered fibers. In section 2.2.2, we are going to show the experimental setup used to generate supercontinuum sources and the spectral properties of the output generated by the tapered fibers.

2.2.1 Fabrication

We used single-mode Corning SMF28 quartz fibers in a home-built fiber-drawing rig. The fibers were drawn over a moving propane-butane-oxygen flame with a temperature close to the melting point of quartz. The fabrication machine is shown in Fig. 2.2.1. H1 and H2 represent the fiber mounts and Br is the burner. M1 and M2 are used to move fiber mounts, and M3 is used to move burner.

The tapered fibers consisted of three parts: untapered region, taper transition region, and waist region as shown in Fig. 2.2.2. The thick untapered regions make it possible to couple the light into tapered fibers conveniently. In the taper transition

region, the outer diameter decreased from 125 micrometers to a few micrometers. The waist region has a constant diameter, ranging from 4 μm to only 0.5 μm. Due to the pulse being focused on such a small area, the guiding mode obtains an extremely huge peak intensity, which leads to the formation of the supercontinuum. Variation of the drawing velocity allowed us to control the diameter of the waist in a very reproducible way.

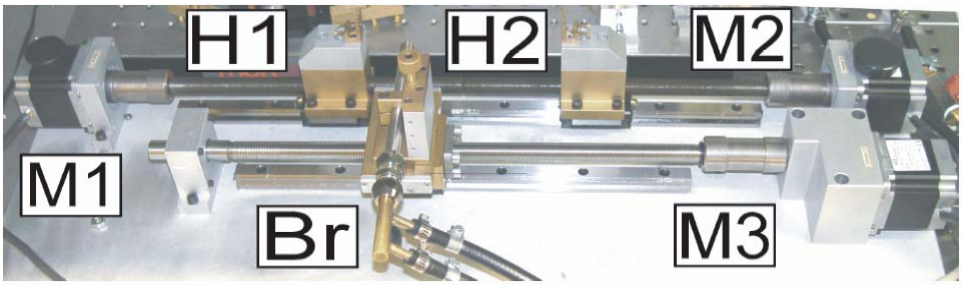

Fig. 2.2.1 Fabrication machine, where H1 and H2 are the fiber mounts and Br is the burner. M1 and M2 are used to move fiber mounts and M3 is used to move burner.

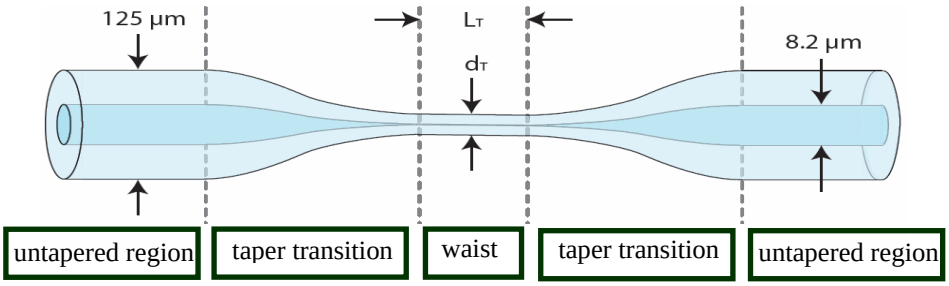

Fig. 2.2.2 Structure of a tapered fiber, which consists of three parts: untapered region, taper transition region, and waist region.

2.2.2 Experimental setup and the supercontinuum generation [2]

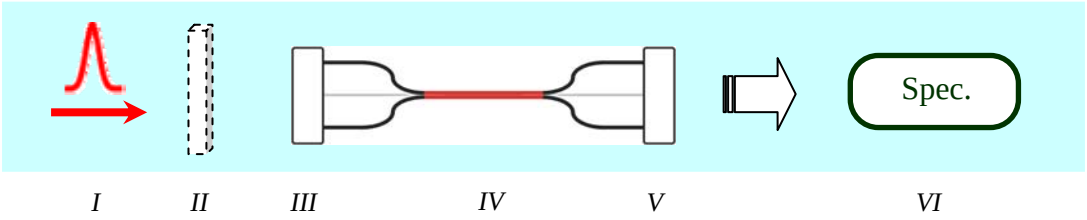

Fig. 2.2.3 Experiment setup. (*I*) Input pulse, (*II*) Faraday isolator, (*III*) Input coupling, (*IV*) Tapered fiber, (*V*) Output coupling, and (*VI*) Spectrometer.

The experiment setup to generate supercontinuum sources consists of input coupler, a tapered fiber, an output coupler, and a spectrometer, as shown in Fig. 2.2.3. Generally, a Faraday isolator is used to prevent back reflections from the fiber into the laser. When both ends of a tapered fiber are carefully cut to avoid unsmooth surfaces, and the input coupling is well adjusted to optimize the pulse propagation, the output power can be as high as 40-60% of the input power.

The generated supercontinuum depends on the pump wavelength, the fiber waist diameter, the input pulse duration, and so on. Figure 2.2.4 shows the spectra of the supercontinuum generation after five tapered fibers, which are of different diameters but pumped at the same wavelength 800 nm [2]. It is evident that the spectra are broadened when the diameter decreases but the dip in the visible region becomes larger as shown by the spectra of the fibers with waist diameter of 2.3 μm and 2.5 μm. The fiber with 2.8 μm waist does not generate a supercontinuum. The explanation for such features is caused by the solitonic generation mechanisms, which will be discussed in detail in section 2.6.

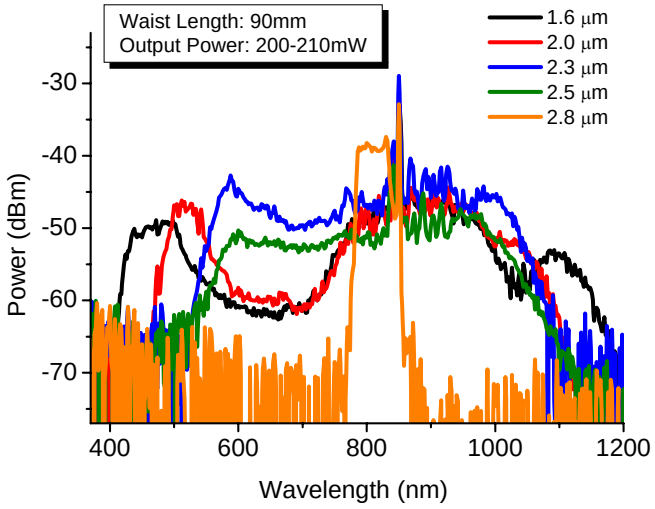

Fig. 2.2.4 The spectra of the supercontinuum generation after the tapered fibers with diameter of 1.6 μm (black), 2.0 μm (red), 2.3 μm (blue), 2.5 μm (green), and 2.8 μm (orange).

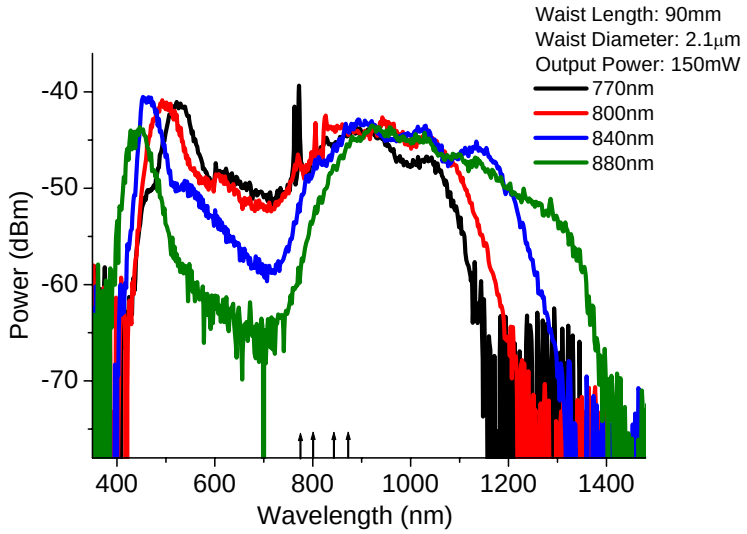

Fig. 2.2.5 The spectra of the supercontinuum generation after one tapered fiber with pumping wavelength of 770 nm (black), 800 nm (red), 840 nm (blue), and 880 nm (green).

Figure 2.2.5 shows the spectra of the supercontinuum generation after one tapered fiber, which has a waist diameter of 2.1 μm, but is pumped at different wavelengths of 770 nm, 800 nm, 840 nm, and 880 nm [2]. The figures demonstrate that pumping a tapered fiber with a higher input wavelength leads to a broadened spectrum and a widened dip in the visible region. A physical explanation on this spectral feature can be found in section 2.6.

2.3 Principles of linear optics in tapered fibers

To understand the nonlinear phenomena behind the supercontinuum generation, it is necessary to review the theory of electromagnetic waves consisting of electric and magnetic fields. The total polarization induced by the optical pulse contains linear and nonlinear parts. In this chapter, I concentrate on the discussion on linear optics in tapered fibers.

On fundamental level, the origin of the linear polarization is relative to the disturbance of the internal charge distribution of atoms [53]. If the energy of the photons launched into the fiber is small, the photon leads only to a linear displacement of the internal charges, which will be accelerated depending on the intensity of the incident light wave. The accelerated charges emit sources of electromagnetic waves, which interfere with the original wave. The waves induced by the molecules have the same frequency or energy as the external wave, only with a different phase or momentum. This nonresonant possibility is the origin of every kind of linear optical effect, which causes reflection, diffraction, scattering, and so on.

In this chapter, the basic principles of linear optics in tapered fibers are introduced. Section 2.3.1 discusses the classical mathematical description of electrodynamics, the Maxwell equation. In section 2.3.2 we deal with the exact eigenvalue equation, derived from the Maxwell equation, which describes the propagation characteristics in tapered fibers. Section 2.3.3 discusses the fractional leakage power in the air when the pulse propagates in the fiber.

2.3.1 Maxwell equation

Every kind of electromagnetic wave can be described by the electric field vector **E**, the electrical displacement **D**, the magnetic field vector **H**, and the magnetic flux density **B**. The relationship among the four field vetors, named Maxwell equation, was derived by James Clerk Maxwell (1831-1879) as follows [25,54]:

$$\nabla \times \mathbf{E} = -\frac{\partial \mathbf{B}}{\partial t}, \tag{2.3.1-a}$$

$$\nabla \times \mathbf{H} = \mathbf{J} + \frac{\partial \mathbf{D}}{\partial t}, \tag{2.3.1-b}$$

$$\nabla \cdot \mathbf{D} = \rho_f, \tag{2.3.1-c}$$

$$\nabla \cdot \mathbf{B} = 0, \tag{2.3.1-d}$$

where, **J** is the current density, ρ_f is the carrier density, and **∇** is the Nabla operator. In the absence of free charges in a medium such as optical fibers, **J** and ρ_f are equal to zero.

For a nonmagnetic medium such as optical fibers, the flux densities **D** and **B** arising in response to the electric and magnetic fields **E** and **H,** can be written as:

$$\mathbf{D} = \varepsilon\mathbf{E} = \varepsilon_0\mathbf{E} + \mathbf{P}$$

$$\mathbf{B} = \mu_0\mathbf{H}\,, \tag{2.3.2}$$

where ε_0 is the vacuum permittivity, μ_0 is the vacuum permeability, and **P** is the induced electric polarizations.

The wave equation for the electric field can be derived as the following equation by first taking the curl of Eq. (2.3.1-a) and then substituting Eq. (2.3.1-c) into the result.

$$\nabla \times \nabla \times \mathbf{E} = -\frac{1}{c^2}\frac{\partial^2\mathbf{E}}{\partial t^2} - \mu_0\frac{\partial^2\mathbf{P}}{\partial t^2}, \tag{2.3.3}$$

where c is the speed of light in vacuum and $\mu_0\,\varepsilon_0\,c^2$=1. In the treatment of the linear effect in a medium, we describe the relation between the induced polarization **P** and the electric field **E** through the electric susceptibility function χ_e:

$$\mathbf{P} = \varepsilon_0\chi_e\mathbf{E}\,. \tag{2.3.4}$$

The dielectric constant ε_r and the net permittivity of medium ε are related with the electric susceptibility function χ_e as 1+ χ_e and ε=$\varepsilon_r\varepsilon_0$, respectively. Substitution of these expressions to Eq. (2.3.3) yields

$$\nabla^2\mathbf{E} - \mu_0\varepsilon\frac{\partial^2\mathbf{E}}{\partial t^2} = 0$$

$$\nabla^2\mathbf{H} - \mu_0\varepsilon\frac{\partial^2\mathbf{H}}{\partial t^2} = 0\,, \tag{2.3.5}$$

where the relations $\nabla\times\nabla\times\mathbf{E}=\nabla(\nabla\mathbf{E})-\nabla^2\cdot\mathbf{E}$ and $\nabla\cdot\mathbf{E}=0$ were used (the last relation is valid only in a homogeneous medium).

In the frequency domain, the equations above are transformed into Eq. (2.3.3) as follows using the operator form $\partial/\partial t=i\omega$,

$$\nabla^2\mathbf{E} - k^2\mathbf{E} = 0$$

$$\nabla^2\mathbf{H} - k^2\mathbf{H} = 0\,, \tag{2.3.6}$$

where $k \equiv \omega\sqrt{\mu_0\varepsilon}$ is the wavenumber and ω is the frequency of the light wave. These two equations are the so-called vector Helmholtz equations.

2.3.2 Exact solutions of the eigenvalue equation in tapered fibers

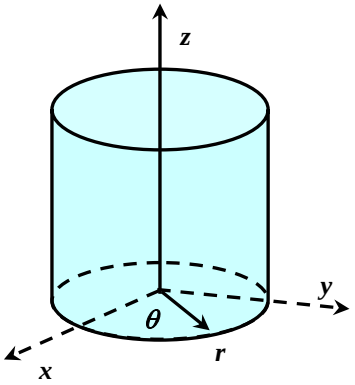

Fig. 2.3.1 The cylinder coordinate (r, ϕ, z).

To solve the Helmholtz equations in tapered fibers oriented along the z axis, we consider the propagating light wave as a forward z-propagating wave in a cylinder coordinate (r, ϕ, z), as in Fig 2.3.1. The variation of the wave with respect to z is described by $\exp(-i\beta z)$, where β, the propagation constant, is equal to the wavenumber k. The phasor form of the electric field can be expressed as

$$\mathbf{E}=\mathbf{E}(r,\phi,z)=\mathbf{E_0}(r,\phi)\exp(-i\beta z), \tag{2.3.7}$$

and $\mathbf{E_0}$ can be further written as the sum of transverse components (E_r and E_ϕ) and longitude component (E_z),

$$\mathbf{E_0}=\mathbf{e_r}E_r+\mathbf{e_\phi}E_\phi+\mathbf{e_z}E_z. \tag{2.3.8}$$

Substituting the expression to Eq. (2.3.6) and expanding the Laplacian operator in cylinder coordinates result in [55]

$$\frac{1}{r}\frac{\partial}{\partial r}\left(r\frac{\partial E_z}{\partial r}\right)+\frac{1}{r^2}\frac{\partial^2 E_z}{\partial \phi^2}+\left(k_0^2n^2-\beta^2\right)E_z=0. \tag{2.3.9}$$

The longitude component of magnetic field H_z can be expressed in the similar form (later on we are not going to discuss the expression of magnetic field in particular since it can be derived in the same way as electric field.)

$$\frac{1}{r}\frac{\partial}{\partial r}\left(r\frac{\partial H_z}{\partial r}\right)+\frac{1}{r^2}\frac{\partial^2 H_z}{\partial \phi^2}+\left(k_0^2n^2-\beta^2\right)H_z=0. \tag{2.3.10}$$

Knowing the refractive index distribution of the tapered fiber, the longitude components E_z and H_z can be achieved with respect to β.

We assume that the solution for E_z is a discrete series of modes, each of which has separated dependences on r, ϕ, and z in product form:

$$E_z=\sum_l R_l(r)\,\Phi_l(\phi)\exp(-i\beta_l z). \tag{2.3.11}$$

Each mode in the expansion must itself be a solution of Eq. (2.3.11). A single mode, $E_z = R(r)\,\Phi(\phi)\exp(-i\beta z)$ can thus be substituted into Eq. (2.3.11) to obtain

$$\frac{r^2}{R}\frac{d^2R}{dr^2}+\frac{r}{R}\frac{dR}{dr}+r^2\beta^2=-\frac{1}{\Phi}\frac{d^2\Phi}{d\phi^2}. \tag{2.3.12}$$

Following the standard derivation by Snyder and Love [55], we obtain the solutions of the longitudinal components in the fiber waist (E_{z1} and H_{z1}) and in the surrounded air (E_{z2} and H_{z2}) as:

In the fiber waist, where $r < a$ (a is the radius of the fiber waist), we get:

$$\begin{pmatrix}E_{z1}\\H_{z1}\end{pmatrix}=\begin{pmatrix}A_1\\B_1\end{pmatrix}J_m(k_c\,r)\begin{pmatrix}\sin m\phi\\\cos m\phi\end{pmatrix} \tag{2.3.13}$$

in the air, where $r > a$, we get:

$$\begin{pmatrix}E_{z2}\\H_{z2}\end{pmatrix}=\begin{pmatrix}A_2\\B_2\end{pmatrix}K_m(k_c\,r)\begin{pmatrix}\sin m\phi\\\cos m\phi\end{pmatrix} \tag{2.3.14}$$

where, $k_c=\sqrt{k_0^2n_{core}^2-\beta^2}$; A_1, B_1, A_2 and B_2 are constants; $J_m(x)$ and $K_m(x)$ are the m^{th} order Bessel function and modified Bessel function, respectively.

All the expressions of transverse components (E_{r1}, H_{r1}, E_{r2}, H_{r2}, $E_{\phi1}$, $H_{\phi1}$, $E_{\phi2}$, $H_{\phi2}$) in the fiber and in the air are found to satisfy the following relationship with the longitudinal components, which are derived from the Maxwell equation.

$$\begin{aligned}
k_c^2E_r&=-i\beta\frac{\partial E_z}{\partial r}-\frac{i\omega\mu_0}{r}\frac{\partial H_z}{\partial\phi}\\
k_c^2E_\phi&=-\frac{i\beta}{r}\frac{\partial E_z}{\partial\phi}+i\omega\mu_0\frac{\partial H_z}{\partial r}\\
k_c^2H_r&=\frac{i\omega\varepsilon_0n^2}{r}\frac{\partial E_z}{\partial\phi}-i\beta\frac{\partial H_z}{\partial r}\\
k_c^2H_\phi&=-i\omega\varepsilon_0n^2\frac{\partial E_z}{\partial r}-\frac{i\beta}{r}\frac{\partial H_z}{\partial\phi},
\end{aligned} \tag{2.3.15}$$

where $k_c^2=\omega^2\mu_0\varepsilon_0n^2-\beta^2=k_0^2n^2-\beta^2$ and $n^2=\varepsilon_r=\dfrac{\varepsilon}{\varepsilon_0}$. Using the boundary conditions [55],

$$E_{z1}=E_{z2},\ H_{z1}=H_{z2},\ E_{\phi1}=E_{\phi2},\ H_{\phi1}=H_{\phi2}\qquad\text{at } r=a, \tag{2.3.16}$$

we can build up a 4×4 homogeneous matrix equation where those constants (A_1, A_2, B_1 and B_2) are the variables. In order to get a set of non-zero solutions for the variables, the determinant of this matrix should be zero.

Following the derivation above, we finally obtain the eigenvalue equation with

respect to propagation constant β, which describes the propagation characteristics in a tapered fiber [55-57]:

$$\left[\frac{J_m'(\kappa a)}{\kappa J_m(\kappa a)}+\frac{K_m'(\gamma a)}{\gamma K_m(\gamma a)}\right]\left[\frac{J_m'(\kappa a)}{\kappa J_m(\kappa a)}+\frac{1}{n^2}\frac{K_m'(\gamma a)}{\gamma K_m(\gamma a)}\right]=\left[\frac{m\beta k_0(n^2-1)}{a\kappa^2\gamma^2 n}\right]^2, \quad (2.3.17)$$

where $\kappa^2=n^2k_0^2-\beta^2$; $\gamma^2=\beta^2-k_0^2$; n is the refractive index of the fiber material. m=1 corresponds to the fundamental mode HE_{11} in the waist region.

2.3.3 Fractional power leakage into the air and its applications

One of the important parameters associated with a fiber is the fractional power carried in the fiber or the manner in which the power is distributed within the structure. The ratio of the power carried in the fiber to the total power that propagates in the mode is expressed as:

$$\eta=\frac{P_{fiber}}{P_{fiber}+P_{air}}. \quad (2.3.18)$$

To calculate the two power quantities (P_{fiber} and P_{air}), we first introduce the concept of time-average power density. The reason that we consider time-average power density instead of instantaneous power density is that most detection equipment cannot response fast enough to follow the oscillating fields. The time-average power density using the electric and magnetic fields in phasor form is given by

$$\langle \mathbf{S} \rangle=\frac{1}{2}\mathrm{Re}\left\{\mathbf{E}\times\mathbf{H}^*\right\}, \quad (2.3.19)$$

where, **S** is the so called Poynting vector.

The expression for power in cylinder coordinates can be further derived as follows:

$$\int_0^a\int_0^{2\pi}\frac{1}{2}\mathrm{Re}\left\{E_rH_\phi^*-E_\phi H_r^*\right\}r\,dr\,d\phi, \quad (2.3.20)$$

where E_r, H_ϕ^*, E_ϕ, and H_r^* can be calculated by Eq. (2.3.15):

In the core,

$$E_{r1}=-\frac{i}{\kappa^2}\left(\beta\kappa A_1J_m'(\kappa r)-\frac{m\omega\mu_0B_1}{r}J_m(\kappa r)\right)\sin(m\phi)$$

$$E_{\phi1}=-\frac{i}{\kappa^2}\left(\frac{m\beta}{r}A_1J_m(\kappa r)-\omega\mu_0\kappa B_1J_m'(\kappa r)\right)\cos(m\phi)$$

$$H_{r1}=\frac{i}{\kappa^2}\left(\frac{\omega\varepsilon_0n^2m}{r}A_1J_m(\kappa r)-\beta\kappa B_1J_m'(\kappa r)\right)\cos(m\phi)$$

$$H_{\phi 1} = -\frac{i}{\kappa^2}\left(\omega\varepsilon_0 n^2 \kappa A_1 J_m'(\kappa r) - \frac{m\beta B_1}{r} J_m(\kappa r)\right)\sin(m\phi), \qquad (2.3.21)$$

in the air,

$$E_{r2} = -\frac{i}{\gamma^2}\left(\beta\gamma A_2 K_m'(\gamma r) - \frac{m\omega\mu_0 B_2}{r} K_m(\gamma r)\right)\sin(m\phi)$$

$$E_{\phi 2} = -\frac{i}{\gamma^2}\left(\frac{m\beta}{r} A_2 K_m(\gamma r) - \omega\mu_0\gamma B_2 K_m'(\gamma r)\right)\cos(m\phi)$$

$$H_{r2} = \frac{i}{\gamma^2}\left(\frac{\omega\varepsilon_0 n^2 m}{r} A_2 K_m(\gamma r) - \beta\gamma B_2 K_m'(\gamma r)\right)\cos(m\phi)$$

$$H_{\phi 2} = -\frac{i}{\gamma^2}\left(\omega\varepsilon_0 n^2 \gamma A_2 K_m'(\gamma r) - \frac{m\beta B_2}{r} K_m(\gamma r)\right)\sin(m\phi), \qquad (2.3.22)$$

with

$$A_1 = \frac{1}{J_m(\kappa a)} \qquad B_1 = \frac{1}{376.7}\frac{mn_{eff}\left(\frac{1}{\kappa^2}+\frac{1}{\gamma^2}\right)}{a\left(\frac{J_m'(\kappa a)}{\kappa}+\frac{K_m'(\gamma a)J_m(\kappa a)}{\gamma K_m(\gamma a)}\right)}$$

$$A_2 = \frac{1}{K_m(\gamma a)} \qquad B_2 = \frac{1}{376.7}\frac{mn_{eff}\left(\frac{1}{\kappa^2}+\frac{1}{\gamma^2}\right)}{a\left(\frac{J_m'(\kappa a)K_m(\gamma a)}{\kappa J_m(\kappa a)}+\frac{K_m'(\gamma a)}{\gamma}\right)}, \qquad (2.3.23)$$

where n_{eff} is the effective refractive index of the guiding mode, satisfying the relation $n_{eff} = \frac{\lambda}{2\pi}\beta$.

Figure 2.3.2 shows the ratio of the power carried in tapered fibers (black solid) and the fractional power leakage in the air (red solid) as a function of the waist diameter. The pump light is launched into the tapered fiber at 800 nm. It demonstrates that with reducing the waist diameter more power leaks out of the fiber and the intensity inside decreases.

Figure 2.3.3 shows the ratio of the power carried in the tapered fiber (black solid) and the fractional power leakage into the air (red dashed) as a function of the pump wavelength. The diameter of fiber waist used in the simulation is 1 μm. It demonstrates the fractional leakage power increases with wavelength, and at shorter wavelength the intensity inside the fiber is higher.

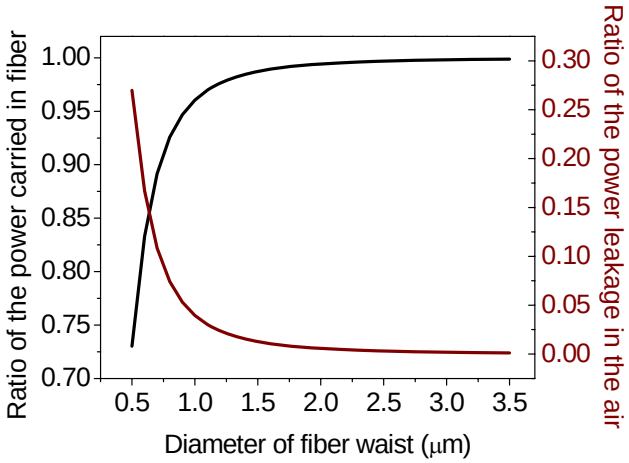

Fig. 2.3.2 Ratio of the power carried in tapered fibers (black solid) and the fractional power leakage into the air (red solid) as a function of the waist diameter. The pump wavelength is 800 nm.

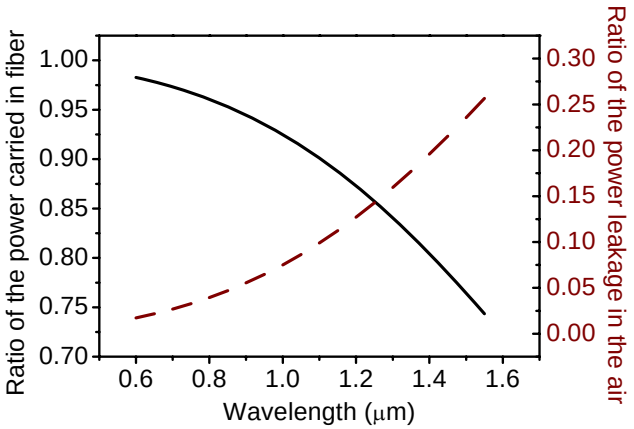

Fig. 2.3.3 Ratio of the power carried in the tapered fiber (black solid) and the fractional power leakage in the air (red dashed) as a function of the pump wavelength. The diameter of fiber waist used in the simulation is 1 μm.

For the purpose of information transmission, a fiber should be designed with a high amount of the power carried in the optical fiber to decrease the fiber losses. However, a tapered fiber with high leakage power can also find applications in an amount of fields, such as dispersion tailoring, gas sensors, atom trapping, and so on.

2.4 Principles of nonlinear optics in the waist region of tapered fibers

In section 2.3, we assumed that the overall response of the medium react linearly on the external field. This simplification is only valid in the case where the optical field strength is rather low. If the applied light field is so strong that it is comparable with the inner atomic field, the response of the valence electron is no longer linear and the rules of linear optics are not valid any more. In other words, the presence of an optical field propagating through a medium changes the properties of the medium which, in turn, modify the optical field itself [53]. Therefore, to understand the complete pulse propagation behavior for high intensity pulse, we must take full account of both the effects of the pulse fields on the medium and the effects of the medium polarization back on the pulses.

This section introduces the fundamentals of several nonlinear optical effects, such as self-phase modulation [27-29], optical soliton formation [58-62], Raman inelastic scattering [32,38-40], *etc*.. We first start with the deviation of the nonlinear pulse-propagation equation in section 2.4.1, which governs propagation of optical pulses in nonlinear dispersive fibers. The effect of group velocity dispersion (GVD) on the pulse propagation is introduced in section 2.4.2. Generally speaking, the dispersion effect does not really belong to nonlinear optics, however, the GVD plays a critical role in the generation of supercontinua, which makes it convenient to discuss it in the chapter of nonlinear optics. Section 2.4.3 deals with self-phase modulation (SPM), a phenomenon that leads to spectral broadening of the incident pulses. In section 2.4.4, the concept of optical solitons, which are formed as a result of the interplay between the dispersive and nonlinear effects, is introduced. Stimulated Raman scattering, which is the primary inelastic scattering process occurring in optical fibers, will be discussed in section 2.4.5. We will introduce cross phase modulation (XPM) in section 2.4.6. The mechanism responsible for this effect arises from the changes of the refractive index induced by the intensity of other copropagating fields. The last section 2.4.7 deals with four wave mixing, which describes the interaction of four waves or photons with each other due to the third-order susceptibility in a nonlinear medium.

2.4.1 Nonlinear pulse-propagation equation

Maxwell’s equations can also be used to obtain the nonlinear pulse-propagation

equation in dispersive nonlinear media. In section 2.3.1, we derived equation Eq. (2.3.5), where the induced polarization **P** and electrical field **E** followed the linear relation Eq. (2.3.4) through the electric susceptibility function χ_e. However, with the presence of nonlinear effects, the induced polarization does not satisfy this linear relation any more, and instead it is expressed by the first few terms in a series expansion in powers of the electric field **E** [63]:

$$\begin{aligned}\mathbf{P} &= \varepsilon_0 \chi^{(1)} \cdot \mathbf{E} + \varepsilon_0 \chi^{(2)} : \mathbf{E}^2 + \varepsilon_0 \chi^{(3)} \vdots \mathbf{E}^3 \cdots \\ &\equiv \mathbf{P}_1 + \mathbf{P}_2 + \mathbf{P}_3 \cdots,\end{aligned} \tag{2.4.1}$$

where the quantities $\chi^{(2)}$ and $\chi^{(3)}$ are called the second- and third-order nonlinear optical susceptibilities, respectively. The polarization at time *t* is assumed to depend only on the instantaneous value of the electric field strength. This limit will be relaxed in section 2.5. In the case of tapered fibers manufactured by fused silica, only $\mathbf{P}_1$ and $\mathbf{P}_3$ contribute to the total induced polarization because of the following properties of fused silica: First, for materials which posses a center of inversion symmetry, such as fused silica, the induced polarization has only odd powers of the electric field. Second, $\mathbf{P_1}$ and $\mathbf{P_3}$ are the only nonlinear effects observed before catastrophic or irreversible damage of an optical fiber occurs.

To solve Maxwell's equations including nonlinear effects, three assumptions are made to simplify the Eq. (2.3.3) [25]. First, $\mathbf{P}_3$ is treated as a small perturbation to $\mathbf{P}_1$, because the nonlinear changes in the refractive index are very small compared to the linear effect. Second, the optical field is assumed to maintain its polarization along the fiber length so that a scalar approach can be made to replace the exact eigenvalue equation introduced in section 2.3.2. It holds not true for a conventional tapered fiber, however, the approximation offers quite good results in practice. Third, the optical field is assumed to be quasi-monochromatic, that implies that the spectral width is much smaller than the central frequency ω_0, which is valid for pulses with durations longer than 0.1 ps. Moreover, in the simulation of the pulse propagation in tapered fibers, we ignore the material absorption effect, which is negligible for a tapered fiber since the propagating length is as short as 10 cm.

Following the three assumptions, we can write the electric filed by separating the rapidly varying part and the slowly varying part in the form

$$\mathbf{E}(\mathbf{r},t) = \frac{1}{2}\hat{x}\left[E(\mathbf{r},t)\exp(-i\omega_0 t) + c.c.\right], \tag{2.4.2}$$

where *x* is the polarization unit vector and $E(\mathbf{r},t)$ is a slowly varying function of time.

The linear polarization part $\mathbf{P}_1$ and nonlinear polarization part $\mathbf{P}_3$ can be expressed in the similar way:

$$\mathbf{P}_1(\mathbf{r},t) = \frac{1}{2}\hat{x}\left[P_1(\mathbf{r},t)\exp(-i\omega_0 t) + c.c.\right] \tag{2.4.3}$$

$$\mathbf{P}_3(\mathbf{r},t) = \frac{1}{2}\hat{x}\left[P_3(\mathbf{r},t)\exp(-i\omega_0 t) + c.c.\right]. \tag{2.4.4}$$

Substituting Eq. (2.4.2) to Eq. (2.4.1) results in

$$\begin{aligned}
\mathbf{P}_3(\mathbf{r},t) &= \varepsilon_0 \chi^{(3)}_{xxxx} \frac{1}{2^3}\left[E(\mathbf{r},t)\exp(-i\omega_0 t) + c.c.\right]^3 \\
&= \varepsilon_0 \chi^{(3)}_{xxxx} \frac{1}{2^3}\left[E^2\exp(-i2\omega_0 t) + \left(E^*\right)^2\exp(i2\omega_0 t) + 2\left|E\right|^2\right]\left[E\exp(-i\omega_0 t) + c.c.\right] \\
&= \varepsilon_0 \chi^{(3)}_{xxxx} \frac{1}{2^3}\left\{\left[E^3\exp(-i3\omega_0 t) + c.c\right] + 3\left|E\right|^2\left[E\exp(-i\omega_0 t) + c.c.\right]\right\} \\
&\approx \varepsilon_0 \chi^{(3)}_{xxxx} \frac{1}{2}\cdot\frac{3}{4}\left|E(\mathbf{r},t)\right|^2\left[E(\mathbf{r},t)\exp(-i\omega_0 t) + c.c.\right],
\end{aligned} \tag{2.4.5}$$

where the term oscillating at the third-harmonic frequency $3\omega_0$ requires phase matching and is generally negligible in optical fibers. By comparing with the Eq. (2.4.4), P_3(**r**,t) can be expressed as

$$P_3(\mathbf{r},t) = \frac{3}{4}\varepsilon_0 \chi^{(3)}_{xxxx}\left|E(\mathbf{r},t)\right|^2 E(\mathbf{r},t) \equiv \varepsilon_0 \varepsilon_{NL} E(\mathbf{r},t), \tag{2.4.6}$$

where ε_{NL} is defined as the nonlinear contribution to the dielectric constant and treated as a constant during the pulse propagation.

It is easier to solve a differential equation in the frequency domain. The Fourier transform of $E(\mathbf{r},t)$, $\tilde{E}(\mathbf{r},\omega-\omega_0)$, is defined as

$$\tilde{E}(\mathbf{r},\omega-\omega_0) = \int_{-\infty}^{\infty} E(\mathbf{r},t)\exp\left[i(\omega-\omega_0)t\right]dt\,. \tag{2.4.7}$$

The linear component P_1 in frequency domain is expressed as

$$\begin{aligned}
P_1(\mathbf{r},t) &= \frac{\varepsilon_0}{2\pi}\int_{-\infty}^{\infty} \tilde{\chi}^{(1)}_{xx}(\omega)\tilde{E}(\mathbf{r},\omega-\omega_0)\exp\left[-i(\omega-\omega_0)t\right]d\omega \\
&= \int_{-\infty}^{\infty} E(\mathbf{r},t)\exp\left[i(\omega-\omega_0)t\right]dt.
\end{aligned}. \tag{2.4.8}$$

By substituting Eq.(2.4.2-2.4.4) in Eq. (2.3.3), the Fourier transform $\tilde{E}(\mathbf{r},\omega-\omega_0)$ is found to satisfy the Helmholtz equation

$$\nabla^2\tilde{E} + \varepsilon(\omega)k_0^2\tilde{E} = 0\,, \tag{2.4.9}$$

where $\varepsilon(\omega) = 1 + \tilde{\chi}^{(1)}_{xx}(\omega) + \varepsilon_{NL}$. We define the total refractive index $\tilde{n}$ including the nonlinear effect as

$$\tilde{n} = n + n_2\left|E\right|^2, \tag{2.4.10}$$

where n_2 is a measure of the fiber nonlinearity and satisfies the relation $n_2 = \frac{3}{8n}\mathrm{Re}(\chi^{(3)}_{xxxx})$.

Using the method of separation of variables, we write the expression of $\tilde{E}(\mathbf{r}, \omega - \omega_0)$ as:

$$\tilde{E}(\mathbf{r}, \omega - \omega_0) = F(x, y)\tilde{A}(z, \omega - \omega_0)\exp(i\beta_0 z), \tag{2.4.11}$$

where $\tilde{A}(z, \omega - \omega_0)$ is a slowly varying function of z and β_0 is the wave number at the center frequency ω_0. Substituting to the Helmholtz Eq. (2.4.9) leads to the following two equations [25]:

$$\frac{\partial^2 F}{\partial x^2} + \frac{\partial^2 F}{\partial y^2} + \left[\varepsilon(\omega)k_0^2 - \tilde{\beta}^2\right]F = 0 \tag{2.4.12-a}$$

$$2i\beta_0 \frac{\partial \tilde{A}}{\partial z} + \left(\tilde{\beta}^2 - \beta_0^2\right)\tilde{A} = 0, \tag{2.4.12-b}$$

where the second order derivative $\frac{\partial^2}{\partial z^2}$ of the slowly varying function $\tilde{A}(z, \omega - \omega_0)$ is ignored. Since the dielectric constant $\varepsilon(\omega)$ in Eq. (2.4.12-a) can be approximated by

$$\varepsilon(\omega) = \tilde{n}^2 = (n + \Delta n)^2 \approx n^2 + 2n\Delta n, \tag{2.4.13}$$

where Δn is a small perturbation, we can solve Eq. (2.4.12) taking advantage of first-order perturbation theory.

The eigenvalue $\tilde{\beta}$ is written by $\tilde{\beta}(\omega) = \beta(\omega) + \Delta\beta$, where $\beta(\omega)$ is the wave number of Eq. (2.3.9) in the case without perturbation Δn. To the first order in perturbation of nonlinear polarization P_3, $\Delta\beta$ is found to satisfy the relation

$$\Delta\beta = \frac{k_0 \int\int_{-\infty}^{\infty} \Delta n \left|F(x, y)\right|^2 dxdy}{\int\int_{-\infty}^{\infty} \left|F(x, y)\right|^2 dxdy}, \tag{2.4.14}$$

where $F(x, y)$ is the modal distribution without the nonlinear perturbation. The Eq. (2.4.12-b) can be well-approximated by replacing $\tilde{\beta}^2 - \beta_0^2$ with $2\beta_0\left(\tilde{\beta} - \beta_0\right)$ as

$$\frac{\partial \tilde{A}}{\partial z} = i\left[\beta(\omega) + \Delta\beta - \beta_0\right]\tilde{A}. \tag{2.4.15}$$

Transforming the Eq. (2.4.15) back to the time domain, the propagation equation for $A(z, t)$ can be obtained. However, it is impossible to directly transform the wave number $\beta(\omega)$ to the time domain without knowing its exact functional form, therefore, we expand $\beta(\omega)$ in a Taylor series about the center frequency ω_0 as

$$\beta(\omega)=\beta_0+(\omega-\omega_0)\left(\frac{d\beta}{d\omega}\right)\Big|_{\omega=\omega_0}+\frac{1}{2}(\omega-\omega_0)^2\left(\frac{d^2\beta}{d\omega^2}\right)\Big|_{\omega=\omega_0}+\frac{1}{6}(\omega-\omega_0)^3\left(\frac{d^3\beta}{d\omega^3}\right)\Big|_{\omega=\omega_0}+\cdots. \tag{2.4.16}$$

We define

$$\beta_k=\left(\frac{d^k\beta}{d\omega^k}\right)\Big|_{\omega=\omega_0} \quad (m=1,2,3,\ldots..). \tag{2.4.17}$$

β_k is called k^{th} order dispersion coefficient and represents the dispersion character of an optical fiber. Those dispersion coefficients play critical roles in the light propagation through fibers, which will be discussed in detail in the next section.

Substituting this equation into Eq. (2.4.15) and taking the inverse Fourier transform result in the propagation equation for $A(z, t)$ as

$$\begin{aligned}\frac{\partial A(z,t)}{\partial z}&=\sum_{k=1}\frac{i^{k+1}}{k!}\beta_k\cdot\frac{\partial^k A(z,t)}{\partial t^k}+i\Delta\beta A(z,t)\\&=\sum_{k=1}\frac{i^{k+1}}{k!}\beta_k\cdot\frac{\partial^k A(z,t)}{\partial t^k}+i\gamma\left|A(z,t)\right|^2A(z,t),\end{aligned} \tag{2.4.18}$$

where $\Delta\beta$ is evaluated by using Eqs. (2.4.14) and (2.4.10), and the nonlinear parameter γ is given in the form

$$\gamma=\frac{n_2\omega\int\int_{-\infty}^{\infty}\left|F(x,y)\right|^4dxdy}{c\left(\int\int_{-\infty}^{\infty}\left|F(x,y)\right|^2dxdy\right)^2}. \tag{2.4.19}$$

All the parameters related to the case without nonlinear perturbation, such as $\beta(\omega)$ and $F(x, y)$, can be solved in a similar way as the longitude components E_z and H_z are solved in section 2.3.2.

Equation (2.4.18) is the so-called nonlinear Schrödinger equation (NLSE), which describes the pulse propagation in an optical fiber. It considers the dispersion character through the dispersion coefficients β_k and deals with the nonlinear effect through the nonlinear parameter γ, however, it ignores the effect of fiber losses and the Raman effect. The Raman effect, arising from the molecular vibrations, plays an important role in the supercontinuum generation, which will be introduced in section 2.4.5) and further discussed in section 2.6.

To solve the nonlinear Schrödinger Eq. (2.4.18), we introduce a new reference (T, z), which travels with the pulse at group velocity v_g. In this reference the variable T follows the expression $T=t-z/v_g$, and the NLSE can be written as

$$\frac{\partial A(z,T)}{\partial z}=\sum_{k=2}\frac{i^{k+1}}{k!}\beta_k\cdot\frac{\partial^k A(z,T)}{\partial T^k}+i\gamma\left|A(z,T)\right|^2 A(z,T). \qquad (2.4.20)$$

2.4.2 Group velocity dispersion

Group velocity dispersion (GVD), representing the frequency (or wavelength) dependence of the group velocity of light in a medium, is responsible for dispersive broadening of pulses and for the group velocity mismatch of different waves in nonlinear interactions. Mathematically the GVD of a tapered fiber is defined as the second derivative of the propagation constant β with respect to ω, $D=-\frac{2\pi c}{\lambda^2}\beta_2$. In this section, we will consider the pulse-propagation problem by treating fibers as a linear optical medium and only discuss the effects of group velocity dispersion and higher order dispersion on the pulse propagation without taking the nonlinear effect into account (γ=0).

The nonlinear Schrödinger equation with dispersion alone becomes

$$\frac{\partial A(z,T)}{\partial z}=-\frac{i}{2}\beta_2\cdot\frac{\partial^2 A(z,T)}{\partial T^2}+\frac{1}{6}\beta_3\cdot\frac{\partial^3 A(z,T)}{\partial T^3}+\frac{i}{24}\beta_4\cdot\frac{\partial^4 A(z,T)}{\partial T^4}+\cdots. \qquad (2.4.21)$$

The cubic and higher–order terms in the expansion are generally negligible if the spectral width is much smaller than the center frequency $\Delta\omega\le\omega_0$. If $\beta_2\approx 0$ for some specific values of center frequency or the spectral width is too large to neglect, the higher-order terms have to be included. We first only discuss the effect of the group velocity dispersion on the pulse propagation, conveniently described by a simplified NLSE

$$\frac{\partial A(z,T)}{\partial z}=-\frac{i}{2}\beta_2\cdot\frac{\partial^2 A(z,T)}{\partial T^2}. \qquad (2.4.22)$$

The equation can be readily solved by using a Fourier-transform method. However, to enable a simulation method applicable for a general NLSE, we employ the split-step Fourier method [25] [45,46] to solve Eq.(2.4.22). The split-step Fourier method has been used extensively to solve the pulse-propagation problems in nonlinear dispersive media. This method will be discussed in detail in section 2.5.1.

We assume the incident pulse, emitted from mode-locked lasers, to be of hyperbolic-secant shape. The electric field $A(0,T)$ corresponding to such a pulse can be expressed in the form

$$A(0,T)=\sqrt{P_0}\,\mathrm{sech}(\frac{T}{T_0}), \tag{2.4.23}$$

where P_0 represents the peak power of the incident pulse and T_0 is the input pulse width.

Solving the Eq. (2.4.22) with the split-step Fourier method, we plot Fig. 2.4.1, showing the normalized intensity ($\left|A(z,T)\right|^2 / P_0$) in the time domain at different propagating distances. It demonstrates that under the effect of group velocity dispersion, the pulse width increases with propagation along the fiber, which is the so called dispersion-induced broadening. Dispersion-induced pulse broadening can be understood as different frequency components of a pulse traveling at slightly different speeds along the fiber.

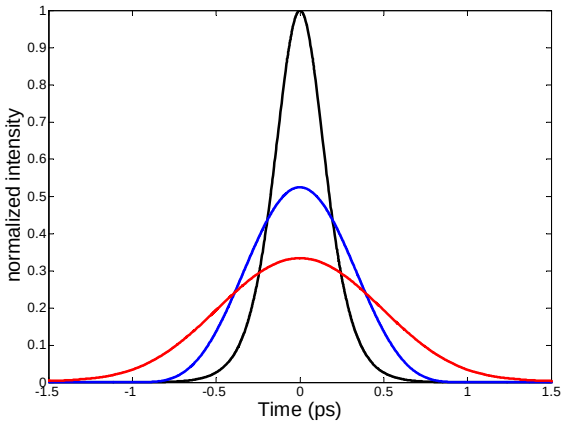

Fig. 2.4.1 Pulse intensities in the time domain, with input pulse duration of 0.35 *ps*, β_2 equal to 0.02 ps^2/m and propagation distance *z* at 0 *m* (black), 4 *m* (blue), 8 *m* (red), respectively.

Although the contribution of GVD dominates the dispersion effect in most cases, the third-order term proportional to β_3 in Eq. (2.4.21) should be taken into account provided that $\beta_2 \approx 0$ or the spectral width is large. Figure 2.4.2 shows the normalized pulse intensity under the combined effect of β_2 and β_3. Different from the pulse shape with group velocity dispersion alone (red), the third order dispersion distorts the symmetry of the pulse and the pulse shape exhibits an oscillatory structure near the trailing edge.

In this section, we only consider the effect of dispersion up to the third order. However, in the case that the spectral width is extremely large, such as in supercontinuum generation, one should definitely take higher order dispersion into account, which will be discussed further in section 2.5.

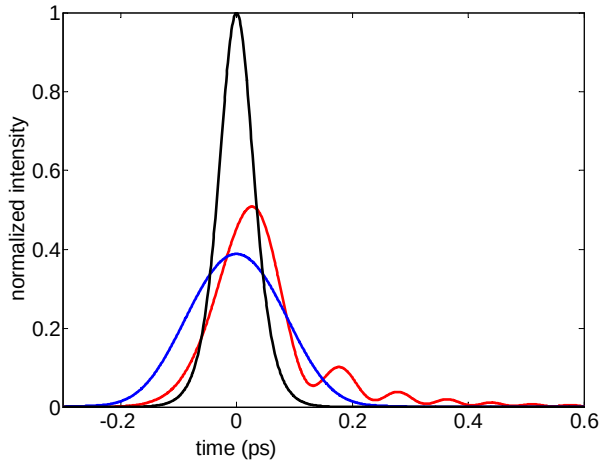

Fig. 2.4.2 Pulse intensities in the time domain for input pulse (dashed curve), β_2 alone (blue), and combined effect of β_2 and β_3. Input pulse duration is 0.04 *ps*, β_2 and β_3 are equal to -0.001 ps^2/m and 0.0001 ps^3/m, respectively, and propagation distance *z* is 5 *m*.

2.4.3 Self phase modulation

Self phase modulation (SPM) arises from the dependence of the fiber refractive index upon the field intensity (optical Kerr effect), which results in a phase alteration of the pulses. The alteration of the phase consequently leads to a modulation of the pulse spectrum. This is so called SPM-induced spectral broadening. In this section, we show how the self phase modulation affects the pulse propagation through fibers without the consideration of dispersion and other nonlinear effects. The combined effect of SPM and GVD on the pulse is discussed in section 2.4.4.

The nonlinear Schrödinger equation describing the effect of self phase modulation alone can be expressed as

$$\frac{\partial A(z,T)}{\partial z} = i\gamma \left|A(z,T)\right|^2 A(z,T). \tag{2.4.24}$$

The following solutions can be readily obtained by assuming $A(z,T) = V\exp(i\phi_{NL})$ [25],

$$\frac{\partial V}{\partial z} = 0; \qquad \frac{\partial \phi_{NL}}{\partial z} = \gamma V^2. \tag{2.4.25}$$

The amplitude *V* is constant along the fiber, therefore, the phase expression can be obtained by analytically integrating the phase equation as

$$\phi_{NL}(z,T) = \gamma z \left|A(0,T)\right|^2, \tag{2.4.26}$$

and

$$A(z,T) = A(0,T)\exp\left(i\gamma z \left|A(0,T)\right|^2\right). \tag{2.4.27}$$

The solutions show that SPM causes an intensity-dependent phase shift but the pulse shape remains unchanged. The SPM-induced spectral broadening is a consequence of the time dependence of the phase, which implies that the instantaneous optical frequency differs across the pulse. The frequency difference from its central value ω_0 is given by

$$\delta\omega(T) = -\frac{\partial \phi_{NL}}{\partial T} = -\gamma z \frac{\partial}{\partial T}\left|A(0,T)\right|^2 . \tag{2.4.28}$$

The time dependence of $\delta\omega(T)$, referred to as frequency chirping, increases with the propagated distance, which means new frequency components are generated continuously as the pulse propagates along the fiber.

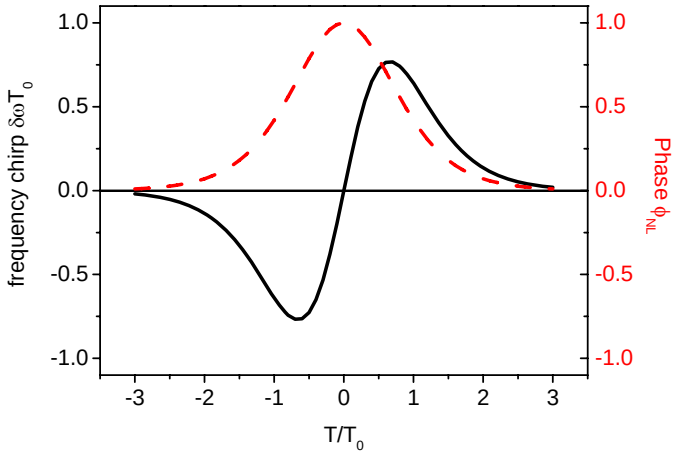

Fig. 2.4.3 The induced frequency chirp (black) and the nonlinear phase shift (red) across the pulse in temporal domain.

The frequency chirp depends on the pulse shape. In the case of a hyperbolic-secant incident pulse with the pulse shape given in Eq. (2.4.23), the SPM-induced chirp $\delta\omega(T)$ becomes

$$\delta\omega(T) = \frac{2P_0\gamma z}{T_0}\operatorname{sech}^2\left(\frac{T}{T_0}\right)\tanh\left(\frac{T}{T_0}\right). \tag{2.4.29}$$

Figure 2.4.3 shows the induced frequency chirp and the nonlinear phase shift across the pulse in the temporal domain. The temporal variation of the phase has the same shape as that of the pulse, while the frequency chirp is negative near the leading edge and becomes positive near the trailing edge of the pulse. In other words, the new frequency components with red shift are generated in the leading part of the pulse and the components with blue shift are generated in the trailing region.

The spectral property can be obtained by taking the Fourier transform of the electric field *A(z, T)*, which, however, depends not only on the pulse shape but also on

the initial chirp imposed on the pulse. A hyperbolic-secant electric field with chirp parameter C can be written as

$$A(0,T)=\sqrt{P_0}\,\mathrm{sech}\left(\frac{T}{T_0}\right)\exp\left(-\frac{iCT^2}{2T_0}\right). \tag{2.4.30}$$

Substituting this expression into Eq. (2.4.27), the spectral properties are obtained. Figure 2.4.4 shows the spectrum generated by SPM without initial chirp, which exhibits a multipeak structure. The origin of this oscillatory structure can be understood by recalling Fig. 2.4.3, the same chirp occurs at two time points across the pulse, therefore this pulse has the same instantaneous frequency at two distinct positions. These two points, considered as two waves of the same frequency but different phases, can interfere with each other. The oscillatory structure is the result of such interference [27].

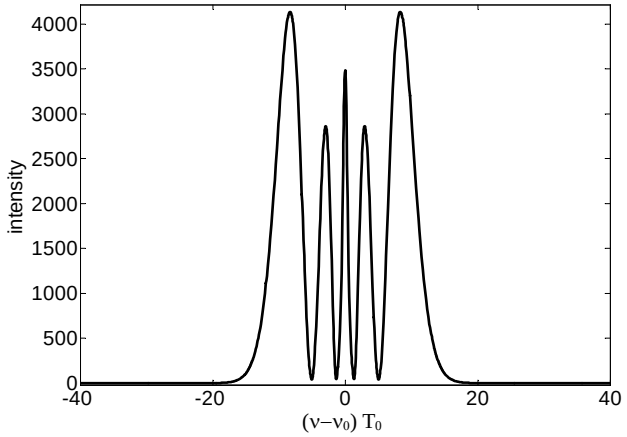

Fig. 2.4.4 Spectrum generated by SPM without initial chirp.

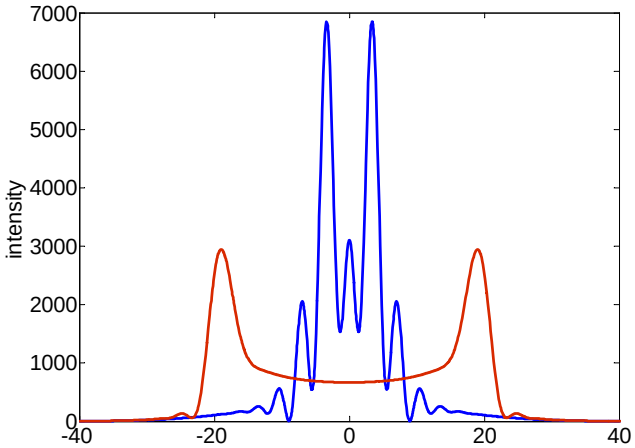

Fig. 2.4.5 Spectrum generated by SPM with positive initial chirp (red) and negative initial chirp (blue).

Figure 2.4.5 shows the spectra generated by SPM with positive (red one) and negative (blue one) chirps. Comparing the spectra, we can see that an initial frequency chirp can lead to drastic changes in the SPM-broadened spectrum. A negative chirp parameter increases the spectral broadening while the opposite occurs in the case of a positive chirp. This can be understood by noting that the sign of frequency chirp varies the same as that of the initial chirp, in the case of *C* positive, therefore, a positive initial chirp adding the extent of the SPM-induce chirp results in an enlarged broadening spectrum. In the case of *C* negative, the two chirps contribute opposite sign, hence, a negative initial chirp reduces the spectral width of the pulse.

Note: Figure 2.4.5 shows an opposite property as that given in reference [64], where the red curve represents the spectrum with negative chirp and the blue one corresponds to a positive chirp. The physical explanation in this dissertation also differs from what the author stated in [64].

2.4.4 Optical soliton

We have discussed the influence of the dispersive and nonlinear effects on the pulse propagation along fibers separately. In this section, the interplay between those effects is described, which in certain conditions can result in the formation of the so called soliton. The word soliton refers to special kinds of wave packets that can propagate undistorted over long distances.

The nonlinear Schrödinger equation, which describes the combination of dispersion and nonlinear effects, can be written as:

$$\frac{\partial A(z,T)}{\partial z} = -\frac{i}{2}\beta_2 \cdot \frac{\partial^2 A(z,T)}{\partial T^2} + i\gamma \left|A(z,T)\right|^2 A(z,T). \qquad (2.4.31)$$

Before solving the NLSE, we first introduce a new parameter called “soliton number *N*”, which describes the relative importance of the self phase modulation and dispersion influence on pulse evolution along the fiber. It is defined as

$$N = \sqrt{\frac{\gamma P_0 T_0^2}{|\beta_2|}}. \qquad (2.4.32)$$

For soliton number N much smaller than 1, dispersion dominates the pulse evolution, in the case of N much larger than 1, SPM dominates, and for values of N approximately equal to 1, both SPM and GVD play an equally important role during pulse propagation.

Although the soliton number *N* is independent of the sign of β_2, the pulse

evolution relies strongly on whether the GVD is normal ($\beta_2 > 0$) or anomalous ($\beta_2 < 0$). For GVD in the normal-dispersion regime, the pulse broadens rapidly, whereas in the case of GVD in anomalous-dispersion regime, the pulse appears to propagate in a steady state along the fiber. This can be understood by noting that SPM generates new frequency components that are red-shifted near the leading edge and blue-shifted near the trailing edge of the pulse [25]. In the normal-dispersion regime, the red components travel faster than the blue ones, therefore, the pulse is forced to broaden further and further and such a combined effect of SPM and GVD even leads to an enhanced rate of pulse broadening compared with that expected from GVD alone. However in the case of GVD in anomalous-dispersion regime, the red components travel more slowly than the blue components, therefore, the SPM-induced chirp given in Eq. (2.4.6) is cancelled completely by the dispersion effect, which leads to an unchanged pulse shape during the propagation. Such an undistorted pulse propagating in the fiber corresponds to a bright soliton and especially the soliton with *N* equal to 1 corresponds to the so-called fundamental soliton. We should note that this holds true for a focusing nonlinearity with $n_2>0$, as is the case in SiO_2.

In the case of higher-order solitons, where $N>1$, the pulse evolution can also be described by the general solution of Eq. (2.4.31). Figure 2.4.6 and Fig. 2.4.7 show the spectral and temporal properties of a propagating hyperbolic-secant pulse with soliton number *N* of 3. SPM dominates initially but GVD soon catches up and leads to pulse contraction. An interesting property of higher order solitons is that as the pulse propagates along the fiber, it first contracts to a fraction of its initial width, splits into several distinct pulses in the middle of one soliton period and then merges again to recover the original shape at the end of the soliton period. The soliton period z_0 is defined as:

$$z_0 = \frac{\pi}{2}\frac{T_0^2}{|\beta_2|}. \tag{2.4.33}$$

Soliton theory [65] shows: for pulses with a hyperbolic-secant shape, the two effects can cooperate in such a way that the pulse follows a periodic evolution pattern with the original shape recurring at multiples of the soliton period z_0.

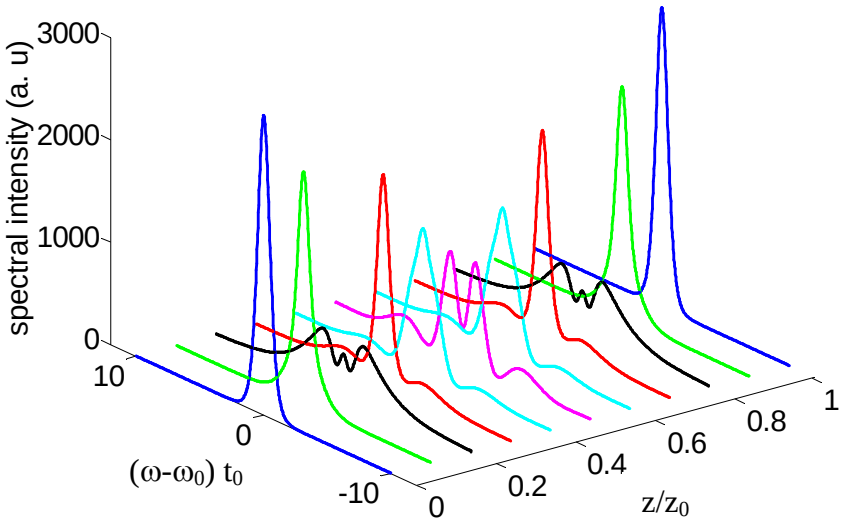

Fig. 2.4.6 The spectral properties of a propagating hyperbolic-secant pulse with soliton number N =3.

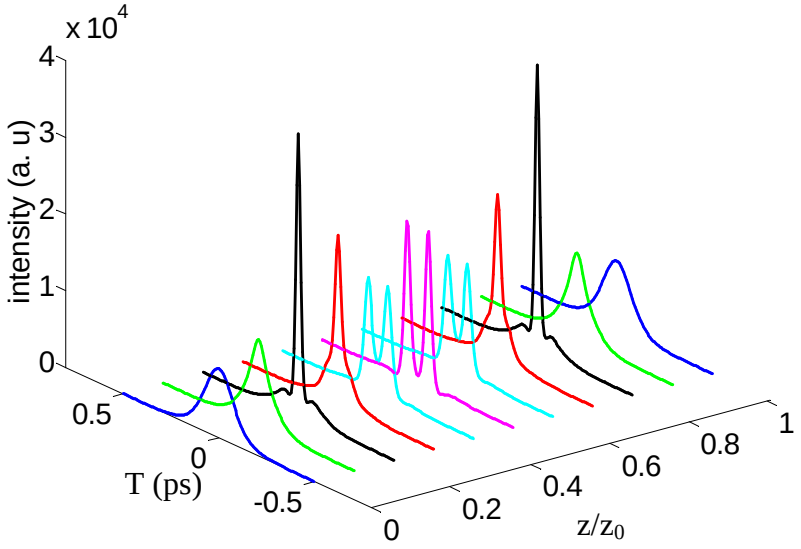

Fig. 2.4.7 The temporal properties of a propagating hyperbolic-secant pulse with soliton number N = 3.

2.4.5 Raman scattering

When electromagnetic radiation at optical frequencies travels through media, various scattering processes can occur, such as Raman scattering [32,38-40], Rayleigh-wing scattering, Brillouin scattering, and so on. In each case light is scattered by fluctuations of the refractive index which are caused by the intermolecular oscillations or twists of the medium. In this section, we only discuss the Raman scattering, which is the primary scattering process occurring in the supercontinuum generation of tapered fibers.

This section introduces the effect of Raman scattering on the pulse propagation in fibers. We start with a general view of Raman scattering, which explains the

properties of Raman scattering with a quantum-mechanical energy diagram. Then we discuss the Raman gain spectrum and the nonlinear Raman response function, which are indispensable when solving the NLSE with the presence of Raman scattering.

Spontaneous Raman scattering can transfer a small part of the incident light with a distinct frequency into a new wave with lower or higher frequency by exciting molecular vibrations [25]. The origin of the frequency change lies in an energy exchange between the photons and the medium, and the frequency shift is determined by the vibrational modes of the material. Those new components shifted to lower frequencies are called Stokes waves and those shifted to higher frequencies are called anti-Stokes waves. The intensity of the Stokes wave is in the case of a thermal equilibrium much higher than the intensity of the anti-Stokes wave.

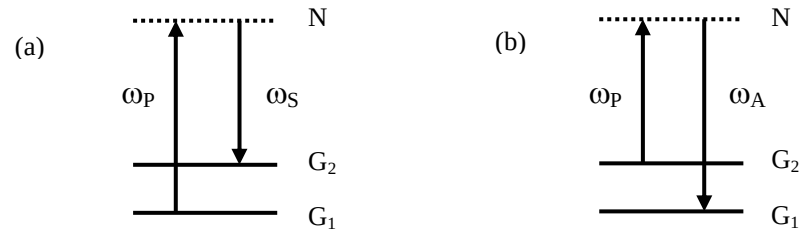

Fig. 2.4.8 Quantum-mechanical energy diagram of Raman scattering for (a) Stokes wave and (b) anti-Stokes wave

These properties can be understood through the quantum-mechanical energy diagram shown in Fig. 2.4.8 [39]. An incident pump photon at frequency ω_P excites the molecule from the ground state G_1 into a higher virtual energy state N. The molecule undergoes a decay falling down into the final state G_2, which is accompanied by the emission of a Stokes photon at frequency ω_S. Similarly, Raman anti-Stokes scattering at frequency ω_A is induced by a transition from level G_2 to level G_1 with level N as the intermediate level. The anti-Stokes waves are many orders of magnitude weaker than the Stokes waves because in thermal equilibrium the population of level G_2 is smaller than the population in level G_1 by the Boltzmann factor $\exp\left(-\frac{E_{G_2}-E_{G_1}}{kT}\right)$ [39].

The Raman scattering depends on the material resonances. The resonance frequencies of the molecular vibration modes in fused silica are overlapped with each other and form rather broad frequency bands. Therefore, optical fibers show Raman scattering over a relatively wide frequency range. The Raman gain g_R, which is defined as Eq. (2.4.34) [8], depends mainly on the composition of the fiber core and

the contained dopants:

$$\frac{dI_S}{dz} = g_R(\Delta\omega) I_P I_S , \tag{2.4.34}$$

where I_S is the Stokes intensity, I_P is the pump intensity, $\Delta\omega$ is the frequency difference between the pump and Stokes waves, and the Raman-gain coefficient g_R is related to the cross section of spontaneous Raman scattering [66-68].

The Raman gain $g_R(\Delta\omega)$, as a function of the frequency shift, is the most important quantity to describe Raman scattering, which is shown in Fig. 2.4.9 [68].

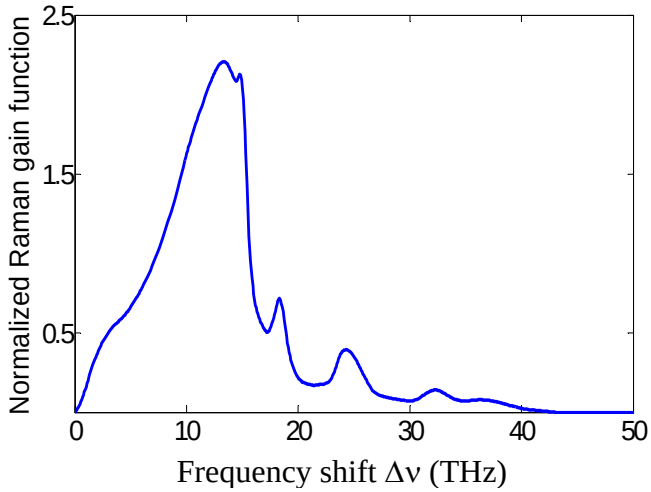

Fig. 2.4.9 The normalized Raman gain spectrum as a function of frequency shift.

Due to the frequency-shift property, the Raman gain can be described by a time-dependent nonlinear refractive index [63], related to a response function in the expression of the third order nonlinear coefficient $\chi^{(3)}$. Equation (2.4.35) expresses the third order polarization in the general case, where Raman scattering is present and the third order nonlinear coefficient $\chi^{(3)}$ consists of a delayed Raman response function.

$$\mathbf{P}_3(\mathbf{r},t) = \varepsilon_0 \int\int\int_{-\infty}^{\infty} \chi^{(3)}(t,t_1,t_2,t_3) \vdots \mathbf{E}(\mathbf{r},t_1)\mathbf{E}(\mathbf{r},t_2)\mathbf{E}(\mathbf{r},t_3) dt_1 dt_2 dt_3 , \tag{2.4.35}$$

where $\chi^{(3)}(t,t_1,t_2,t_3)$ is the time-dependent nonlinear coefficient.

To determine the nonlinear coefficient $\chi^{(3)}(t,t_1,t_2,t_3)$, the Born-Oppenheimer (BO) approximation [63] is applied. For purely optical effects in transparent materials, two distinct physical processes contribute to the third-order nonlinear polarization. First, there is an electronic contribution from the nonlinear distortion of the electron orbits around the average positions of the nuclei. This polarization responds rapidly to field changes, within a few electronic cycles ($\sim 0.1 fs$). Second, there is a nuclear

contribution arising from an optical field induced change in the motions of the nuclei. This polarization responds to the field changes much more slowly than the electronic one (~ *ps*). The Born-Oppenheimer approximation is the assumption that the electronic motion and the nuclear motion in molecules can be separated. Referred to the BO approximation, the third order nonlinear susceptibility becomes [63]

$$\chi^{(3)}_{ijkl}(t,t_1,t_2,t_3)=\sigma_{ijkl}\delta(t-t_1)\delta(t_1-t_2)\delta(t_2-t_3)+\delta(t-t_1)d_{ijkl}(t_1-t_2)\delta(t_2-t_3), \quad (2.4.36)$$

where $\delta(t)$ is a delta function, σ_{ijkl} is a constant tensor which describes the electronic nonlinearity, and $d_{ijkl}(t)$ is a time-dependent function which describes the nuclear contribution to the third-order optical polarization and can be expressed in a similar way as delta function $\int_{-\infty}^{\infty} d_{ijkl}(t)dt=1$.

Substituting Eq. (2.4.36) into Eq. (2.4.35) and assuming the electric field to be $\hat{x}$ polarized, the third-order polarization can be written as

$$\begin{aligned}
P_3(t) &= \varepsilon_0\int_{-\infty}^{t}\left(\sigma_{xxxx}\delta(t-t')+d_{xxxx}(t-t')\right)E^2(t')E(t)dt' \\
&= \varepsilon_0\int_{-\infty}^{t}\left(\frac{3}{4}\sigma_{xxxx}\delta(t-t')+\frac{1}{2}d_{xxxx}(t-t')\right)\left|E^2(t')\right|^2 E(t)dt' \\
&= \varepsilon_0\left(\frac{3}{4}\sigma_0+\frac{1}{2}D_0\right)E(t)\int_{-\infty}^{t}\left(\frac{\frac{3}{4}\sigma_0}{\frac{3}{4}\sigma_0+\frac{1}{2}D_0}\delta(t-t')+\frac{\frac{1}{2}D_0}{\frac{3}{4}\sigma_0+\frac{1}{2}D_0}h_R(t-t')\right)\left|E^2(t')\right|^2 dt' \\
&= \frac{3}{4}\varepsilon_0\chi^{(3)}E(t)\int_{-\infty}^{t}\left((1-f_R)\delta(t-t')+f_R h_R(t-t')\right)\left|E^2(t')\right|^2 dt',
\end{aligned} \quad (2.4.37)$$

where $\frac{3}{4}\sigma_0$ and $\frac{1}{2}D_0$ are the electric and nuclear contribution to the nonlinear polarization with the incident light of continuous waves (cw) laser ($T_0\to\infty$), respectively. The factors of $\frac{3}{4}$ and $\frac{1}{2}$ appearing in the relation represent the local field correctors, which can be derived in the similar way as in Eq. (2.4.5). $h_R(t)$ is the nuclear response function responsible for the Raman gain, $\chi^{(3)}$ is the total nonlinear coefficient with the incident light of CW laser, and f_R represents the fractional contribution of the delayed Raman response to nonlinear polarization.

$\frac{3}{4}\sigma_0$ and $\frac{1}{2}D_0$ can be evaluated by an intensity-induced polarization changes (IIPC) experiment, affiliated with the measurement of differential Raman-scattering cross sections [69]. Details are beyond the scope of this thesis. Knowing the values of

$\frac{3}{4}\sigma_0$ and $\frac{1}{2}D_0$, the fractional contribution of Raman scattering f_R is determined to be 0.18.

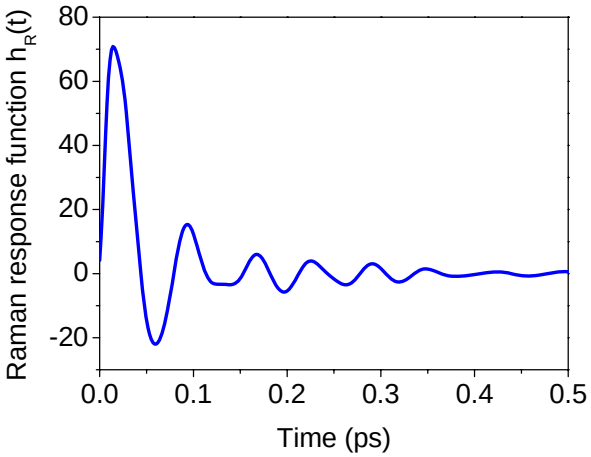

Fig. 2.4.10 Raman response function of fused silica.

The relation between the Raman response function $h_R(t)$ and Raman gain spectrum satisfies the following equation:

$$g_R(\Delta\omega) = \frac{3}{4}\frac{\omega_0}{cn_0} f_R \chi^{(3)} \mathrm{Im}[\tilde{h}_R(\Delta\omega)], \tag{2.4.38}$$

where *Im* stands for the imaginary part and $\tilde{h}_R(\Delta\omega)$ is the Fourier transform of the Raman response function $h_R(t)$. The imaginary part of $\tilde{h}_R(\Delta\omega)$ can be readily calculated from the Eq. (2.4.38), and the real part of $\tilde{h}_R(\Delta\omega)$ can be generated from the imaginary part by using the Kramers-Kronig transformation. The Fourier transformation of $\tilde{h}_R(\Delta\omega)$ provides the Raman response function, shown in Fig. 2.4.10 [68].

Note 1: The derivation of the Raman response function and Raman gain spectrum is different from that in reference [70]. In my opinion, the formula used in the reference [68], especially Eqs. (2.3.30) and (2.3.31) are lacking a reliable theory. The paper "Theoretical description of transient stimulated Raman scattering in optical fibers" by K. J. Blow et al. [46] was used by the authors as a reference to support these two equations, however, I haven't found the same formula in this referenced paper. Using those equations to derive the Raman response function, which is given by Eq. (2.3.35) in [70], one would obtain a factor of 3/4 different from the Eq. (2.4.38) in my dissertation.

Note 2: The response function with respect to time given in [70] is plotted in arbitrary units. Fig. 2.4.10 in my dissertation is a normalized result, therefore, the amplitudes of

the two figures are different.

Using the same way as deriving the NLSE in an instantaneous medium shown in section 2.4.1, we can obtain the following equation for pulse evolution inside a single-mode fiber:

$$\frac{\partial A(z,T)}{\partial z}=\sum_{k=2}\frac{i^{k+1}}{k!}\beta_k\cdot\frac{\partial^k A(z,T)}{\partial T^k}+i\gamma\left(1+\frac{i}{\omega_0}\frac{\partial}{\partial T}\right)\left(A(z,T)\int_{-\infty}^{\infty}R(t')\left|A(z,T-t')\right|^2dt'\right), \tag{2.4.39}$$

where $A(z,t)$ is envelope of the electric field, β_k is the k^{th} order dispersion coefficient at center frequency ω_0, γ is the nonlinear parameter, and *R(t)* is the response function of fused silica satisfying the following formula

$$R(t)=(1-f_R)\delta(t)+f_R h_R(t). \tag{2.4.40}$$

To describe stimulated Raman scattering properly we precede the nonlinear term with a time derivative operator, which ensures that the coupled NLSEs conserve the number of photons and not the optical energy [41]. In this way the equations are valid for pulses with spectral widths as large as one third of the carrier frequency.

Substituting Eq. (2.4.40) into Eq. (2.4.39), the nonlinear Schrödinger equation becomes:

$$\begin{aligned}&\frac{\partial A}{\partial z}-\sum_{k=2}\frac{i^{k+1}}{k!}\beta_k\cdot\frac{\partial^k A}{\partial T^k}\\&=i\gamma\left\{(1-f_R)A|A|^2+(1-f_R)\frac{i}{\omega_0}\frac{\partial}{\partial T}\left[A|A|^2\right]+f_R\left(1+\frac{i}{\omega_0}\frac{\partial}{\partial T}\right)\left(A\int_0^{\infty}h_R(t')\left|A(z,T-t')\right|^2dt'\right)\right\}.\end{aligned} \tag{2.4.41}$$

The first term on the right side of Eq. (2.4.41) corresponds to the self phase modulation, and the third term describes the delayed Raman response, both of which we have discussed. The second term expressed as $i\gamma(1-f_R)\frac{i}{\omega_0}\frac{\partial}{\partial T}\left[A|A|^2\right]$ represents the so-called self steepening effect [25]. The self steepening, which results from the intensity dependence of the group velocity, leads to an asymmetry in the generated spectrum.

2.4.6 Cross-phase modulation

Cross-phase modulation (XPM), similar to self-phase modulation, is also one of the most important nonlinear effects in tapered fibers [34-37]. The fiber nonlinearity can couple two or more fields through cross-phase modulation without inducing any

energy transfer among them [25]. This effect leads to a phase alteration of the pulses and consequently changes the spectrum of the output pulse. The XPM is similar to SPM, however, the spectral broadening of the pulses arise from the effect that different optical fields with different wavelengths interact with each other, as copropagating simultaneously inside the fiber. The refractive index, which an optical field experiences, depends not only on the intensity of that field but also on the intensity of other copropagating fields. Hence, a pulse at one frequency has an influence on a pulse at other frequencies.

The XPM phenomenon can be described by solving the coupled nonlinear Schrödinger equations [25]. In this section, we do not go further into the mathematical derivation of the XPM-induced coupled NLSEs with regards to the third-order nonlinear polarization. We are going to demonstrate the properties of the XPM effect by solving the coupled NLSEs in the case of two optical pulses of different frequency propagating simultaneously in a tapered fiber. The theoretical simulations on photonic crystal fibers have been done with a set of simplified coupled NLSEs [71], where the Raman effect is simplified but not suitable for the simulation in the case of the pulse duration in the femtosecond range.

The copropagation of two pulses in a tapered fiber with a pump of femtosecond duration is found to satisfy the following set of coupled generalized nonlinear Schrödinger equations:

$$\begin{aligned}
&\frac{\partial A_P(z,T)}{\partial z}-\sum_{k=2}\frac{i^{k+1}}{k!}\beta_k^P\cdot\frac{\partial^k A_P(z,T)}{\partial T^k}\\
&=i\gamma_P\left(1+\frac{i}{\omega_{0P}}\frac{\partial}{\partial T}\right)\cdot A_P(z,T)\\
&\quad\times\left\{f_R\int_{-\infty}^{\infty}h_R(t')\left(\left|A_P(z,T-t')\right|^2+\left|A_S(z,T-t')\right|^2\right)dt'+(1-f_R)\left(\left|A_P(z,T)\right|^2+2\cdot\left|A_S(z,T)\right|^2\right)\right\}\\
&\frac{\partial A_S(z,T)}{\partial z}-(\beta_1-\beta_2)\cdot\frac{\partial A_S(z,T)}{\partial T}-\sum_{k=2}\frac{i^{k+1}}{k!}\beta_k^S\cdot\frac{\partial^k A_S(z,T)}{\partial T^k}\\
&=i\gamma_S\left(1+\frac{i}{\omega_{0S}}\frac{\partial}{\partial T}\right)\cdot A_S(z,T)\\
&\quad\times\left\{f_R\int_{-\infty}^{\infty}h_R(t')\left(\left|A_P(z,T-t')\right|^2+\left|A_S(z,T-t')\right|^2\right)dt'+(1-f_R)\left(\left|A_S(z,T)\right|^2+2\cdot\left|A_P(z,T)\right|^2\right)\right\},
\end{aligned}$$

(2.4.42)

where, $A_P(z,T)$ and $A_S(z,T)$ represent the electric fields of the pump pulse and signal pulse, respectively, a reference frame travelling with the pump is used, β_k^P and β_k^S are the dispersion coefficients at the center frequency of the pump and signal, respectively, $\beta_1-\beta_2$ is related to the group-velocity mismatch between the two incident pulses, and γ_P and γ_S are the nonlinear parameters at the center frequency of the pump and signal, respectively. The Raman fraction f_R, equal to 0.18, multiplies the convolution integral term, which accounts for the delayed part of the nonlinear response. The instantaneous part of the nonlinearity is described by the electronic fraction $(1-f_R)$ multiplying the last two terms in the equations. The second last term is responsible for self-phase modulation, and the last term results from phase modulation of one wave by the copropagating wave, responsible for cross-phase modulation. The factor of 2 shows that XPM is twice as effective as SPM for the same intensity.

In our simulations, we consider a tapered fiber with diameter of 3.0 μm and waist length of 1 m. A tapered fiber with such a long waist length is not yet available in practice, however, to demonstrate the properties of the cross-phase modulation more clearly, we employed such a fiber in our simulations. The pump with a wavelength of 890 nm has the nonlinear parameter γ_P of 0.0418/W/m, dispersion coefficients of $\beta_2 = -8.388\times10^{-3}\ ps^2/m$, $\beta_3 = 7.906\times10^{-5}\ ps^3/m$, $\beta_4 = -1.010\times10^{-7}\ ps^4/m$, $\beta_5 = 2.237\times10^{-10}\ ps^5/m$, $\beta_6 = -5.755\times10^{-13}\ ps^6/m$, $\beta_7 = 1.731\times10^{-15}\ ps^7/m$, and an initial electric field $A_P(0,t)$ with the form $\sqrt{P_{Pupm}}\,\mathrm{sech}\left(T/T_0^{pump}\right)$, where the peak power of the pump P_{Pump} is equal to 150 W and the pulse width T_0^{pump} is equal to 150 fs. The signal with a wavelength of 790 nm has the nonlinear parameter γ_P of 0.0474 /W/m, dispersion coefficients of $\beta_2 = 8.361\times10^{-3}\ ps^2/m$, $\beta_3 = 5.992\times10^{-5}\ ps^3/m$, $\beta_4 = -6.010\times10^{-8}\ ps^4/m$, $\beta_5 = 1.234\times10^{-10}\ ps^5/m$, $\beta_6 = -2.862\times10^{-13}\ ps^6/m$, $\beta_7 = 7.837\times10^{-16}\ ps^7/m$, and an initial electric field $A_S(0,t)$ of $\sqrt{P_{signal}}\ \mathrm{sech}\left((T-t_d)/T_0^{signal}\right)$, where the peak power of the signal P_{signal} is equal to 1 W, the pulse width T_0^{signal} is equal to 200 fs, and a delayed parameter t_d used to compensate the group velocity mismatch is equal to 40 fs.

Figure 2.4.11 shows the spectral and temporal properties of the copropagating

pulses in the tapered fiber. For a better understanding of cross-phase modulation, we also present the spectra and intensities of the pump and signal, generated by the wave itself alone, as shown in Fig. 2.4.12.

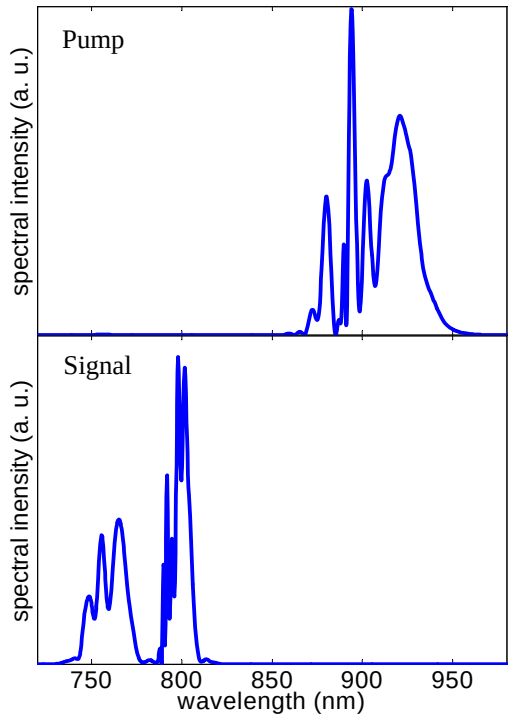

(a)

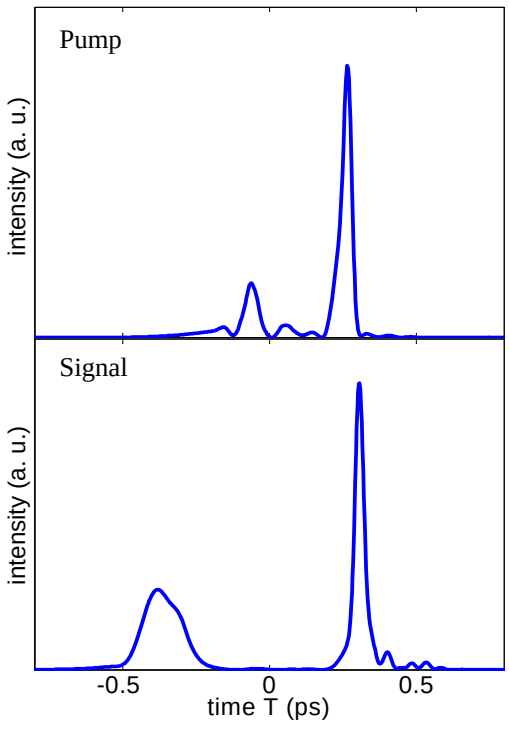

(b)

Fig. 2.4.11 The spectral (a) and temporal (b) properties of the pump and signal pulses with consideration of cross-phase modulation.

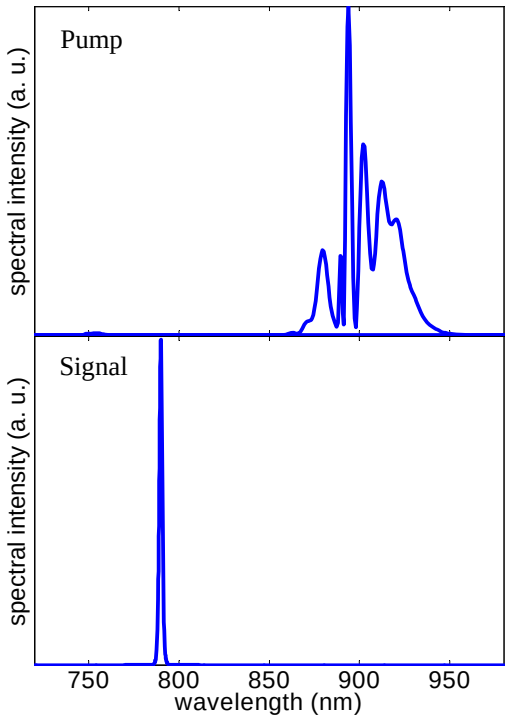

(a)

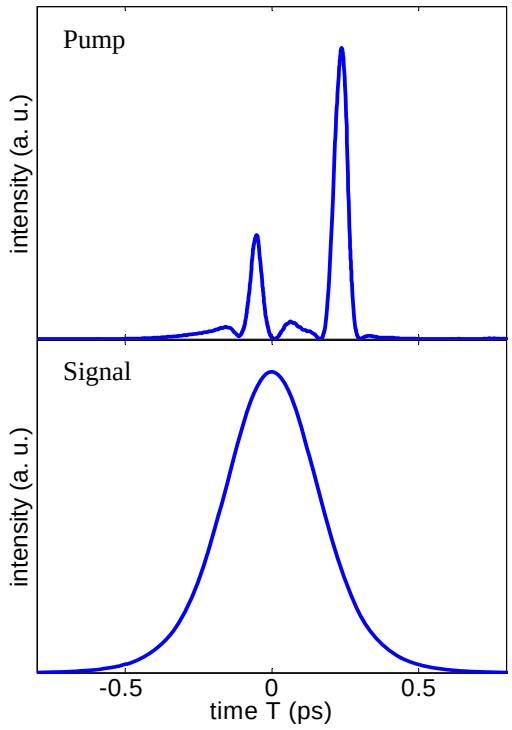

(b)

Fig. 2.4.12 The spectral (a) and temporal (b) properties of the pump and signal pulses without taking cross-phase modulation into account

The figures demonstrate the effect of the cross-phase modulation induced by the pump pulse influences the behavior of the signal pulse quite substantially. Without the presence of the pump pulse, the spectrum of the signal pulse is negligibly broadened, because the signal wavelength is located in the normal dispersion region. However, due to the appearance of the copropagating pump pulse, the signal pulse feels the nonlinear effect induced by the cross-phase modulation, which is responsible for new frequency components generated in the spectrum of the signal pulse.

2.4.7 Four wave mixing

Four wave mixing (FWM) describes a nonlinear process where four waves or photons interact with each other due to the third-order susceptibility in a medium [30-33]. Such a nonlinear process belongs to parametric processes because it modulates the medium parameters, such as the refractive index. The parametric processes also include the effect due to the second-order nonlinearity, such as second harmonic generation and sum-frequency generation [25]. The second-order susceptibility in some crystals (BBO for example) is 12 orders of magnitude higher than the third-order susceptibility, however, in fused silica, an isotropic medium, the second-order susceptibility vanishes and consequently the third-order nonlinearity is responsible for the parametric processes. Despite the smaller value of the third-order nonlinearity, FWM is also an important effect to generate new frequency components in optical fibers due to the intense propagating light.

FWM phenomena can be understood by a quantum mechanical model. An atom is excited into a virtual intermediate state by the simultaneous annihilation of two photons [39]. When the atom jumps back to the ground state it generates two new photons, as shown in Fig. 2.4.13. The life-time of the atom in the virtual excited state, corresponding to the distortion of the electron cloud, is inversely proportional to the virtual state energy and is on the order of one femtosecond. Therefore, annihilation and generation of the photons are approximately instantaneous. The atom remains unchanged after the interaction, hence the rules of conservation of energy (Eq. 2.4.43) and momentum (Eq. 2.4.44) have to be fulfilled during the process:

$$\omega_1 + \omega_2 = \omega_3 + \omega_4 \tag{2.4.43}$$

and

$$\vec{k}_1 + \vec{k}_2 = \vec{k}_3 + \vec{k}_4 . \tag{2.4.44}$$

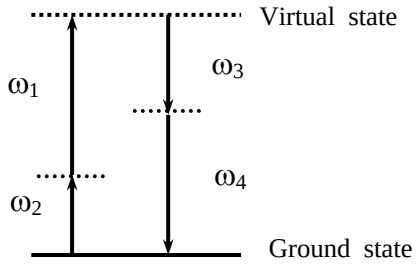

Fig. 2.4.13 Quantum-mechanical description of four wave mixing

The conservation of momentum leads to the phase matching condition. The efficiency of FWM depends very strongly on the phase matching of the frequency components, and consequently relies on the fiber dispersion properties. In tapered fibers, the most often encountered FWM effect during continuum generation is the degenerate FWM process, where two pump photons generate a Stokes and an anti-Stokes photon:

$$2\omega_p = \omega_{st} + \omega_{as}, \tag{2.4.45}$$

where ω_p, ω_{st}, and ω_{as} represent the frequencies of the pump, Stokes, and anti-Stokes photons, respectively. The conservation of momentum, which corresponds to the phase matching condition, is fulfilled with the equation:

$$2\left(\beta_p + \gamma P_0\right)L = \left(\beta_{st} + \beta_{as}\right)L, \tag{2.4.46}$$

where P_0 and γ are the peak power and nonlinear parameter of the pump, respectively, L corresponds to the length of taper waist, and β_p, β_{st}, and β_{as} represent the propagation constants of the pump, Stokes and anti-Stokes photons, respectively. Substituting the expansion of constant β in a Taylor series (see section 2.4.1), we can obtain the final phase matching condition:

$$\frac{\beta_2}{2}\left(\omega_a - \omega_p\right)^2 + \frac{\beta_4}{24}\left(\omega_a - \omega_p\right)^4 + \gamma P_0 = 0, \tag{2.4.47}$$

where only the even terms of the series expansion contribute to the phase matching condition due to the energy conservation as shown in Eq. (2.4.47) and we ignored the higher order dispersion influences.

Figure 2.4.14 shows the phase matching diagrams as a function of pumping wavelengths for a tapered fiber with waist length of 90 mm, waist diameter of 2.1 μm, and zero dispersion wavelength of 730 nm. The dashed blue, solid red and solid black curves represent the phase matching diagrams with pump powers equal to zero, 1 kW and 8 kW, respectively. The phase matching diagrams demonstrate that the pump wavelengths, which are located in the normal-dispersion regime, are phase matched

with a broad range of Stokes and anti-Stokes wavelengths without a requirement for a high power density. In other words, even a small amount of light in the normal-dispersion regime can serve as parametric pump and generates new frequency components. However, in the case where the pump wavelength lies in the anomalous-dispersion regime, the phase matching can be achieved only if the pump power is high enough to compensate the phase mismatch arising from the material dispersion.

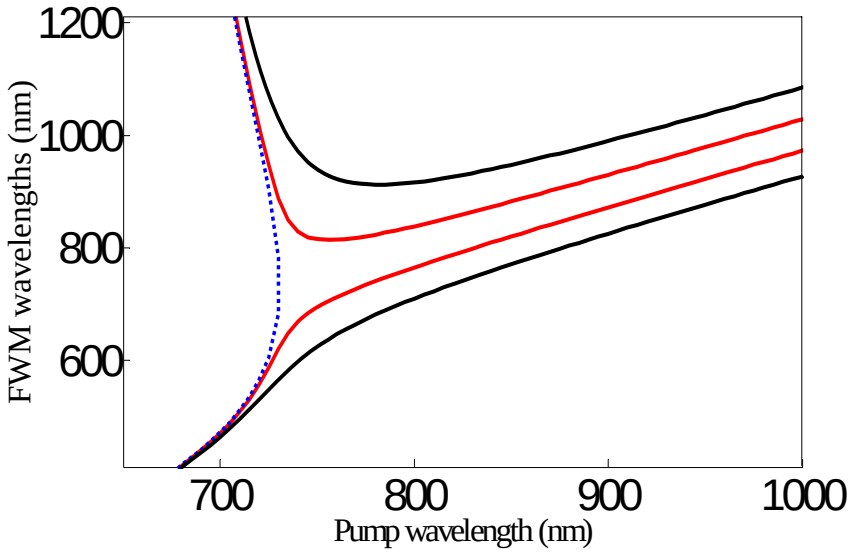

Fig, 2.4.14 The phase matching diagram with peak power of zero (dashed blue), 1 kW (red), and 8 kW (black), respectively.

2.5 Numerical simulation

Generally, a nonlinear partial differential equation, such as the nonlinear Schrödinger equation, has no analytic solutions except for some special cases. A numerical approach is therefore required to solve pulse-propagation problems in optical fibers. In this section, we will concentrate on the numerical simulations of supercontinuum generation. Section 2.5.1 introduces the so called "split-step Fourier method", which is common and efficient to solve a nonlinear partial differential equation. In section 2.5.2, theoretical simulations using the split-step Fourier method will be compared with experimental results.

2.5.1 Split-Step Fourier Method

To study the pulse-propagation problem in tapered fibers and photonic crystal fibers, we applied the split-step Fourier method [25] [45,46] to solve the nonlinear Schrödinger equation. In this section, we will briefly introduce the philosophy behind the method and discuss its implementation in our simulations in detail.

The nonlinear Schrödinger equation, including higher order dispersion, self steepening, and Raman scattering, is expressed in Eq. (2.5.1):

$$\frac{\partial A(z,T)}{\partial z}=\sum_{k=2}\frac{i^{k+1}}{k!}\beta_k\cdot\frac{\partial^k A(z,T)}{\partial T^k}+i\gamma\left(1+\frac{i}{\omega_0}\frac{\partial}{\partial T}\right)\left(A(z,T)\int_{-\infty}^{\infty}R(t')\left|A(z,T-t')\right|^2dt'\right). \tag{2.5.1}$$

We write the Eq. (2.5.1) in the following form:

$$\frac{\partial A(z,T)}{\partial z}=\left(\widehat{D}+\widehat{N}\right)A(z,T), \tag{2.5.2}$$

where

$$\widehat{D}=\sum_{k=2}\frac{i^{k+1}}{k!}\beta_k\cdot\frac{\partial^k}{\partial T^k} \tag{2.5.3}$$

and

$$\widehat{N}=\frac{i}{A(z,T)}\gamma\left(1+\frac{i}{\omega_0}\frac{\partial}{\partial T}\right)\left(A(z,T)\int_{-\infty}^{\infty}R(t')\left|A(z,T-t')\right|^2dt'\right). \tag{2.5.4}$$

The following approximation is made in the split-step Fourier method: Within a small propagation distance, the dispersive and nonlinear effects act on the pulse independently. In the simulations presented in this dissertation, we take three steps to describe the pulse propagation over one segment from z to $z+h$. In the first step, dispersion effects act alone from z to $z+h/2$ and $\widehat{N}=0$; in the second step, the nonlinear effects are included in the middle of the segment, and they act alone from z

to $z+h$; in the third step, dispersion effects act alone from $z+h/2$ to $z+h$. Mathematically, this procedure can be expressed by Eq. (2.5.5):

$$A(z+h,T) \approx \exp\left(\frac{h}{2}\widehat{D}\right)\exp\left(\int_{z}^{z+h}\widehat{N}(z')dz'\right)\exp\left(\frac{h}{2}\widehat{D}\right)A(z,T). \qquad (2.5.5)$$

Under further simplification of the integral, Eq. (2.5.5) is replaced by

$$A(z+h,T) \approx \exp\left(\frac{h}{2}\widehat{D}\right)\exp\left(\frac{h}{2}\left[\widehat{N}(z)+\widehat{N}(z+h)\right]\right)\exp\left(\frac{h}{2}\widehat{D}\right)A(z,T). \quad (2.5.6)$$

To evaluate the exponential operator $\exp\left(\frac{h}{2}\widehat{D}\right)$, we apply the following formula:

$$\exp\left(\frac{h}{2}\widehat{D}\right)A(z,h) = F_T^{-1}\left\{\exp\left[\frac{h}{2}D(-i\omega)\right]F_T\left[A(z,h)\right]\right\}, \qquad (2.5.7)$$

where F_T stands for Fourier-transform operation, $D(-i\omega)$ is the Fourier transform of $\widehat{D}$, and ω is the frequency in the Fourier domain. Since $\widehat{D}(-i\omega)$ is a number instead of an operator, Eq. (2.5.7) can be calculated readily. Using the same method, we obtain the electric field $A(z+h, T)$ at propagation distance $z+h$ as Eq. (2.5.8):

$$A(z+h,T) \approx F_T^{-1}\left\{\exp\left[\frac{h}{2}D(-i\omega)\right]F_T\left[X(z,h)\right]\right\}, \qquad (2.5.8)$$

where $X(z,h) = \exp\left(\frac{h}{2}\left[\widehat{N}(z)+\widehat{N}(z+h)\right]\right)F_T^{-1}\left\{\exp\left[\frac{h}{2}D(-i\omega)\right]F_T\left[A(z,h)\right]\right\}$.

Two difficulties arise when we evaluate the electric field $A(z+h, T)$. First, $\widehat{N}(z+h)$ in the expression of $X(z, h)$ is unknown, since it is a function of electric field $A(z+h, T)$. Second, the integral term in Eq. (2.5.4), which represents the delayed Raman scattering, is hard to evaluate directly. To solve the first problem, we employ an iterative method. $\widehat{N}(z+h)$ in the expression of $X(z, h)$ is initially replaced by $\widehat{N}(h)$ to estimate $A(z+h, T)$, which can be used to evaluate $\widehat{N}(z+h)$. Knowing the value of $\widehat{N}(z+h)$, we can calculate the new value of $A(z+h, T)$. In our simulations, two iterations are implemented. The second problem can be settled by using convolution theory. The integral term in Eq. (2.5.4) is therefore expressed as

$$\begin{aligned}\int_{-\infty}^{\infty} R(t')\left|A(z,T-t')\right|^2 dt' &= \int_0^T R(t')\left|A(z,T-t')\right|^2 dt' \\ &= R(T)\otimes\left|A(z,T)\right|^2 \\ &= F_T^{-1}\left\{F_T\left[R(T)\right]\cdot F_T\left[\left|A(z,T)\right|^2\right]\right\},\end{aligned} \qquad (2.5.9)$$

where the imaginary part of $F_T\left[R(T)\right]$ can be readily obtained by the experimentally measured Raman gain spectrum given in Fig. (2.4.9), and the real part of $F_T\left[R(T)\right]$ can be obtained by using a Kramers-Kronig transform (see section 2.4.5).

So far we are able to implement split-step Fourier method. The program was written using Matlab, where the discrete Fourier transform is straightforward. To obtain reliable results, the time and frequency discretization points are chosen to be 2^{13}, the time window size is 12.868 *ps*, and the longitudinal step size *h* is set to be less than 50 μm.

2.5.2 Comparisons between simulations and experiments in tapered fibers

In the section 2.4.1, a nonlinear Schrödinger equation was derived to describe the propagation characteristics of pulses in tapered fibers. The spectral and temporal properties of the supercontinuum generation can, therefore, be theoretically simulated by solving the NLSE with the split-step Fourier method. However, in the derivation of the equation, some prerequisites were made to simplify the original expression of the equation, such as the generation assumed to be linearly polarized along tapered fibers, the third-order polarization considered negligible compared with the linear effect, and so on. Therefore, to check the validity of such a NLSE, one should compare theoretical simulations with experimental results. For this purpose, we simulated the spectra of the supercontinuum generated by tapered fibers under similar conditions as in the experiment (Fig. 2.2.5) in section 2.2.4.

In the femtosecond range, the nonlinear Schrödinger equation including Raman scattering is written as

$$\frac{\partial A(z,T)}{\partial z}=\sum_{k=2}\frac{i^{k+1}}{k!}\beta_k\cdot\frac{\partial^k A(z,T)}{\partial T^k}+i\gamma\left(1+\frac{i}{\omega_0}\frac{\partial}{\partial T}\right)\left(A(z,T)\int_{-\infty}^{\infty}R(t')\left|A(z,T-t')\right|^2dt'\right). \tag{2.5.10}$$

The tapered fiber used in the experiments has a diameter of 2.1 μm and a waist length of 90 mm, pumped at 770 nm, 800 nm, 840 nm, and 880 nm, respectively. The input power is 200 mW and output power is reduced to 110 mW, hence, it is reasonable to assume the propagating average power to be equal to 110 mW in the taper waist. The pump pulse generated by the Ti:Sapphire oscillator has a repetition rate of 80 MHz, a pulse duration of 200 fs, and a *sech* pulse shape. Recalling the experimental setup, we used a Faraday isolator to prevent backreflections from the fiber into the laser, therefore, in the simulations, the chirp induced by the Faraday

isolator and the untapered region of the fiber should also be taken into account. Figure 2.5.15 shows the output spectral properties of the tapered fibers (a) to (d).

The origin of the dramatic spectral broadening during the SC generation process is the interaction between the fiber dispersion and various nonlinear effects, such as SPM, FWM, self-steepening, and stimulated Raman scattering. The details on the mechanisms responsible for the supercontinuum generation will be discussed in section 2.6.

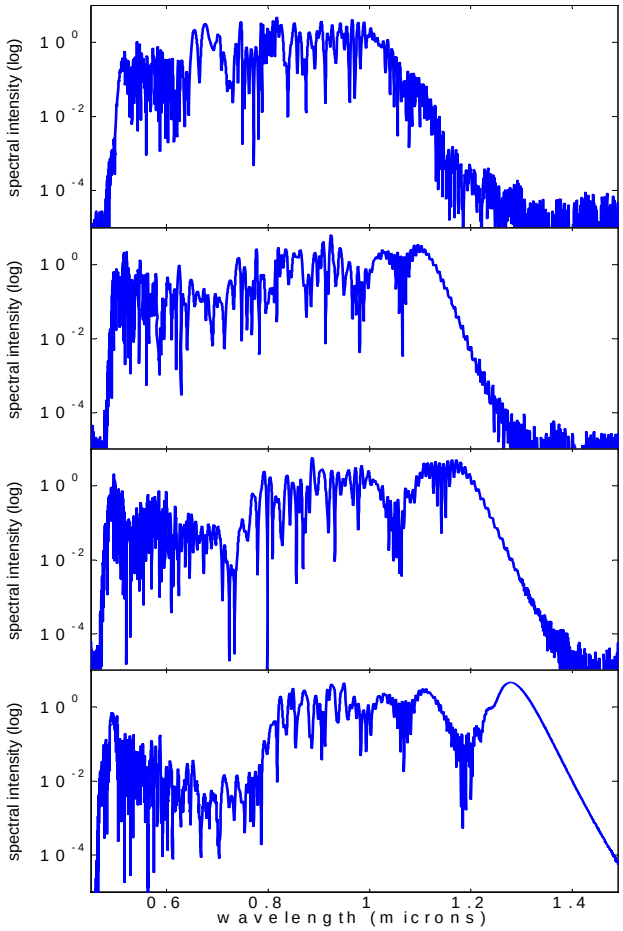

Fig. 2.5.15 Theoretical simulations of spectral properties generated in tapered fibers with diameter of 2.1 μm at different pump wavelength of 770 nm, 800 nm, 840 nm and 880 nm (from top to bottom).

Comparing with the experiment shown in Fig. 2.5.16 (the same as Fig. (2.2.5), see section 2.2.2), we found the theoretical simulations can not only adequately model the width of the generated spectrum but also approximately predict the positions of distinct spectral peaks. Furthermore, pumping the fiber at longer wavelength, both the experimental result and the theoretical simulation illustrate that the generated spectrum is more broadened and the gap in the visible regime is widened. The physics mechanisms responsible for this spectral feature will be also discussed in section 2.6.

However, no simulation method so far can predict exactly the output spectra, as experimental parameters such as polarization cross-coupling, higher-order

dispersion, and the experimental waist profile cannot be measured with the accuracy to precisely simulate the exact spectra.

There are numerous oscillatory structures in the spectra of theoretical simulations, whereas the experimental spectra show more flattened and smoother profiles. We guess that two factors are likely to result in such a difference. First, the oscillating structures could be produced by the algorithm instability of split-step Fourier method. To examine the instability induced by the algorithm, we introduce a noise to the input peak power. We found the structure is not very sensitive to the noise. For example, for a noise with its magnitude 0.1 percent of the original peak power, the average power difference of the generated spectrum is less than one percent. And such a power difference is induced by both the numerical approach and the nonlinearity effects. Through increasing the frequency discretization points or decreasing the longitudinal step size, the algorithm instability can be to a certain extent reduced, but at expense of the running time. Second, the spectra shown in Fig. (2.5.16) were measured by a spectrometer, which records a time-averaged result, and therefore the spectra seem flattened when compared to the theoretical simulations.

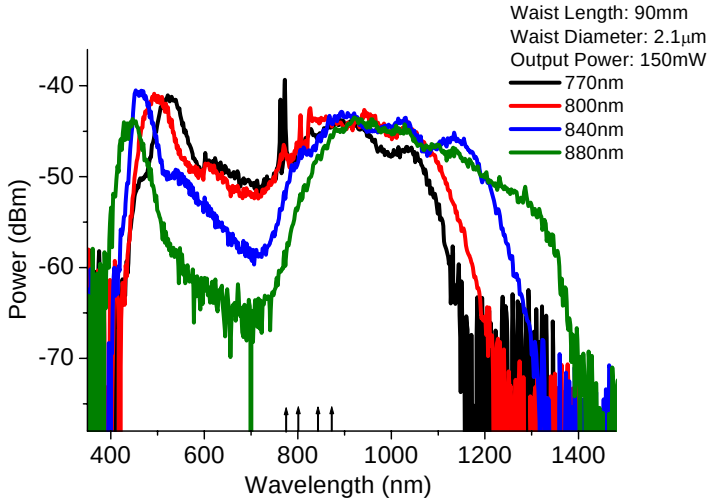

Fig. 2.5.16 The spectra of the supercontinuum generation after one tapered fiber with pumping wavelength of 770 nm (black), 800 nm (red), 840 nm (blue), and 880 nm (green).

2.6 Mechanisms responsible for supercontinuum generation

The supercontinuum generation is a complex nonlinear phenomenon. The mechanisms behind SC generation arise from the interaction between dispersion and nonlinear effects, including self-phase modulation [27-29], soliton formation [58-62], soliton splitting [41-43], self steepening [25], soliton self-frequency shift [72,73] and Raman scattering [32, 38-40]. In this section, we are going to discuss the generation process of supercontinua in detail.

With group velocity dispersion and self-phase modulation alone, the balance between those effects results in the formation of solitons, and at higher amplitudes a higher-order soliton with soliton number N is formed. Such a higher-order soliton undergoes periodic narrowing and broadening during propagation. However, at the presence of perturbations, such as higher-order dispersion, Raman effect, and self-steepening, the soliton is broken up and the initial pulse decays into several sub-pulses which propagate independently as fundamental solitons [40-43,74-76]. Simultaneously, the pulse emits the non-solitonic radiation as a dispersive wave in the normal dispersion region (typically in the blue spectral region), which satisfies the phase matching condition of the fundamental solitons. The fundamental solitons undergo soliton self-frequency shift (SSFS) [72,73], caused by stimulated Raman scattering, and consequently form the distinct red-shifted components in the spectrum. The dispersive wave experiences the cross phase modulation, which is induced by the nonlinear refractive index due to the temporally overlapping Raman solitons [35,37].

To confirm the generation mechanisms as described above, we apply the NLSE to simulate the spectral and temporal properties of the first stages of the continuum formation in different cases. Figure 2.4.16 shows the spectral evolution, when neither the higher-order dispersive terms nor Raman scattering contribution nor self-steepening effect are included. The spectrum recurves into its original form after a soliton period and a higher-order soliton is formed, which is constituted of N fundamental solitons. The tapered fiber, used in the simulation, has a diameter of 3.0 mm and a length of 56.7 mm, which is the soliton period of this fiber. And it is pumped at 950 nm with peak power of 18 kW and pulse duration of 50 fs.

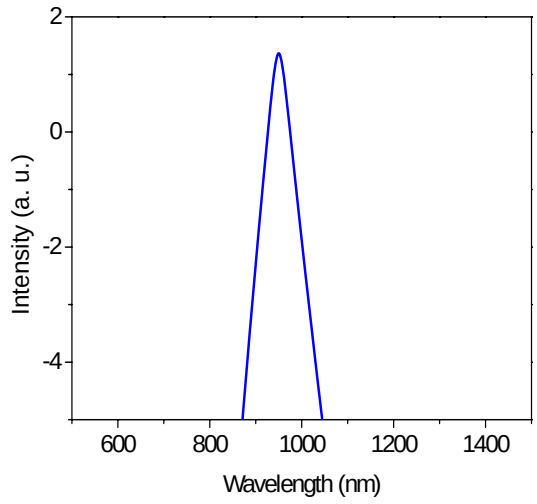

(a)

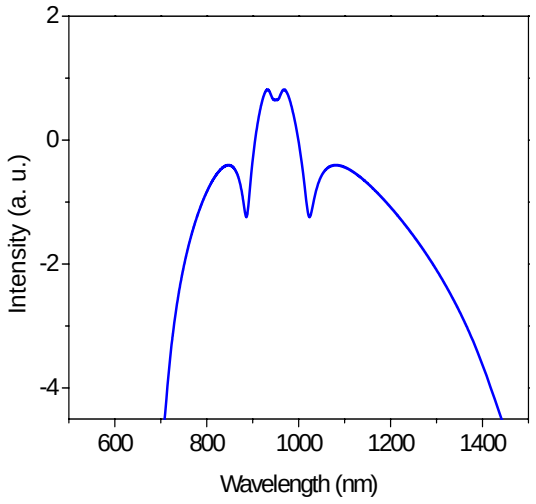

(b)

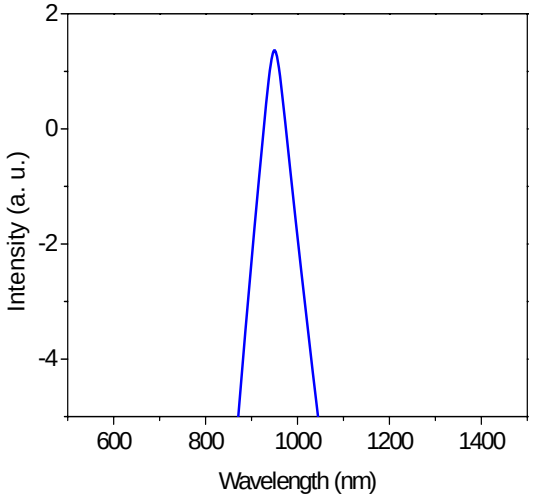

(c)

Fig. 2.4.16. Simulated spectrum of a tapered fiber, without considering higher order dispersion effects and nonlinear effects for (a) input end, (b) at z=0.13 z_0, and (c) at z=z_0 (z_0 is the soliton period).

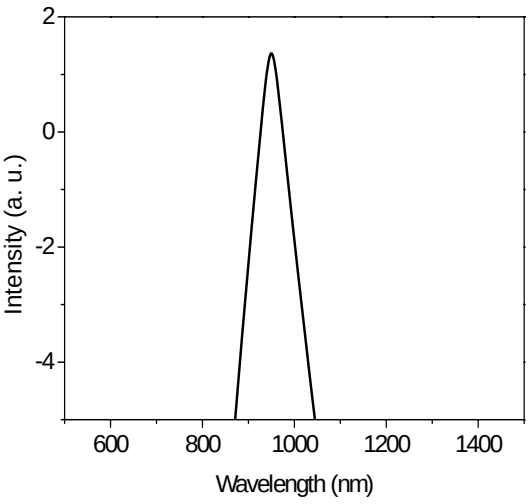

(a)

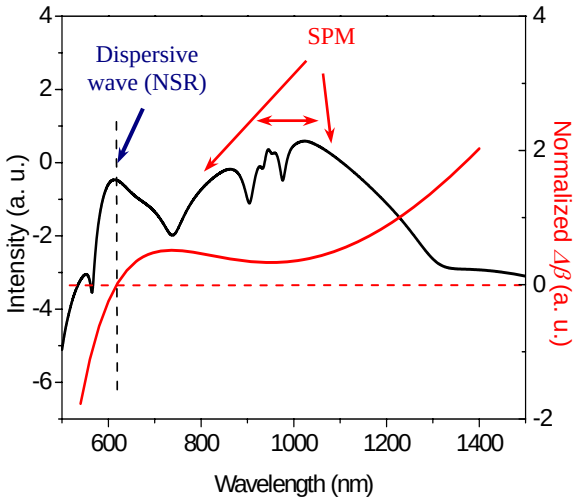

(b)

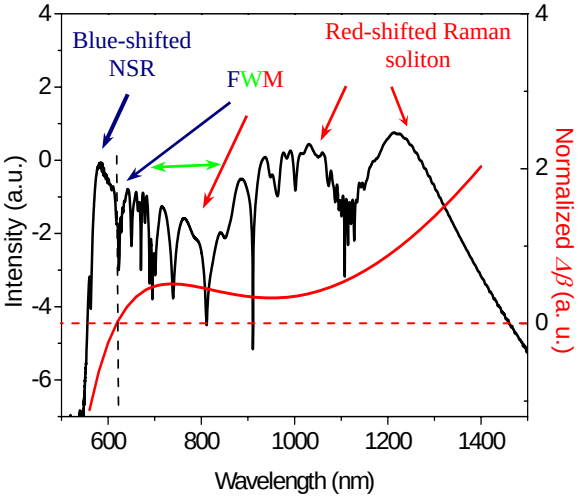

(c)

Fig. 2.4.17. Simulated spectrum of a tapered fiber, with all the dispersion effects and nonlinear effects considered, for (a) input end, (b) at z=0.13 z_0, and (c) at z=z_0 (z_0 is the soliton period).

When including higher-order dispersion, self-steepening term, and Raman term, the initial pulse starts to decay into several solitons. The initial generation of new red-shifted frequency components is induced by stimulated Raman scattering. The blue components around 610 nm, identified as anti-Stokes wave or non-solitonic radiation, arise from the process that the sub-pulses shed away energy in order for the pulse to be able to propagate as fundamental solitons. The phase of the soliton should coincide with that of the dispersive radiation and this phase matching condition can be mathematically expressed by the equation [61]:

$$\Delta\beta = \beta(\omega_S) - \beta(\omega_{DW}) - (\omega_S - \omega_{DW})\beta_1(\omega_S) + (1 - f_R)\gamma P_S \ , \qquad (2.4.48)$$

where, ω_S and P_S are the frequency and peak power of fundamental soliton, respectively, ω_{DW} is the frequency of dispersive wave, and f_R is the Raman fractional contribution equal to 0.18. Subsequently, the fundamental solitons shifts to the red side due to the self-frequency shift, which is induced by Raman effect and higher-order dispersion. The blue components undergo cross-phase modulation and generate the blue-shifted nonsolitonic radiation (NSR). Finally, the spectrum is smoothed by four wave mixing. The details of the generation mechanism are demonstrated in Fig. 2.4.17.

In the simulations of Fig. 2.4.17, we used the same fiber parameters and input conditions as in Fig. 2.4.16. Figure 2.4.17 (a) shows the spectrum of the input pulse. Figure 2.4.17 (b) demonstrates the initial stage of supercontinuum generation, which occurs at position $z=z_0$ (z_0 is the soliton period). It is easily visible that the wavelength of the generated dispersive wave at 618 nm is exactly predicted by the phase matching condition. Fig. 2.4.17 (c) shows the final spectrum of the supercontinuum generation after one soliton period. The blue component at 580 nm is generated by cross-phase modulation due to the nonlinear refractive index of the red-shifted Raman soliton.

As we have discussed in section 2.2 and section 2.6, pumping a fiber at larger wavelength leads to two spectral features. First, the spectrum is more broadened, and second, the gap in the visible region becomes larger. The first feature can be understood by the phase matching condition discussed above. Pumping farther from the zero dispersion wavelength, the pulse generates the nonsolitonic radiation at a shorter wavelength, e.g., with pump wavelength at 950 nm, the dispersive wave occurs at 618 nm, while with pump wavelength at 850 nm the dispersive wave lies around 665 nm. The wavelength of the blue-shifted dispersive wave, which is induced by cross-phase modulation between the nonsolitonic radiation and Raman solitons,

consequently has a smaller value. Therefore the whole spectrum becomes more broadened compared when pumping the fiber closer to the zero dispersion wavelength.

The second feature can be understood by recalling the phase-matching diagram of four-wave mixing. In the case of the pump wavelength located in the anomalous dispersion regime, a tapered fiber pumped closer to the zero dispersion wavelength provides the phase matching for parametric four wave mixing over a wider wavelength range. More specifically, Fig. (2.4.18) shows the phase-matching diagram of four wave mixing at the maximum peak power P_{max} when the pulse propagates along the fiber. The zero dispersion wavelength is located at 830 nm. The figure demonstrates that with the fiber pumped at 850 nm, four wave mixing generates a pair of new frequency components at 680 nm and 1120 nm at the maximum peak power P_{max}. In other words, when the pulse propagates with a peak power smaller than P_{max}, the generated new components resulting from FWM can to a certain extent fill the frequency regime between 680 nm and 1120 nm. Similarly, when the fiber is pumped at 950 nm, the new frequency components due to four wave mixing range from 850 nm to 1090 nm. Therefore, at the presence of four wave mixing, a tapered fiber pumped at a wavelength closer to zero dispersion wavelength can generate a more broadened and smoother spectrum to fill the gap in the visible region. Moreover, pumping the fiber at a shorter wavelength, the fiber has a smaller value of the group velocity dispersion (GVD), so that the pulse in initial stage can generate a broader continuum due to increased self-phase modulation. The smaller wavelength components in the SPM-induced spectrum lead to the generation of new components, resulting from four wave mixing. These new frequency components help to fill the gap in the visible region as well.

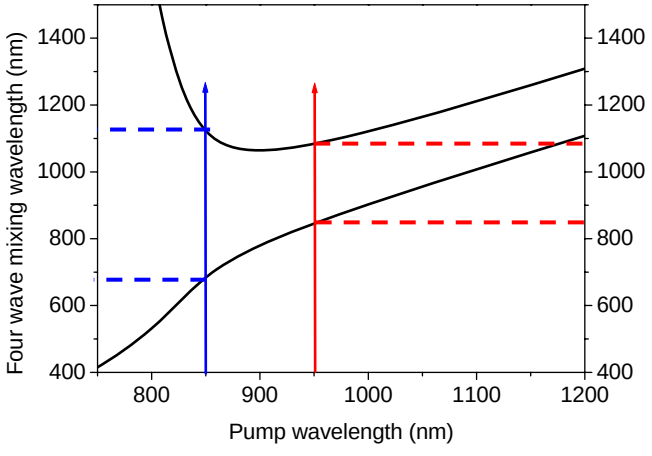

Fig. 2.4.18 Phase-match diagram of four wave mixing.

Section 3 Mode and group velocity dispersion evolution in the tapered transition region [21]

3.1 Introduction

So far, most publications have concentrated on the *waist region* of the tapered fibers, where the strongest nonlinear effect is induced, and assume that the waist can be approximated by a constant diameter silica strand surrounded by air, having similar properties to a high air fill fraction PCF. However, a complete model of the propagation characteristics must take into account the transition or the taper region where the diameter is varying along the fiber.

All of the nonlinear processes engaged in the supercontinuum (SC) generation take place over the whole fiber, including the input and the output tapers. Comprehensive understanding of the nonlinear properties in the taper is of great importance for a complete picture of the generation of SC and its interaction with the pump. Characterization of the pulse and dispersion properties of the SC after exiting the fiber should also include the contribution from the output taper. Especially when the tapered fiber is inserted into a feed-back scheme, acting as nonlinear element in an optical parametric amplifier or oscillator [77], the SC will have to pass through both the input and the output tapers several times and consequently experiences more nonlinearity and dispersion from the tapers. The nonlinear characteristics of both tapered regions will influence significantly the amplification or oscillation processes. Additionally, in experimental GVD measurements, due to the unknown GVD value in the tapers it is difficult to compare the directly measured GVD value along the whole tapered fiber and the theoretical GVD value of the waist. Therefore, the investigation of the mode and the GVD evolution in the taper region is significant for a comprehensive understanding of the light propagation and interaction in the fiber.

In this section, we present theoretical studies of the evolution of the mode profile and the GVD in the taper region. To characterize the most important parameters as mentioned above, we first need to evaluate the propagation constant β.

There are generally two theoretical models to describe the propagation of light in tapered fibers: scalar wave equation and full vector Maxwell equation. In the scalar wave equation, the polarization of the field is assumed to be unchanged and the longitudinal component is ignored [55,78,79]. However, with the fiber tapered down, the polarization of the light varies with propagation, and the longitudinal component

of the mode fields increases even to the same order of magnitude as the transverse components [80]. Therefore, the vector model can provide a more precise description of the light propagation.

Our calculation shows that the nonlinear parameter based on the field distribution is not sensitive to the difference between the scalar equation and the vector equation models when the diameter of the tapered fiber is larger than 1.0 μm. In this paper, we restrict our discussion to fiber tapers with a diameter larger than 1.8 μm, and we used the scalar equation to calculate β in order to simplify the calculation of the mode evolution. In contrast, the GVD, which is actually the second-order derivative of β, is extremely sensitive to any approximations in the model when the diameter of the taper becomes rather small. In this case, we used the full vector Maxwell equation to simulate the evolution characteristics of GVD in the tapered region.

Furthermore, when simulating the mode evolution, we also compared the results from the standard solution of the scalar wave equation with those obtained from the so-called “variational calculation” [55], which is in fact an approximation to the scalar equation.

3.2 Evolution of the radial distribution of the light intensity and the nonlinear parameter in the taper

3.2.1 Standard solution of the scalar equation

For an adiabatic process [78] in a tapered fiber, the perturbation caused by the variation of the fiber radius is so small that the loss of power from the fundamental mode to the higher-order mode in the fiber is negligible [3, 78]. In this paper, we assume the fiber is an adiabatic single-mode tapered fiber.

In such a fiber, the light propagates always as a fundamental mode. For a given position *z* along the taper, we can build the fundamental-mode wave equation in a cylindrical system by making use of the geometry of the local profile (see Fig. 3.2.1).

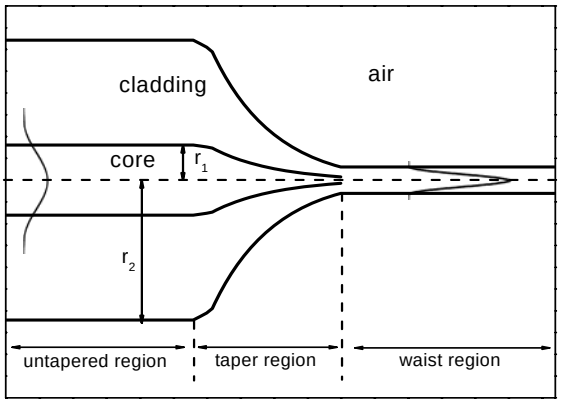

Fig. 3.2. 1. Radial profile along the input tapered fiber.

To obtain the radial distribution of intensity, which is a function of the propagation constant β, we need to solve the scalar wave Eq. (3.2.1).

$$r^2\frac{\partial^2\psi}{\partial r^2}+r\frac{\partial\psi}{\partial r}+[r^2(n^2k_0^2-n_{eff}^2k_0^2)-m^2]\psi=0, \tag{3.2.1}$$

where Ψ is the transverse electric field, and *m* is equal to zero for the fundamental mode LP_{01}.

The solution of this equation can be expressed by a linear composition of Bessel functions and modified Bessel functions. Using the boundary conditions that the wave function and its first derivative are continuous at the core-cladding and cladding-air interfaces, we can obtain the propagation constant of the fundamental mode at each position *z*. In Fig. 3.2.2, the color-scaled contour shows the evolution of the normalized radial distribution of intensity along the fiber at a wavelength of 800 nm.

The red lines in the graph describe the core-cladding and cladding-air interfaces. The variation of the radius of the cladding can be described by:

$$r_{cladding}(\mu m) = -1.9 + 67.8 \cdot \exp(-z/4.7), \tag{3.2.2}$$

which is a fit to measured data (with z in mm) [20]. We have assumed that the ratio between the radius of the cladding and the core remains constant (around 15.2) during the pulling process. The Sellmeier equation for the cladding is $n_{cladding}(\lambda) = \sqrt{3.0 + 0.009/(\lambda^2 - 0.01) + 84.1/(\lambda^2 - 96.0)}$ with λ in μm. The refractive index difference between the cladding and the core is 0.36%. In the simulation of the mode evolution, we assume that power is conserved: $\int_0^{2\pi}\int_0^{\infty} \frac{1}{2}\mathrm{Re}\left(\vec{E}\times\vec{H}^*\right) r\,dr\,d\phi = const.$, and the ratio between the transverse electric field and transverse magnetic field is approximated as μ_0/ε.

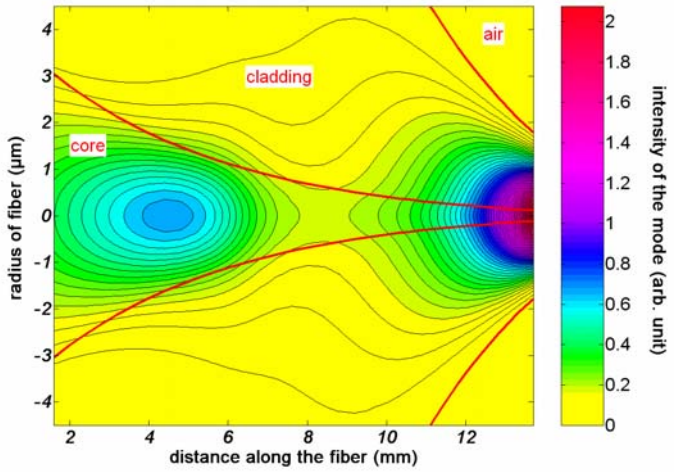

Fig. 3.2.2. The evolution of the radial distribution of intensity along the input taper region of SMF 28 fused silica tapered fiber (at 800 nm).

At the beginning of the taper region, the light propagates as a core mode and most of the energy is confined within the core. As the fiber is tapered down, the difference between the refractive indices of the core and the cladding is not large enough to confine the mode in the core. Therefore, the light begins to spread out into the cladding and propagates as a cladding mode that is guided by the boundary between the cladding and the air. As a result, the energy redistributes into the cladding and the intensity of the light decreases due to the relatively large diameter of the cladding. As the fiber is tapered down further, the intensity of the mode, which is now confined by the cladding-air interface, increases again due to the rather small radius of the cladding and reaches its highest magnitude at the end of the taper. The position

where the propagation mode transfers from the core mode to the cladding refers to as the transition point, or the so-called 'core-mode cut off' [81]. Furthermore, the evolution of the mode and the process of the light propagation in the output taper region are mirror symmetric to Fig. 3.2.2 about the waist.

The evolution described above depends significantly on the pump wavelength. Figure 3.2.3 (a) and (b) demonstrate the evolution processes for wavelengths at 500 nm and 1064 nm, respectively.

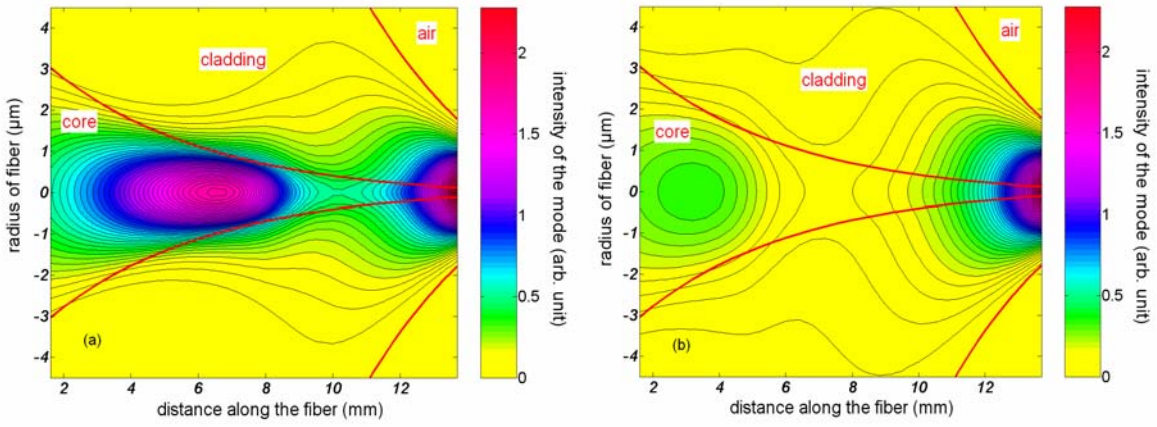

Fig. 3.2.3. The evolution of the radial distribution of intensity along the taper at (a) 500 nm and (b)1064 nm.

At shorter wavelength, the mode can be confined to a smaller core and propagates as a core mode over a longer distance compared to the mode at longer wavelength. For a given tapered fiber, the value of core-cladding transition parameter V_{cc}, which is given by [81],

$$V_{cc} \approx \sqrt{\frac{2}{\ln s}}\left(1+\frac{0.26}{\ln s}\right)^{-\frac{1}{2}}, \tag{3.2.3}$$

where s is the ratio between the radius of the cladding and the core, does not depend on the wavelength. The local V-value of the core at position z is a function of wavelength and can be expressed as $V_{core}(z)=\frac{2\pi \cdot r_{core}(z)}{\lambda}\cdot\sqrt{\left(n_{core}^2-n_{cladding}^2\right)}$. When $V_{core}(z)$ is larger than the critical parameter V_{cc}, the light propagates as a core mode. At the transition point, where $V_{core}(z)$ is equal to V_{cc}, the local V-value of the core $V_{core}(z)$ becomes too small to confine the core mode any more, therefore, when $V_{core}(z)$ is smaller than V_{cc}, the cladding becomes the new guiding medium and the light propagates as a cladding mode. Therefore, for a smaller wavelength, to match the

core-cladding transition point, the radius of the core should be smaller than that for a longer wavelength.

Knowing the transverse distribution of the mode along the taper, we can evaluate the nonlinear parameter γ that is important for the understanding of the nonlinear properties in the tapered region. γ is defined as $n_2 \omega_0 / c A_{eff}$ [55], inversely proportional to the effective area of the mode A_{eff} that is related to the modal distribution function $E(r,\phi)$ as:

$$A_{eff} = \frac{\left(\int_0^{2\pi} \int_0^{\infty} |E(r,\phi)|^2 \, r \, dr \, d\phi \right)^2}{\int_0^{2\pi} \int_0^{\infty} |E(r,\phi)|^4 \, r \, dr \, d\phi}, \tag{3.2.4}$$

where n_2 is the nonlinear refractive index of the fiber material, ω_0 and c are the given frequency and the speed of light in vacuum, respectively. Figure 3.2.4 (a) and (b) illustrate the evolution of the effective area A_{eff} and the nonlinear parameter γ along the SMF 28 fused silica tapered fiber at different pump frequencies.

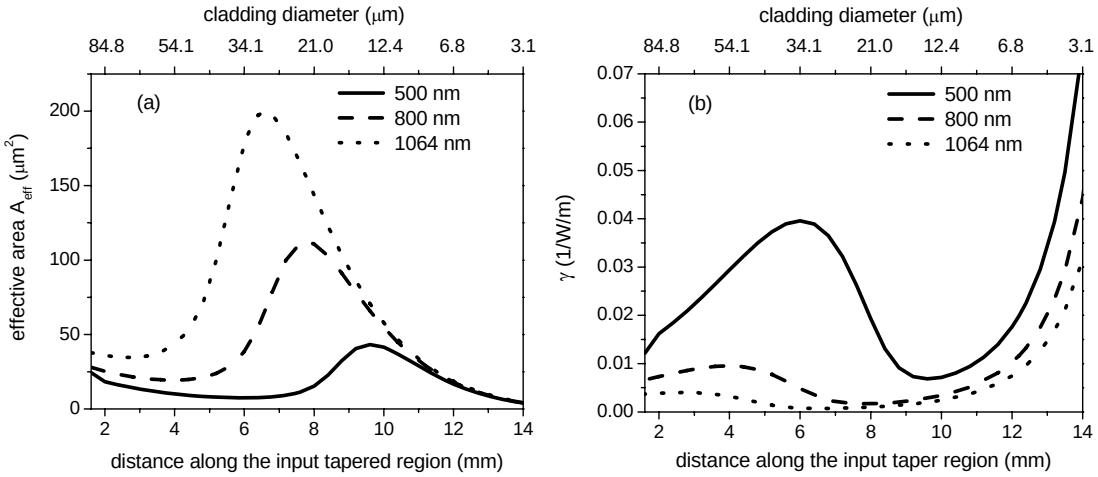

Fig. 3.2.4. The evolution of (a) effective area and (b) nonlinear parameter γ along the SMF 28 fused silica fiber.

Figure 3.2.4 (a) demonstrates that the effective area increases with the wavelength around the transition point and this transition point appears earlier at longer wavelengths. Thus, the nonlinear parameter γ becomes larger at shorter wavelengths and the peak value of γ shifts to the waist direction with shortening the wavelength, as demonstrated in Fig. 3.2.4 (b). Figure 3.2.4 (b) shows nicely that the value of the nonlinear parameter early in the taper becomes comparable with that in the waist, for example at a wavelength of 500 nm, which implies that nonlinear processes such as self phase modulation and four-wave mixing can already take place

before the transition point. This effect leads to a wavelength dispersion of the nonlinear parameter γ and the transition points. It will consequently influence the propagating supercontinuum in the output taper region, so that different wavelengths will experience different nonlinear interactions and different time-dependent propagation characteristics.

3.2.2 Variational calculation

We also performed "variational calculation" [8], where we assumed a Gaussian distribution for the fundamental mode $\psi(r) = \frac{\sqrt{2}}{w} e^{-(r/w)^2}$, which proved to be a good approximation to the true ground state radial distribution if we were not too close to the transition point. The effective width of the Gaussian mode is obtained by maximizing $\left\langle \beta^2 \right\rangle \equiv \left\langle {n_{eff}}^2 {k_0}^2 \right\rangle = \int_0^\infty dr\, r \psi(r) \left(\frac{1}{r} \frac{\partial}{\partial r} r \frac{\partial}{\partial r} + n^2(r) k_0^2 \right) \psi(r)$.

Using $\frac{d\left\langle \beta^2 \right\rangle}{dw} = 0$ and solving the subsequently derived equation with respect to *w*,

$$1 = r_{core}^2 k_0^2 e^{-(r_{core}/w)^2} (n_{core}^2 - n_{cladding}^2) + r_2^2 k_0^2 e^{-(r_{cladding}/w)^2} (n_{cladding}^2 - n_{air}^2), \qquad (3.2.5)$$

we calculated the value of *w* directly.

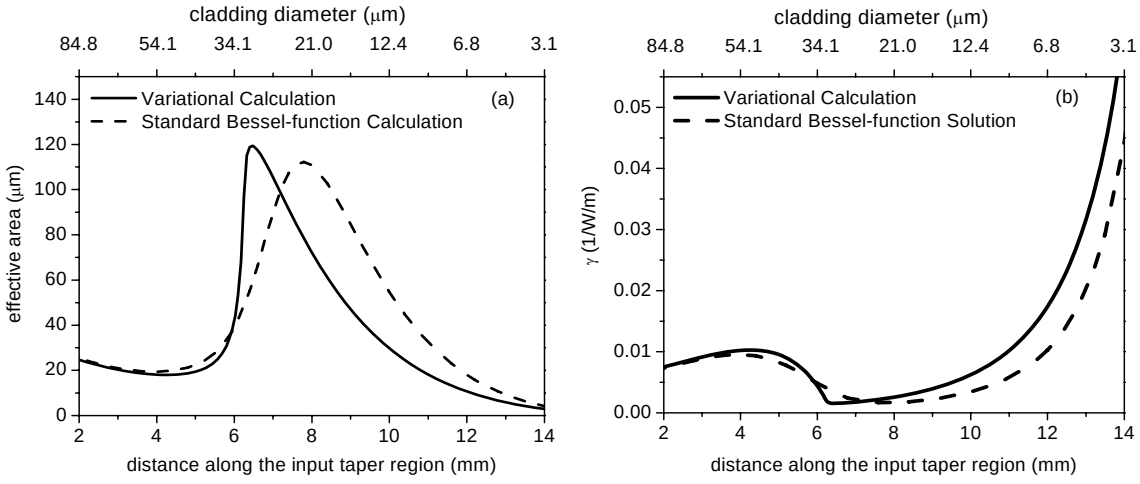

Fig.3.2.5. The evolution of (a) effective area and (b) nonlinear parameter γ, obtained by the variational calculation and the calculation of standard Bessel differential equation, respectively.

Figure 3.2.5 (a) and (b) show the evolution of the effective mode area and the nonlinear parameter γ along the tapered fiber at 800 nm obtained by the variational calculation and the standard Bessel-function solution, respectively.

Qualitatively, these two methods give approximately similar results considering their overall distribution and the shapes of the curves in Fig. 3.2.5 (a), especially at the edges of the taper. The largest discrepancy between them is around the transition point due to the Gaussian-distribution ansatz along the whole taper region.

Nevertheless, the variational theory is an effective method for approximately solving the scalar wave equation and a useful tool for analysing the transverse mode evolution in tapered fibers.

3.3 Evolution of the group velocity dispersion in the taper

In order to fully characterize the propagation in a tapered fiber, we have to include the GVD in the taper region, which is defined as:

$$D = -\frac{2\pi c}{\lambda^2}\frac{d^2\beta}{d\omega^2}, \tag{3.3.1}$$

where β is the propagation constant at a given frequency ω, λ is the corresponding wavelength, and c is the speed of light in vacuum. β can be derived by solving Eq. (2.3.11).

Following the standard approach of Snyder and Love [55], we obtain the solutions of the longitudinal components (E_z and H_z) in the taper region.

In the core, where $r < r_1$ (r_1 is the radius of the core), we get:

$$\begin{pmatrix} E_{z1} \\ H_{z1} \end{pmatrix} = \begin{pmatrix} A_1 \\ A_2 \end{pmatrix} J_m(k_0\sqrt{n_{core}^2 - n_{eff}^2}\cdot r)\begin{pmatrix} \sin m\phi \\ \cos m\phi \end{pmatrix}, \tag{3.3.2}$$

where A_1 and A_2 are constants, $k_0=2\pi/\lambda_0$ is the wave number, n_{core} is the refractive index of the core, $n_{eff}=\beta/k_0$ is the effective index, m=1 for the fundamental mode HE_{11}, and J_m is the m^{th} order Bessel function of the first kind. E_{z1} and H_{z1} are the longitudinal components of the electric and the magnetic field in the core, respectively.

In the cladding, where $r_1 \le r \le r_2$ (r_2 is the radius of the cladding), the light can propagate either as a core mode or a cladding mode. This is determined by the local fiber profile. For a core mode, the effective index n_{eff} has a value between the refractive indices of the core and the cladding. For a cladding mode, n_{eff} is smaller than the refractive index of the cladding. The position where n_{eff} is exactly equal to $n_{cladding}$ refers to as the transition point. Therefore, when the light propagates along the taper, n_{eff} undergoes a transition from a value larger than $n_{cladding}$ to a value smaller than it.

If $n_{eff} > n_{cladding}$, the solutions can be written as:

$$\begin{pmatrix} E_{z2} \\ H_{z2} \end{pmatrix} = \begin{pmatrix} B_1 \\ B_2 \end{pmatrix} I_m(k_0\sqrt{n_{eff}^2 - n_{cladding}^2}\cdot r)\begin{pmatrix} \sin m\phi \\ \cos m\phi \end{pmatrix} + \begin{pmatrix} C_1 \\ C_2 \end{pmatrix} K_m(k_0\sqrt{n_{eff}^2 - n_{cladding}^2}\cdot r)\begin{pmatrix} \sin m\phi \\ \cos m\phi \end{pmatrix}. \tag{3.3.3}$$

If $n_{eff} < n_{cladding}$, the solutions become

$$\begin{pmatrix} E_{z2} \\ H_{z2} \end{pmatrix} = \begin{pmatrix} B_1 \\ B_2 \end{pmatrix} J_m(k_0\sqrt{n_{cladding}^2 - n_{eff}^2}\cdot r)\begin{pmatrix} \sin m\phi \\ \cos m\phi \end{pmatrix} + \begin{pmatrix} C_1 \\ C_2 \end{pmatrix} Y_m(k_0\sqrt{n_{cladding}^2 - n_{eff}^2}\cdot r)\begin{pmatrix} \sin m\phi \\ \cos m\phi \end{pmatrix}, \tag{3.3.4}$$

where B_1, B_2, C_1, C_2 are constants, $n_{cladding}$ is the refractive index of the cladding, I_m and K_m are the modified Bessel functions of the first kind and the second kind, respectively, and Y_m is the Bessel function of the second kind. E_{z2} and H_{z2} are the

longitudinal components of the electric and the magnetic field in the cladding, respectively.

In the air, where $r > r_2$, $n_{eff} > n_{air}$, we get:

$$\begin{pmatrix} E_{z3} \\ H_{z3} \end{pmatrix} = \begin{pmatrix} D_1 \\ D_2 \end{pmatrix} K_m(k_0\sqrt{n_{eff}^2 - n_{air}^2}\cdot r)\begin{pmatrix} \sin m\phi \\ \cos m\phi \end{pmatrix}, \tag{3.3.5}$$

where D_1, D_2 are constants, and n_{air} is the refractive index of the air. E_{z3} and H_{z3} are the longitudinal intensities of the electric and the magnetic field in the air, respectively.

By substituting the expressions of E_z and H_z into the equations of the relationships between field components [8], we can obtain all the transverse components of the field. Using the boundary conditions,

$$\begin{aligned} &E_{z1} = E_{z2},\ H_{z1} = H_{z2},\ E_{\phi 1} = E_{\phi 2},\ H_{\phi 1} = H_{\phi 2} \qquad \text{at } r = r_1, \\ &E_{z2} = E_{z3},\ H_{z2} = H_{z3},\ E_{\phi 2} = E_{\phi 3},\ H_{\phi 2} = H_{\phi 3} \qquad \text{at } r = r_2, \end{aligned} \tag{3.3.6}$$

we can build up an 8×8 homogeneous matrix equation where those constants are the variables. In order to get a set of non-zero solutions for the variables, the determinant of this matrix should be zero. Finally, we can obtain the result of the propagation constant by finding the roots of the determinant numerically. The GVD of a tapered fiber can then be calculated according to the formula given in Eq. (3.3.1).

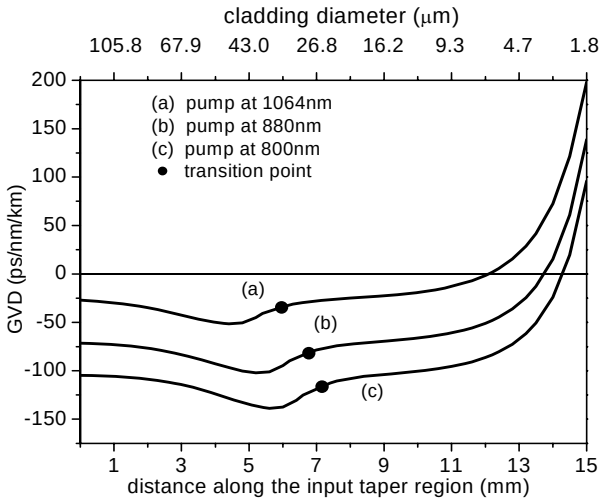

Fig. 3.3.1. The evolution of the GVD along a tapered SMF 28 fused silica fiber, with a waist diameter of 1.8 μm, pumped at (a) 1024 nm, (b) 880 nm and (c) 800 nm. The black dot denotes the transition point from core mode to cladding mode.

Figure 3.3.1 shows the evolution of the GVD as a function of position along the taper for different wavelengths. The GVD values range between –150 and +200 ps/nm/km. We assume an SMF 28 fiber (Corning) to be tapered down to a waist

diameter of 1.8 μm. The variation of the radius of the cladding follows Eq. (3.2.2) and the other parameters of the fiber profile are the same as discussed in Section 3.2.1.

The theoretical calculation also shows that when the cladding diameter of the fiber is larger than 6.3 μm, the GVD value of the taper obtained from the full vector Maxwell equation is almost equal to that from the scalar equation, and the difference between them is less than 1%, as marked by the dashed line in Fig. 3.3.2 (a). Therefore, for a fiber with a cladding diameter larger than 6.3 μm, we can simply use the scalar equation to evaluate the GVD with sufficient precision. However, when the outer diameter becomes smaller than 6.3 μm, the difference increases significantly and cannot be neglected anymore. In Fig. 3.3.2 (a), we compare the evolution of the GVD values that are calculated by the vector Maxwell equation and the scalar equation, respectively, where the pump wavelength is 800 nm and the cladding diameter varies from 9.3 μm to 1.8 μm.

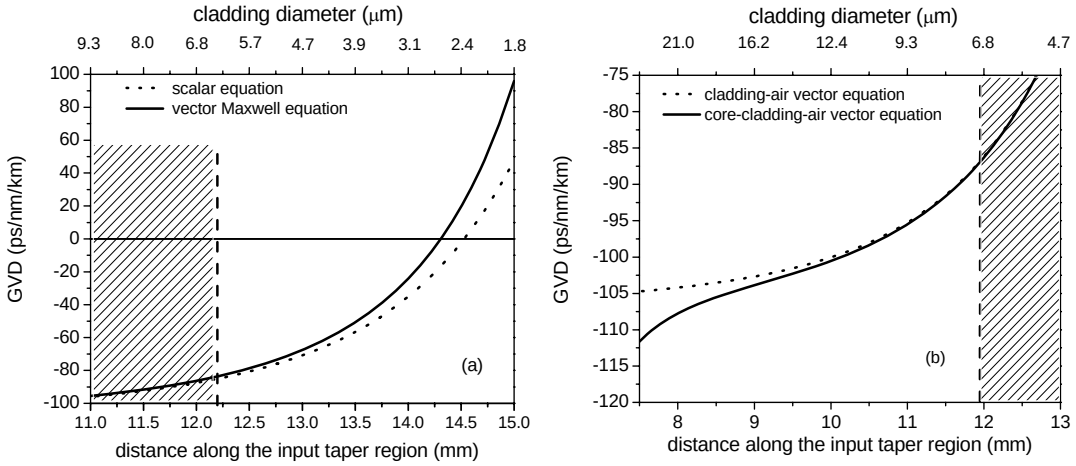

Fig. 3.3.2. The evolution of GVD, estimated by (a) the vector Maxwell equation (solid) and the scalar equation (dotted) and (b) the cladding-air vector equation (dotted) and the core-cladding-air vector equation (solid).
The hatched area denotes the region where the difference between the equations is less than 1% and the wavelength is 800 nm.

When the core of the fiber becomes so thin that its influence on the intensity distribution can be neglected, the fiber can be considered to consist of only the cladding, and we define the corresponding model as cladding-air model. The full vector Maxwell equation, which is named as the core-cladding-air vector equation here, can be replaced by the cladding-air vector equation. Calculations show that when the diameter of the fiber is smaller than 6.9 μm, the difference between the GVD values calculated from the two vector equations does not exceed 1%, as marked by the dashed line in Fig. 3.3.2 (b). The two curves in Fig. 3.3.2 (b) show the evolution of the GVD along the tapered fiber, which are calculated by the cladding-air

vector Maxwell equation and the core-cladding-air equation, respectively. The pump wavelength is 800 nm, and the diameter of the taper changes from 25.5 μm to 4.7 μm.

We conclude for the fiber SMF 28 that when the diameter of the tapered fiber is larger than 6.3 μm, the scalar equation can be used as a reasonable approximation to replace the full vector Maxwell equation, and when the diameter decreases below 6.9 μm, the cladding-air vector equation can simplify the full vector equations with sufficient precision.

Section 4 Group velocity dispersion with tapered fibers immersed in different liquids [24]

4.1 Introduction

As we discussed in section 2.6, the most important mechanism responsible for spectral broadening is the so-called soliton splitting [41-43], taking place around the zero points of the group velocity dispersion (GVD) and in the anomalous dispersion region where the GVD parameter becomes positive. In principle, the zero dispersion points of the tapered fiber determine the region of spectral broadening, and the GVD characteristics controls the shape and the bandwidth of the broadened spectrum. In order to have a supercontinuum generated in the desired spectral range, one usually needs to design the diameter and the material of the fiber core and the cladding in a way that the zero dispersion point occurs at the appropriate wavelength. Furthermore, we usually desire a homogenous broadening of the spectrum to the largest extent. Therefore, an extremely slow variation with small GVD values in the anomalous dispersion region is of key importance. For photonic crystal fibers, ultra-flat dispersion had been demonstrated by Reeves *et al.* [82], and the zero-dispersion wavelength of the GVD can be determined by the structure of the fiber. However, for tapered fibers, such a GVD design has not been realized so far. For example, to extend or shift the generation of new spectral components to the infrared, covering for instance the telecommunication window from 1.3 μm to 1.55 μm, a much larger diameter fiber (over 10 μm) would be required for a tapered quartz fiber. Such a thick fiber will result in much lower light intensity in the tapered region and hence a considerably reduced nonlinearity for the conversion process. Certainly, the second point of zero dispersion at longer wavelength can also be used for the generation in the infrared [1][4][37]. In such a case, a much thinner fiber waist (d=1-1.1 μm) has to be used, which means more difficulties in the fabrication process and a lower damage threshold of the tapered fibers.

In this section, we demonstrate a considerably simple way to control the GVD characteristics of a tapered fiber. We fill the environment of the tapered fiber with a selected chemical liquid which provides a suitable refractive index [83]. By changing the diameter of the tapered fiber and by using different chemical liquids with varying mixture ratios, we optimize the design of the GVD curve. And spectrum simulation demonstrates that such a fiber is capable to generate the supercontinuum with

dramatically broadened spectrum due to the two zero dispersion wavelengths lying in the near infrared region.

4.2 Group velocity dispersion of a tapered fiber

The GVD of a tapered fiber is defined as the second derivative of the propagation constant β with respect to ω, $D = -\frac{2\pi c}{\lambda^2}\frac{d^2\beta}{d\omega^2}$. When talking about the GVD in the paper, we always refer to the value *D*. β can be characterized theoretically by solving the propagation equation in fibers [13]:

$$\left[\frac{J_m'(\kappa a)}{\kappa J_m(\kappa a)}+\frac{K_m'(\gamma a)}{\gamma K_m(\gamma a)}\right]\left[\frac{J_m'(\kappa a)}{\kappa J_m(\kappa a)}+\frac{n_2^2}{n_1^2}\frac{K_m'(\gamma a)}{\gamma K_m(\gamma a)}\right]=\left[\frac{m\beta k_0(n_1^2-n_2^2)}{a\kappa^2\gamma^2 n_1}\right]^2, \qquad (4.2.1)$$

where $\kappa^2 = n_1^2 k_0^2 - \beta^2$; $\gamma^2 = \beta^2 - n_2^2 k_0^2$; a is the core radius; n_1, n_2 are the refractive indices of core and cladding, respectively; $J_m(x)$ and $K_m(x)$ are the m^{th} order Bessel function and modified Bessel function, respectively. *m*=1 corresponds to the fundamental mode HE_{11} in the waist region.

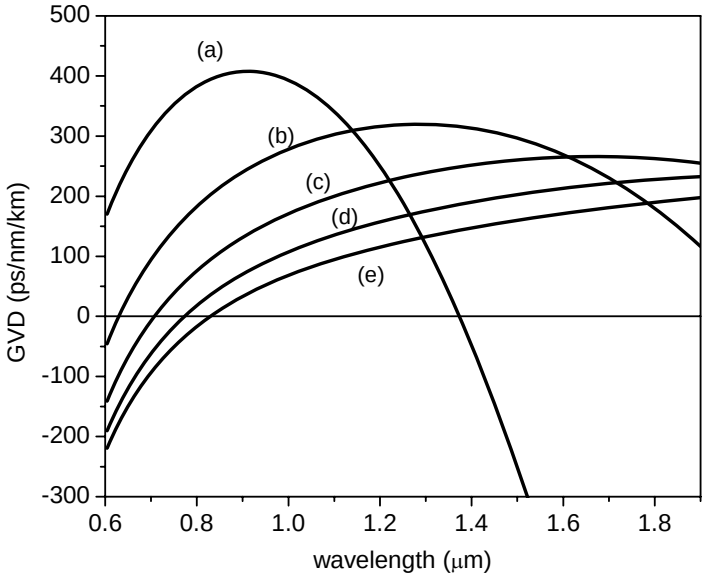

Fig. 4.2.1. The calculated GVD curve of a tapered SMF28 fused silica fiber in air with diameter (a) 1 μm, (b) 1.5 μm, (c) 2 μm, (d) 2.5 μm, and (e) 3 μm

The GVD curves as a function of wavelength for tapered fibers made out of fused silica SMF28 fibers in air with different diameters are shown in Fig. 4.2.1. We used the Sellmeier equation for fused silica for the values of the refractive index n from Smith [84]. The GVD values are quite large in the anomalous-dispersion regime, ranging in the order of 200 ps/km/nm; meanwhile, the first zero dispersion points do not exceed a wavelength of 800 nm for a fiber diameter below 3 μm. This phenomenon, caused by the large difference between the refractive indices of the fiber

material and air, limits the position and the extent of spectral broadening. To achieve supercontinuum generation in the spectral range of longer wavelengths and to extend the bandwidth, we should find media with intermediate refractive index values between n_{air} and n_{fiber} to fill the environment of the fiber taper. Organic chemical liquids are promising candidates for this task.

4.3 Refractive indices and dispersion of some chemical liquids

I and my colleague Jörn Teipel measured the refractive indices of acetonitrile, pentane, and hexane in the visible spectral region using an Abbe Refractometer, as summarized in Table 4.3.1. Limited by the instrument, we were not able to perform the measurement in the infrared. Equations (4.3.1)-(4.3.3) are the fitted Sellmeier equations for the three chemicals using the measurement data. For acetonitrile, we combined the measurement data in the infrared (from 1200 nm to 2000 nm) given in Ref. [85] with our measurement in the visible. Unfortunately, no data in the IR are available so far for the other two chemicals.

Table 4.3.1. Measured refractive indices and Sellmeier equations of acetonitrile, pentane, and hexane

n / λ (μm)	Acetonitrile	Pentane	Hexane
0.45	1.349	1.3642	--------
0.48	1.3474	1.3619	1.3804
0.50	1.3467	1.3614	1.3795
0.55	1.3442	1.3592	1.3772
0.58	1.3436	1.3578	1.3762
0.60	1.3426	1.3571	1.3749
0.65	1.3408	1.3561	1.3733
0.68	1.3406	1.356	1.373

Acetonitrile: $n = 1.32488\text{-}0.00171/\lambda^2 + 0.00283/\lambda^4$ (4.3.1)

Pentane: $n = 1.35079+0.00191/\lambda^2 + 0.00016/\lambda^4$ (4.3.2)

Hexane: $n = 1.37071\text{-}0.00137/\lambda^2 + 0.00102/\lambda^4$ (4.3.3)

Although the equations (4.3.2) and (4.3.3) for pentane and hexane are sufficiently precise only in the visible range, the dispersion of organic compounds varies only slowly in the infrared, so that we extrapolate them into the longer wavelength region with reasonable accuracy. This is certainly a first approximation to the problem. However, in order to be able to estimate the required fiber waist thicknesses and liquids, this method gives valid results. Comparing the exact refractive index of acetonitrile in the IR (the only component with a tabulated

refractive index in the IR) with the extrapolation, we found only small deviations in GVD (around 10 ps/nm/km). Also, the GVD zero point uncertainty is only in the range of 0.1 μm. Therefore, before more exact measurements of the IR indices of other liquids can be made, this method has to be sufficient. In the future, immersed tapered fibers can be characterized with respect to their GVD using white light interferometry.

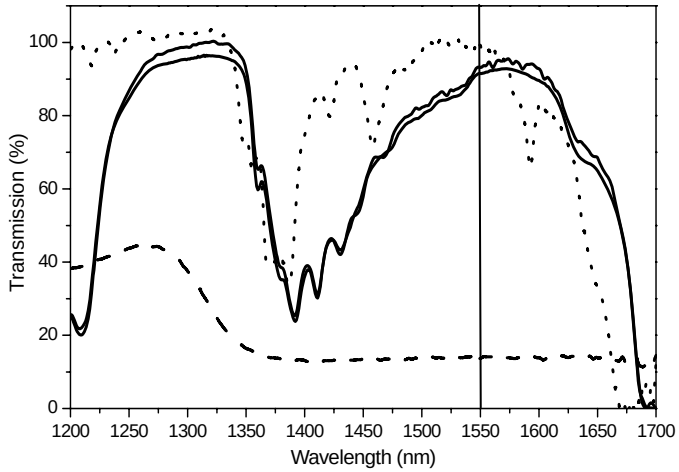

Fig. 4.3.2 The transmission curves of a 9.8 mm cuvette of water (dashed), acetonitrile (dotted), pentane and hexane (solid). The curves of pentane and hexane are almost on top of each other. I and my colleague Jörn Teipel measured the data using a CARY spectrophotometer in Prof. Buse's group.

In principle, water can also provide an appropriate refractive index (1.33 at 589 nm), and its Sellmeier equation with respect to wavelengths from 0.2 μm to 1.1 μm can be found in Ref. [86]. However, strong absorption takes place in the infrared due to the O-H bond vibration overtones, which excludes water for our application. The transmission curves of a 9.8 mm cuvette with water, acetonitrile, pentane, and hexane in the infrared region are shown in Fig. 4.3.2 (corrected for the cuvette reflection). Acetonitrile, pentane, and hexane do not suffer from near infrared absorption since they do not possess O-H vibrational overtone absorption lines. The absorption bands around 1400 nm are on the order of 1 cm^{-1} and do therefore influence the refractive index in that region only very slightly.

4.4 Group velocity dispersion of tapered fibers immersed in chemical liquids

Figure 4.4.1 shows the calculated GVD of tapered fibers with a diameter of 3 μm, assuming that the fibers are immersed in (a) acetonitrile, (b) pentane, and (c) hexane, respectively.

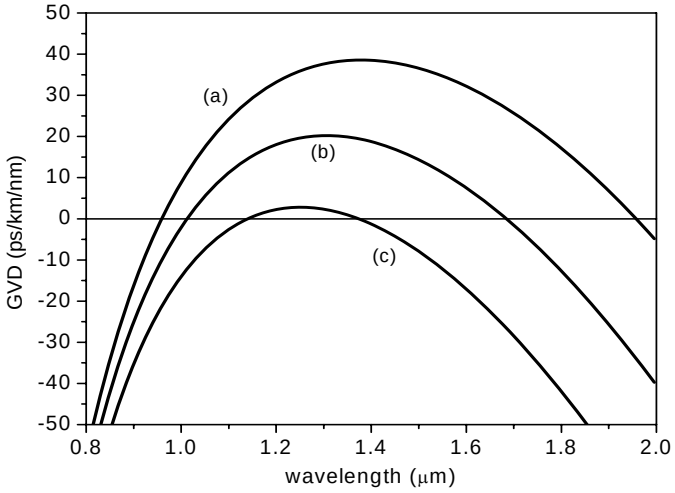

Fig. 4.4.1. The GVD curve of tapered fiber with diameter 3 μm when it is immersed in (a) acetonitrile (b) pentane (c) hexane.

The curves in Fig. 4.4.1 reveal that a tapered fiber with a diameter of 3 μm possesses favorable GVD properties in the anomalous dispersion region if immersed into these three chemicals. The first zero dispersion point appears around 1 μm in the near infrared. The GVD curve has quite small values (<40 ps/km/nm) over the span between the two zero-dispersion points. The bandwidth of anomalous dispersion of the tapered fiber in acetonitrile (950 nm~1650 nm) is broader than that of the tapered fiber in pentane and hexane, while smaller GVD values (less than 20 ps/nm/km) can be achieved using pentane and hexane. We can further conclude that using acetonitrile, pentane, or hexane as the environment of a tapered fiber, a supercontinuum generation should be feasible in the infrared and the corresponding spectral width should be significantly enlarged. Depending on the exact length of the waist, the continuum might stretch even further into the infrared, as the absorption values around

Harbold *et al.* reported continuum spectrum generation around the second dispersion zero point (1.26 μm) of a tapered fiber in air with a diameter of 1 μm [4]. In our case, supercontinua should be feasible at even longer wavelengths in the infrared, e.g., around 1.6 μm when using pentane and a fiber diameter around 3 μm.

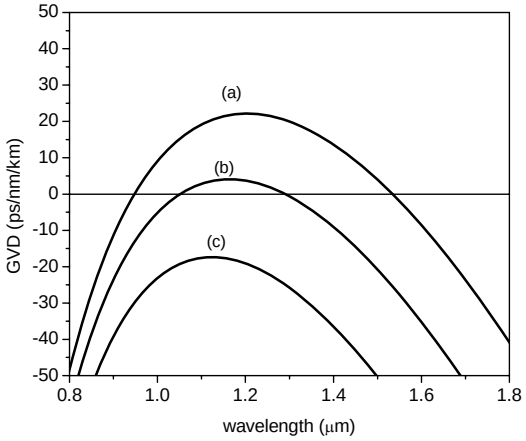

Fig. 4.4.2 The GVD curve of tapered fiber with diameter 2.5 μm when it is immersed in (a) acetonitrile (b) pentane (c) hexane.

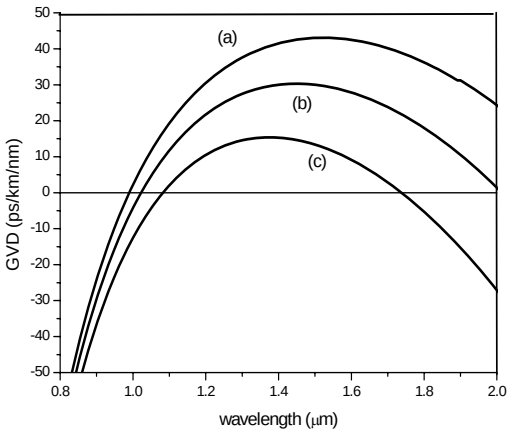

Fig. 4.4.3 The GVD curve of tapered fiber with diameter 3.5 μm when it is immersed in (a) acetonitrile (b) pentane (c) hexane.

Regarding tapered fibers with diameters of 2.5 μm and 3.5 μm, GVD curves are shown in Fig. 4.4.2 and Fig. 4.4.3, respectively. With smaller diameter, the tapered fiber provides lower and steeper group velocity dispersion, and the fiber immersed in hexane does not reach the anomalous dispersion region. With a larger diameter of 3.5 μm, the anomalous dispersion region covers more wavelengths. The first zero-dispersion wavelength (ZDW) appears in a lower position while all the second ZDWs of the three candidates occur beyond 1.7 μm.

4.5 Optimization of the group velocity dispersion curve

4.5.1 Mixing of different chemicals

In some cases, the center frequency of the pump cannot exactly match the ZDW of the GVD curve, which results in lower intensity and narrower spectra of the supercontinuum light. Therefore, we mix different chemicals to get a new effective refractive index. This allows the optimal ZDW to be generated just at the frequency of the pump pulse by changing the ratio of the chemical constituents. For a pump pulse at 1.55 μm, the second ZDW can occur exactly around 1.55 μm when a tapered fiber with a diameter of 3 μm is surrounded by pentane and hexane mixed in a ratio of 1:1, as shown in Fig. 4.5.1. The curve in Fig. 4.5.2 shows the variation of the second ZDW position with the change of the ratio between pentane and hexane. A tuning range from 1.38 μm to 1.7 μm for the second ZDW can easily be achieved by varying the mixing ratio.

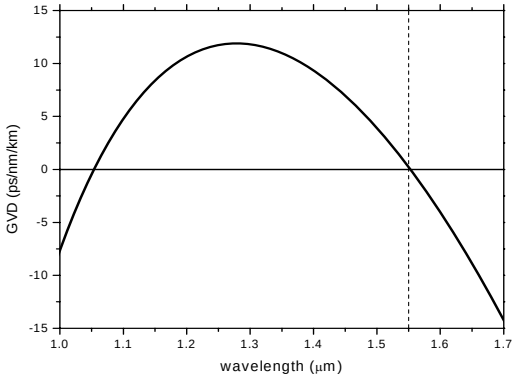

Fig. 4.5.1. The GVD curve of a tapered fiber with a diameter 3 μm when it is immersed in the mixture of pentane and hexane (1:1).

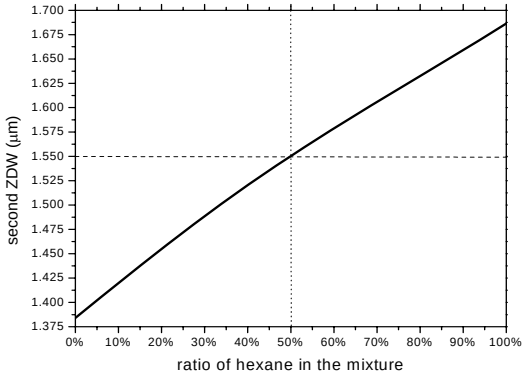

Fig. 4.5.2. The second zero-dispersion wavelength position versus the ratio of hexane in the mixture (hexane and pentane) when the fiber taper diameter is 3 μm.

4.5.2 Selection of the fiber material

The diameter of tapered fibers is one of the significant factors which influence the nonlinear effects in the fiber. However, because of the limited range of the refractive indices that the chemicals can offer, the diameter of the tapered fiber cannot be smaller than 3 μm in order to achieve an anomalous dispersion range. For the first ZDW of GVD curve, no matter what liquid is employed and what diameter of the fiber taper is used, the first ZDW cannot be generated in the telecommunication window. Therefore, we would like to select some alternative fiber materials (BK7, SF6, and SF9) instead of quartz to serve as optical fiber material [87] which could overcome such disadvantages.

For the calculations of the GVD, the necessary formulas for the three selected glasses, such as the Sellmeier equations, are given in Ref. [88], and their basic optical properties are shown in Table 4.5.1 [89]. The GVD curves of a tapered fiber made of BK7 show the desired anomalous dispersion properties when the fiber taper with a diameter of 2 μm is immersed in acetonitrile, pentane, and hexane, respectively (see Fig. 4.5.3). Figure 4.5.4 shows the GVD curves generated by tapered fibers made out of SF6 and SF59, immersed in chlorobenzene (refractive index 1.525 at 589 nm). Their first ZDW can occur in the telecommunication window and their GVD characteristics are rather flat. The advantage of such high-index glasses is to allow a much greater range of immersion liquids with refractive indices that are smaller than the glass index.

Table 4.5.1. The optical properties of glasses BK7, SF6, and SF59 (1 esu = 174 cm^2/W)

	Refractive index at 1550 nm	Transmission range (nm)	Nonlinear index n_2 (10^{-13} e.s.u)
Fused silica	1.444	185-2000	1.1
BK7	1.4946	450-1600	1.15
SF6	1.7644	500-2000	9.90
SF59	1.8960	500-2000	19.2

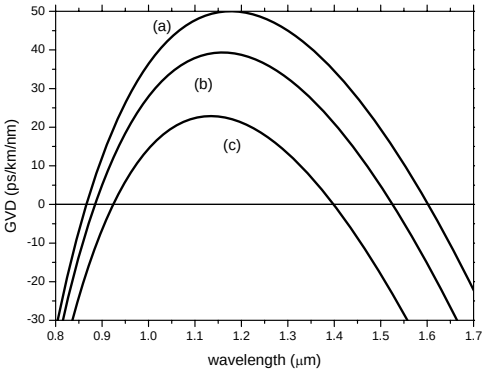

Fig. 4.5.3. The GVD curve of a BK7 tapered fiber with diameter 2 μm when it is immersed in (a) acetonitrile, (b) pentane, (c) hexane.

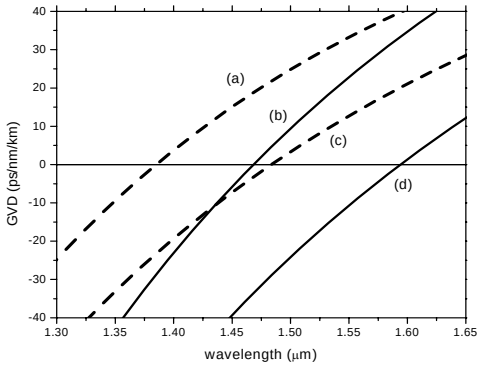

Fig. 4.5.4. The GVD curve of a tapered fiber immersed in chlorobenzene, with a fiber taper material of (a) SF6, d=3 μm (b) SF59, d=3 μm (c) SF6, d=4 μm (d) SF59, d=4 μm.

4.6 Theoretical simulations of supercontinuum in liquid cladding tapered fibers

The optical properties of the liquids acetonitrile, pentane, and hexane, were discussed in the previous sections. Tapered fibers immersed in those liquid present favorable GVD curves and can be used to generate supercontinuum in the telecommunication window. However, those liquids show strong absorption at wavelengths larger than 1700 nm, which will limit the supercontinuum generation in the mid-infrared region. Therefore, in this section we will introduce a new liquid to immerse the tapered fiber and simulate the supercontinuum generation. Compared with acetonitrile, pentane, and hexane, this liquid (Series AAA), offered by the Cargille company, displays perfect transmission properties. It is transparent from 500 nm to more than 2000 nm. The details about this liquid are shown in appendix [90].

Figure 4.6.1 shows the group velocity dispersion curves of a tapered fiber immersed in liquid Series AAA with fiber diameters of 2.2 μm (blue), 2.7 μm (red), and 3.2 μm (black). It demonstrates that with the liquid of Series AAA, the fiber has two zero dispersion wavelengths in the infrared region, and the GVD curves in the anomalous dispersion regime varies extremely slowly. Those properties make this fiber very suitable to generate a smooth and dramatically broadened spectrum in the near- and mid-IR.

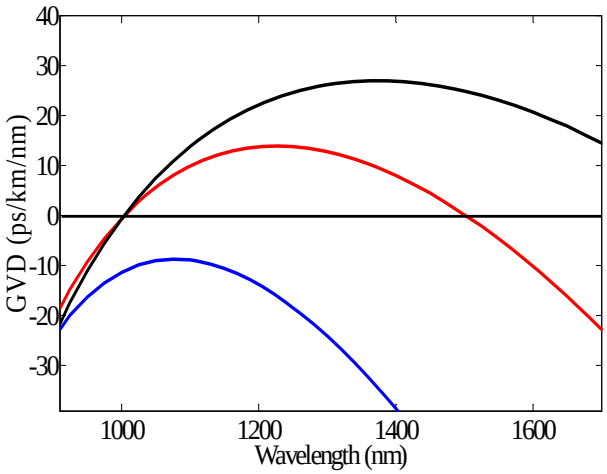

Fig. 4.6.1 The group velocity dispersion curves of a tapered fiber immersed in liquid Series AAA with fiber diameters of 2.2 μm (blue), 2.7 μm (red), and 3.2 μm (black).

To simulate the supercontinuum generation, we applied the nonlinear Schrödinger equation as:

$$\frac{\partial A(z,T)}{\partial z}=\sum_{k=2}\frac{i^{k+1}}{k!}\beta_k\cdot\frac{\partial^k A(z,T)}{\partial T^k}+i\gamma\left(1+\frac{i}{\omega_0}\frac{\partial}{\partial T}\right)\left(A(z,T)\int_{-\infty}^{\infty}R(t')\left|A(z,T-t')\right|^2dt'\right).$$

(4.6.1)

In the simulation, we used the parameters with the fiber diameter of 2.7 μm, a fiber length of 90 mm, a pump wavelength of 1200 nm, soliton number *N* of 5, and a pulse duration of 50 fs. Figure 4.6.2 shows the initial stage of the supercontinuum generation and the phase matching condition. We find two dispersive waves in the visible and infrared region, and the wavelengths of these two waves can be well predicted by the phase matching condition. The generation mechanisms are described in detail in section 2.6. Figure 4.6.3 shows the final spectrum of the SC generation. The spectrum ranges from 700 nm to 2000 nm.

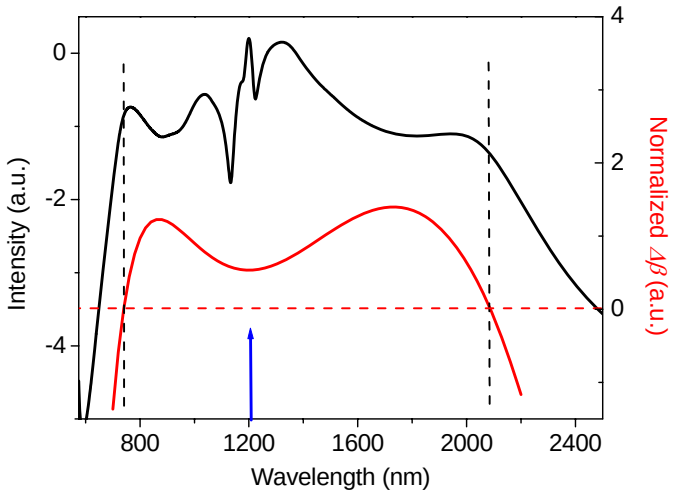

Fig. 4.6.2 The spectrum of initial stage of the supercontinuum generation (black) and the phase matching condition (red). The fiber has a diameter of 2.7 μm and a length of 90 mm. It is pumped at 1200 nm with a pulse duration of 50 fs and soliton number *N* of 5.

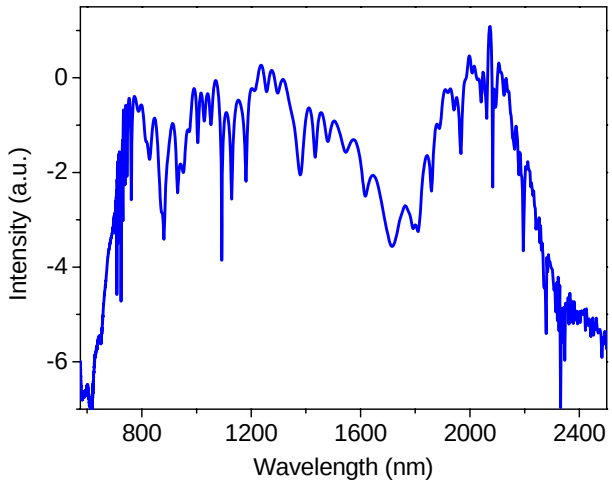

Fig. 4.6.3 The simulated supercontinuum spectrum after the immersed tapered fiber as described in Fig. (4.6.2)

Section 5 Polarization-maintaining tapered fibers [122]

5.1 Introduction

Tapered optical fibers and photonic crystal fibers, where supercontinuum (SC) generation takes place, have a large number of applications in pulse compression, parametric amplifiers, supercontinuum-based WDM telecom sources, etc. [91-93]. Applications of SC radiation in CARS microscopy, OPO systems, and sensors have been proposed, but the group delay variations of conventional tapered fibers or photonic crystal fibers pose challenges with those applications that have not yet been overcome.

For many applications it is desirable to have SC radiation with a high degree of polarization. Besides being interesting in its own right, polarization maintaining SC generation should also be more efficient since the power that is contained in a certain polarization state is relevant for the nonlinear processes that drive the SC generation. Recently, polarization maintaining photonic crystal fibers were fabricated and used to generate supercontinua [94-97], however, tapered fibers with polarization maintaining characteristics have not yet been realized. A polarization maintaining tapered fiber can find applications in many fields, such as gas sensors, atom trapping, *etc.* In this paper, we designed a tapered fiber with elliptical cross section in the waist region. As we will show, this fiber exhibits strong enough birefringence to maintain an incident linear polarization state throughout the propagation path and to generate a highly polarized supercontinuum.

Figure 5.1.1 shows the cross section and refractive index distribution of the untapered fiber in our design, being a confocal elliptical fiber. The odd and even dominant modes propagate in the core, with the transverse electric field along the semimajor and semiminor axis, respectively, as shown in Fig. 5.1.2. For small perturbations, the untapered fiber is singly polarized because of the high birefringence induced by the elliptical shape of the core.

In order to preserve polarization in the tapered fiber, the taper transition region should be adiabatic [24] [78], so that the perturbation caused by the variation of the fiber radius is small enough to couple negligible power from the odd dominant mode to the even mode. The criterion derived from this physical argument is that the beat length L_b should be smaller than the mechanical perturbation periods L_p everywhere

along the taper, where $L_b = \dfrac{2\pi}{\beta_{odd} - \beta_{even}}$, β_{odd} and β_{even} are the propagation constants of the odd dominant mode and even dominant mode, respectively; $L_p = \dfrac{\rho(z)}{\tan^{-1}\left|d\rho(z)/dz\right|}$, z is the distance along the taper, and $\rho(z)$ is the local core radius. In this paper, we assume that the taper transition regions are approximately adiabatic.

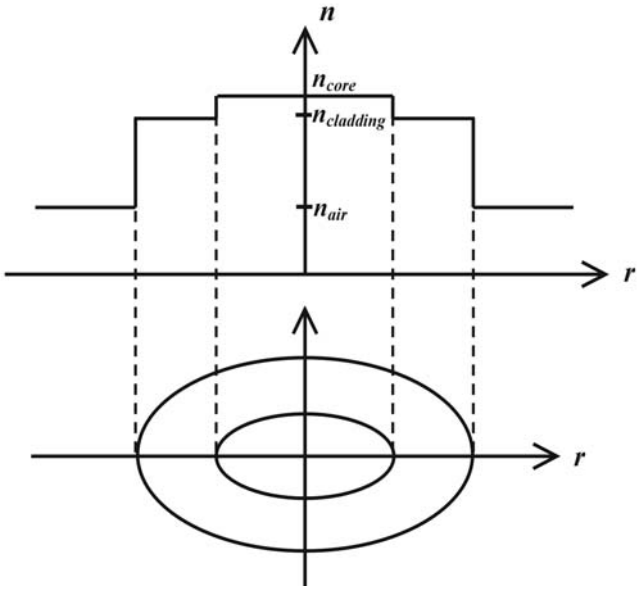

Fig.1. The confocal elliptical cross section and refractive index distribution of the untapered fiber.

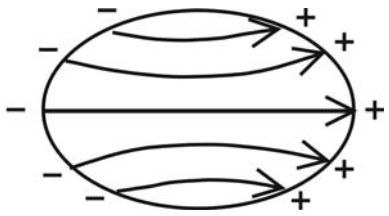

(a) *o*HE$_{11}$ mode

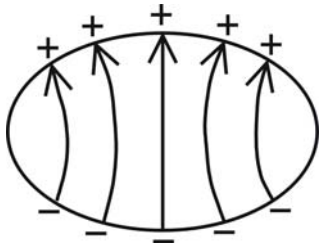

(b) *e*HE$_{11}$ mode

Fig.2. Transverse electric field of the two dominant modes (a) *o*HE$_{11}$ and (b) *e*HE$_{11}$.

5.2 Birefringence calculation of the tapered fiber in the waist region

The structural birefringence of the fiber is defined as

$$\Delta n = \frac{\lambda}{2\pi} \cdot (\beta_{odd} - \beta_{even}) \cdot \tag{5.2.1}$$

Propagation constants β_{odd} and β_{even} can be characterized theoretically by solving the propagation equation in elliptical coordinates, as shown in Fig. 5.2.1. The radial coordinate η describes a set of confocal ellipses, and the azimuthal coordinate ξ a set of hyperbolae orthogonal to the ellipses. The axial coordinate in the direction of propagation is *z*. The eccentricity of the ellipse is $e = \sqrt{1 - b^2/a^2}$, the focal distance is $q = \sqrt{a^2 - b^2}$, and the other parameters are defined in Fig. 5.2.1.

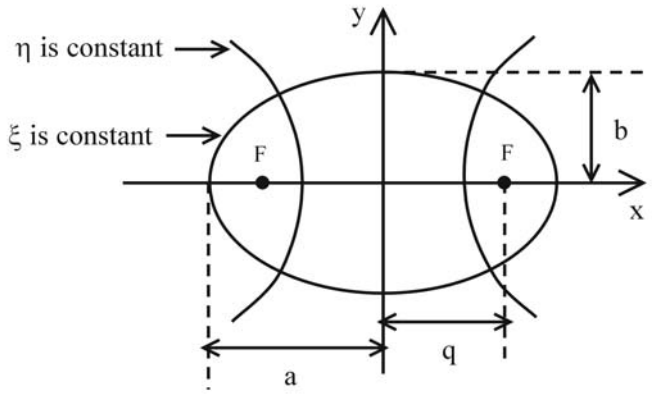

Fig. 5.2.1 Elliptical coordinate, where *a* is the semimajor axis and *b* is the semiminor axis, *q* is focal distance, and *F* is the focus of the ellipse.

Yeh and others have analyzed elliptical-core waveguides and approximately calculated the propagation constant of a weakly guided elliptical fiber based on Mathieu functions [98-100]. However, the approximation made in their simulation could be applied only to the modes at small eccentricities and small differences in the effective indices between core and cladding, which does not hold true in our tapered fibers. Furthermore, the calculation of GVD requires values of the propagation constant with very high precision. Therefore, in this paper we evaluate the propagation constants β_{odd} and β_{even} with the full vector equations and consideration of higher-order Mathieu functions. Thus we can overcome the limitations of the weakly guiding and small eccentricity approximation above.

5.2.1 Calculation of propagation constants of the odd and even dominant modes

The longitudinal components can be expanded in terms of Mathieu functions as:

$$\begin{pmatrix} E_{z1} \\ H_{z1} \end{pmatrix} = \begin{pmatrix} \sum_{m=0}^{\infty} A_m \, Ce_m(\xi, q1)\, ce_m(\eta, q1) \\ \sum_{m=1}^{\infty} B_m \, Se_m(\xi, q1)\, se_m(\eta, q1) \end{pmatrix}, \tag{5.2.2}$$

in the core, and

$$\begin{pmatrix} E_{z2} \\ H_{z2} \end{pmatrix} = \begin{pmatrix} \sum_{m=0}^{\infty} C_m \, Fek_m(\xi, q2)\, ce_m(\eta, q2) \\ \sum_{m=1}^{\infty} D_m \, Gek_m(\xi, q2)\, se_m(\eta, q2) \end{pmatrix}, \tag{5.2.3}$$

in the cladding,

where E_{z1} and H_{z1} are the longitudinal components of the electric and the magnetic field in the core, respectively. A_m, B_m, C_m, and D_m are constants, q_1 and q_2 satisfy $q_1 = n_1^2 k_0^2 - \beta^2$ and $q_2 = n_2^2 k_0^2 - \beta^2$, respectively, $k_0 = 2\pi/\lambda_0$ is the wave number, n_{core} is the refractive index of the core, and β is the propagation constant. ce_m and se_m are the even and odd Mathieu functions of the first kind, Ce_m and Se_m are the even and odd modified Mathieu functions of the first kind, and Fek_m and Gek_m are the even and odd modified Mathieu functions of the second kind.

The remaining transverse components of the electrical and magnetic field can be found from the longitudinal components using Maxwell's equations

The Mathieu functions and their derivatives can be expressed in the following way [101]:

$$ce_m(\eta, q_2) = \sum_{n=0}^{\infty} \alpha_{m,n}(q_2, q_1) ce_n(\eta, q_1), \quad se_m(\eta, q_2) = \sum_{n=1}^{\infty} \beta_{m,n}(q_2, q_1) se_n(\eta, q_1),$$

$$\frac{d}{d\eta} ce_m(\eta, q2) = \sum_{n=1}^{\infty} \chi_{m,n}(q_2) se_n(\eta, q_2), \quad \frac{d}{d\eta} se_m(\eta, q2) = \sum_{n=0}^{\infty} \nu_{m,n}(q_2) ce_n(\eta, q_2), \tag{5.2.4}$$

where, $\alpha_{m,n}(q_2, q_1)$, $\beta_{m,n}(q_2, q_1)$, $\chi_{m,n}(q_2)$, and $\nu_{m,n}(q_2)$ are connection coefficients, which satisfy the equations:

$$\alpha_{m,n}(q_2,q_1)=\frac{\int_0^{2\pi} ce_m(\eta,q_2)ce_n(\eta,q_1)d\eta}{\int_0^{2\pi} ce_n^2(\eta,q_1)d\eta},\qquad \beta_{m,n}(q_2,q_1)=\frac{\int_0^{2\pi} se_m(\eta,q_2)se_n(\eta,q_1)d\eta}{\int_0^{2\pi} se_n^2(\eta,q_1)d\eta},$$

$$\chi_{m,n}(q_2)=\frac{\int_0^{2\pi} ce'_m(\eta,q_2)se_n(\eta,q_2)d\eta}{\int_0^{2\pi} se_n^2(\eta,q_2)d\eta},\qquad \nu_{m,n}(q_2)=\frac{\int_0^{2\pi} se'_m(\eta,q_2)ce_n(\eta,q_2)d\eta}{\int_0^{2\pi} ce_n^2(\eta,q_2)d\eta},\tag{5.2.5}$$

According to the orthogonality of Mathieu functions and the properties of the Fourier coefficients $A_n(m,q)$ and $B_n(m,q)$ [101], the connection coefficients can be expressed as:

(a) If *m* and *n* are both even,

$$\alpha_{m,n}(q_2,q_1)=A_0(m,q_2)\cdot A_0(n,q_1)+\sum_{i=0}^{\infty}A_{2i}(m,q_2)\cdot A_{2i}(n,q_1);$$

$$\beta_{m,n}(q_2,q_1)=\sum_{i=1}^{\infty}B_{2i}(m,q_2)\cdot B_{2i}(n,q_1);$$

$$\chi_{m,n}(q_2)=\sum_{i=1}^{\infty}(-2)\cdot i\cdot A_{2i}(m,q_2)\cdot B_{2i}(n,q_2);$$

$$\nu_{m,n}(q_2)=\sum_{i=1}^{\infty}2\cdot i\cdot A_{2i}(n,q_2)\cdot B_{2i}(m,q_2)\tag{5.2.6}$$

(b) If *m* and *n* are both odd,

$$\alpha_{m,n}(q_2,q_1)=\sum_{i=0}^{\infty}A_{2i+1}(m,q_2)\cdot A_{2i+1}(n,q_1)\ ,$$

$$\beta_{m,n}(q_2,q_1)=\sum_{i=0}^{\infty}B_{2i+1}(m,q_2)\cdot B_{2i+1}(n,q_1),$$

$$\chi_{m,n}(q_2)=\sum_{i=0}^{\infty}(-2\cdot i-1)\cdot A_{2i+1}(m,q_2)\cdot B_{2i+1}(n,q_2)\ ,$$

$$\nu_{m,n}(q_2)=\sum_{i=0}^{\infty}(2\cdot i+1)\cdot A_{2i+1}(n,q_2)\cdot B_{2i+1}(m,q_2),\tag{5.2.7}$$

where $A_n(m,q)$ and $B_n(m,q)$ are Fourier coefficients of the even and odd Mathieu functions, respectively. If m and n have unequal parity, all the connection coefficients are equal to zero.

Using the boundary conditions and the expansions of Eqs (5.2.2) and (5.2.3) above, we can build up a homogeneous infinite matrix equation with the expansion

coefficients (A_m, B_m, C_m, and D_m) as variables. In order to get a set of non-zero solutions for the variables, the determinant of this matrix should be zero. For the modes HE_{lp}, with the mode number l, the determinant starts with the matrix element whose m and n are equal to l. The propagation constant β can be obtained by finding the roots of the determinant numerically. We have found that sufficient accuracy is obtained by using maximum values of m and n of seven. Figure 5.2.2 shows the curve of the calculated propagation constants as a function of the wavelength in the tapered fiber with a semimajor axis a of 1.5 μm and a semiminor axis b of 0.75 μm.

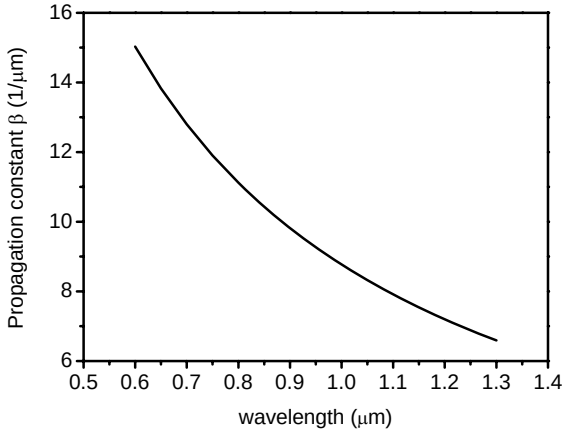

Fig. 5.2.2 Propagation constant for the odd dominant mode oHE_{11} as a function of wavelength with the semimajor axis of 1.5 μm and an eccentricity of 0.866.

The calculations of the longitudinal components of an even dominant mode are identical to those of the odd one, with the even Mathieu functions replaced by the odd ones and vice versa.

5.2.2 Birefringence of the tapered fiber in the waist region

According to Eq. (5.2.1), we evaluate the birefringence of the tapered fiber and plot the results in Fig. 5.2.3. The tapered fiber shows a large birefringence in the visible and near infrared region due to the large refractive index difference between the fiber and air, and the birefringence becomes larger with increasing wavelength. Compared with a highly birefringent PCF, which yields a beat length around 0.4 mm at 1540 nm [102], the tapered fiber with a semimajor axis of 1.5 μm and a semiminor axis of 0.75 μm shows a larger birefringence around Δn = 0.016 and a shorter beat length of 0.1 mm at 1540 nm. Figure 5.2.3 (a) shows the wavelength dependence of birefringence and beat length of tapered fibers with different eccentricities, and Fig. 5.2.3 (b) shows the birefringence and beat length with different semimajor axes. This demonstrates that the birefringence increases for larger eccentricity e or smaller focal distance q.

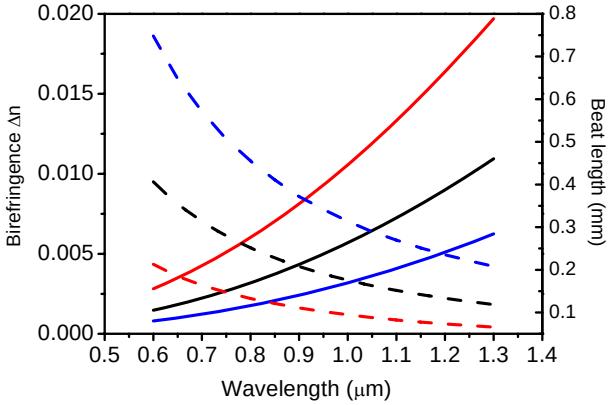

Fig. 5.2.3 (a). The calculated curves of birefringence Δn (solid) and beat length (dashed) as a function of wavelengths with different ratios between semiminor and semimajor axis of 0.6, 0.5, and 0.4 (from top to bottom). The semimajor axis *a* is 1.5 μm.

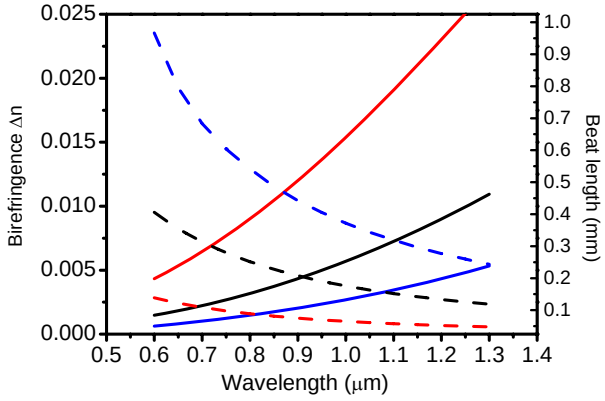

Fig. 5.2.3 (b). The calculated curves of birefringence (solid) and beat length (dashed) as a function of wavelength with different semimajor axes *a* of 1 μm, 1.5 μm, and 2 μm (from top to bottom). The eccentricity *e* is 0.866.

5.3 Group velocity dispersion and comparision between the two modes

5.3.1 Group velocity dispersion in waist region

The GVD of a tapered fiber is defined as the second derivative of the propagation constant β with respect to ω, $D = -\frac{2\pi c}{\lambda^2}\frac{d^2\beta}{d\omega^2}$. Figure 5.3.1 shows the GVD curves of the ${}_oHE_{11}$ mode as a function of wavelength for tapered e-core fibers made from fused silica SMF28 fibers, corresponding to different semimajor axes with an eccentricity of 0.866.

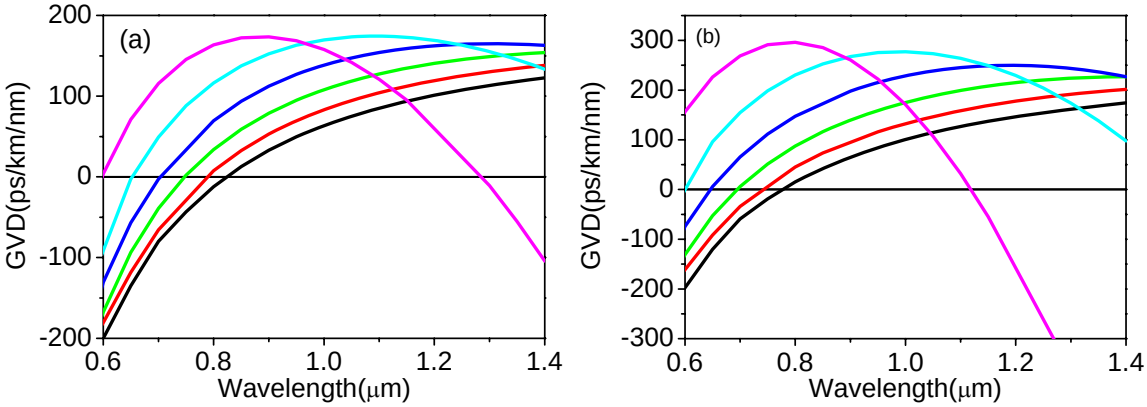

Fig. 5.3.1 The calculated GVD curve of ${}_oHE_{11}$ mode (a) and ${}_eHE_{11}$ mode (b) with semimajor axes of 1.5 μm, 2.0 μm, 2.5 μm, 3.0 μm, 3.5 μm, and 4 μm (from top to bottom).

5.3.2 Comparision between the two modes

With the same fiber parameters, the zero GVD of the odd mode occurs at a larger wavelength than that of the even mode. This fact can be understood by considering the polarization direction of the two modes. The odd mode has the transverse electric field along the semimajor axis, which corresponds to the fundamental mode of a circular cross-section fiber with a larger diameter. The even mode has the electrical field along the semiminor axis, which corresponds to the fundamental mode of a circular fiber with a smaller diameter. The zero dispersion wavelength in a circular fiber moves towards the infrared region with increasing diameter, therefore, the odd mode has the zero GVD at a larger wavelength. The relationship of the zero dispersion wavelengths of the different modes is shown in Fig. 5.3.2.

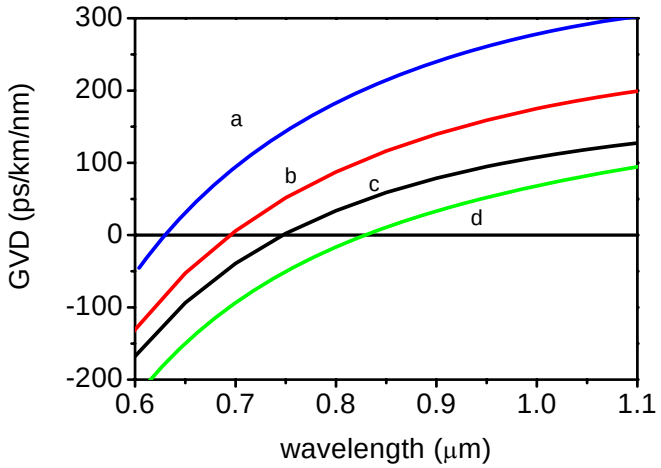

Fig. 5.3.2 The GVD curves as a function of wavelength for different modes: (a) fundamental mode in circular waveguide with a radius of 0.75 μm, (b) odd dominant mode with semimajor axis of 1.5 μm and semiminor axis of 0.75 μm, (c) even dominant mode with semimajor axis of 1.5 μm and semiminior axis of 0.75 μm, and (d) fundamental mode in a circular waveguide with a radius of 1.5 μm.

Fig. 5.3.2 also demonstrates that the zero dispersion wavelength of the fiber can be slightly changed by launching the incident light with different polarization states. With the polarization state parallel to the semimajor axis, the zero dispersion wavelength is at 750 nm, and with the polarization parallel to the semiminor axis, the zero dispersion wavelength is at 700 nm. This will impact the subsequent supercontinuum generation characteristics.

5.4 Theoretical simulations of supercontinuum generation in polarization-maintaining tapered fibers

In our numerical model to simulate the pulse propagation in a PM tapered fiber, we consider the fiber as a weakly guiding one, which can be described by a generalized scalar propagation equation:

$$\frac{\partial A}{\partial z} - i \cdot \sum_{k \geq 2} \frac{i^2 \beta_k}{k!} \cdot \frac{\partial^2 A}{\partial t^k} = i\gamma \left(1 + \frac{i}{\omega_0} \frac{\partial}{\partial t}\right) \cdot \left(A \cdot \int_{-\infty}^{t} R(t') \left| A(z, t-t') \right|^2 dt' \right), \qquad (5.4.1)$$

where $A = A(z,t)$ is envelope of the electric field, β_k is the k^{th} order dispersion coefficient at center frequency ω_0, $R(t)$ is the response function of fused silica and γ is the nonlinear parameter. All the parameters in the propagation equation can be evaluated in a similar way as in the cases of circular tapered fibers, except the nonlinear parameter γ, which is expressed as:

$$\gamma = \frac{n_2 \omega_0 \int\int_{-\infty}^{\infty} \left| F(x,y) \right|^4 dxdy}{c \left(\int\int_{-\infty}^{\infty} \left| F(x,y) \right|^2 dxdy \right)^2}. \qquad (5.4.2)$$

n_2 represents the nonlinear refractive index of fused silica, c is the light speed in vacuum, and $F(x,y)$ is the solution of

$$\frac{1}{q^2 \left[\cosh^2(\xi) - \cos^2(\eta) \right]} \left[\frac{\partial^2 F(\xi,\eta)}{\partial \xi^2} + \frac{\partial^2 F(\xi,\eta)}{\partial \eta^2} \right] + \left(n^2 k_0^2 - \beta^2 \right) F(\xi,\eta) = 0, \quad (5.4.3)$$

where ξ and η satisfy the relations

$$\cosh(\xi)\cos(\eta) = x/q, \qquad (5.4.4)$$

and

$$\sinh(\xi)\sin(\eta) = y/q. \qquad (5.4.5)$$

We used an approximated expression of mode distribution $F(x,y)$ for the fundamental mode in the elliptical core [224]

$$F(\xi,\eta) \cong A_0 Ce_0(\xi, q_1) ce_0(\eta, q_1), \qquad (5.4.6)$$

which was substituted to Eq. (9) to evaluate the value of nonlinear parameter γ.

The polarization maintaining tapered fiber used in our simulation has semimajor axis a and semiminor axis b of 1.5 μm and 0.75 μm, respectively, and a fiber waist length of 0.9 mm. The dispersion coefficients for the fundamental mode (odd mode) used in the simulation are calculated up to the seventh order. At the pump

wavelength of 830 nm, the nonlinear parameter γ is 0.116 /m/W, and the dispersion coefficients are:

$\beta_2 = -1.796\times10^{-2}\ ps^2/m$, $\beta_3 = 8.094\times10^{-5}\ ps^3/m$, $\beta_4 = -8.502\times10^{-8}\ ps^4/m$,

$\beta_5 = 1.477\times10^{-10}\ ps^5/m$, $\beta_6 = -1.943\times10^{-13}\ ps^6/m$, and $\beta_7 = -7.711\times10^{-16}\ ps^7/m$.

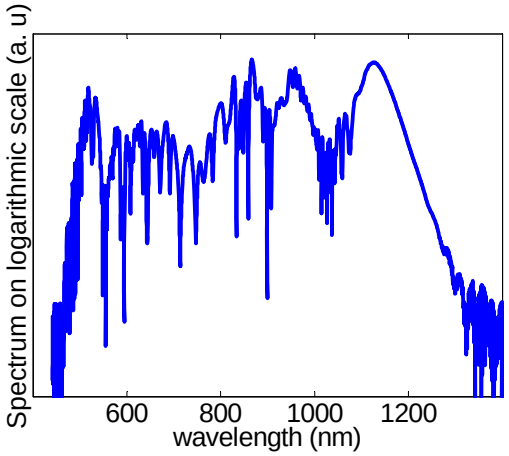

Fig. 5.4.1 The simulated spectrum of SC generation in a polarization maintaining fiber with semimajor of 1.5 μm and semiminor of 0.75 μm. The pump wavelength is 830 nm, the peak power is 5000 W, and the pulse duration is 80 fs.

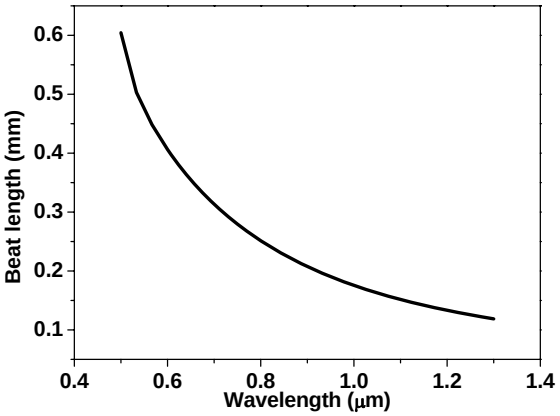

Fig. 5.4.2 The calculated curves of beat length as a function of wavelengths with semimajor of 1.5 μm and semiminor of 0.75 μm..

Figure 5.4.1 illustrates the spectral properties of the supercontinuum in a polarization maintaining tapered fibers with a pump wavelength of 830 nm, a peak power of 5000 W, and a pump pulse duration of 80 fs. The spectrum shows similar properties as that were generated in circular fibers. The wavelengths covered in the supercontinuum ranges from 500 nm to 1200 nm. To check whether the output pulse is singly polarized, we applied a coupled theory, which demonstrates that negligible coupling between two existing modes occurs if the perturbation length is much larger than the beat length of the two modes. The perturbation length in tapered fibers achieved through normal bending is more than 2 mm [3], whereas all the frequency components in the supercontinuum, as shown in Fig. (5.4.2), have beat lengths smaller than 0.6 mm. This demonstrates that our tapered fiber maintains a linear polarization state throughout propagation and generates a singly polarized supercontinuum.

We also calculated the spectral and temporal properties of an elliptical-core tapered fiber with the input polarization state not aligned along one of the birefringence axes. The fiber used in the simulation has the same parameters as that in Fig. 5.4.1, and the light launched to the fiber has an input peak power of 10 kW, a pumping wavelength of 710 nm, and a polarization state of 45^0 with respect to the

semimajor axis. To simulate the generated supercontinuum spectrum, one should consider the coupled nonlinear Schrödinger equations:

$$\begin{aligned}
&\frac{\partial A_o(z,T)}{\partial z}-\sum_{k=2}\frac{i^{k+1}}{k!}\beta_k^o\cdot\frac{\partial^k A_o(z,T)}{\partial T^k}\\
&=i\gamma_o\left(1+\frac{i}{\omega_0}\frac{\partial}{\partial T}\right)\cdot A_o(z,T)\\
&\quad\times\left\{f_R\int_{-\infty}^{\infty}h_R(t')\left(\left|A_o(z,T-t')\right|^2+\left|A_e(z,T-t')\right|^2\right)dt'+(1-f_R)\left(\left|A_o(z,T)\right|^2+\frac{2}{3}\left|A_e(z,T)\right|^2\right)\right\}\\
&\frac{\partial A_e(z,T)}{\partial z}-\left(\beta_1^o-\beta_1^e\right)\cdot\frac{\partial A_e(z,T)}{\partial T}-\sum_{k=2}\frac{i^{k+1}}{k!}\beta_k^e\cdot\frac{\partial^k A_e(z,T)}{\partial T^k}\\
&=i\gamma_e\left(1+\frac{i}{\omega_0}\frac{\partial}{\partial T}\right)\cdot A_e(z,T)\\
&\quad\times\left\{f_R\int_{-\infty}^{\infty}h_R(t')\left(\left|A_o(z,T-t')\right|^2+\left|A_e(z,T-t')\right|^2\right)dt'+(1-f_R)\left(\left|A_e(z,T)\right|^2+\frac{2}{3}\left|A_o(z,T)\right|^2\right)\right\},
\end{aligned}\tag{5.4.7}$$

where $A_o(z,T)$ and $A_e(z,T)$ represent the electric fields of the odd mode and even mode, respectively, a reference frame travelling with the odd mode is used, β_k^o and β_k^e are the dispersion coefficients at the center frequency of the pump and signal, respectively, $\beta_1^o-\beta_1^e$ is related to the group-velocity mismatch between the two incident pulses, and the nonlinear parameters of the odd mode γ_o and even mode γ_e are assumed equally. In the coupled NLSEs, we have neglected the term corresponding to four-wave mixing, because in a high birefringence fiber the term changes its sign quite often and its contribution averages out to zero [146].

Figure 5.4.3 and Fig. 5.4.4 shows the spectral and temporal properties of generated supercontinuum of the even mode (a) and odd mode (b), respectively. The figures demonstrate that both in the odd mode and in even mode we generated a supercontinuum. In fact, referring to the GVD curve shown in Fig. 5.3.2, we know the odd mode is pumped in the normal dispersion region, however, due to the strong self-phase modulation and cross-phase modulation, some generated frequency components extend to the anomalous dispersion region and form the Raman soliton, which is identified by the peak locating around –1 ps in Fig. 5.4.4 (b). However, lack of the soliton splitting process, no dispersive wave is found in the visible region as shown in Fig. 5.4.3 (b). Due to the group velocity mismatch, the odd mode and even mode separate from each other in time domain and the odd mode travels faster than the even

mode. The two modes have polarization states orthogonal to each other, and no energy transfer occurs between them. In other words, the odd mode generates a singly polarized supercontinuum radiation with a polarization state along the semimajor axis, and the even mode generates supercontinuum radiation with a single polarization state along the semiminor axis.

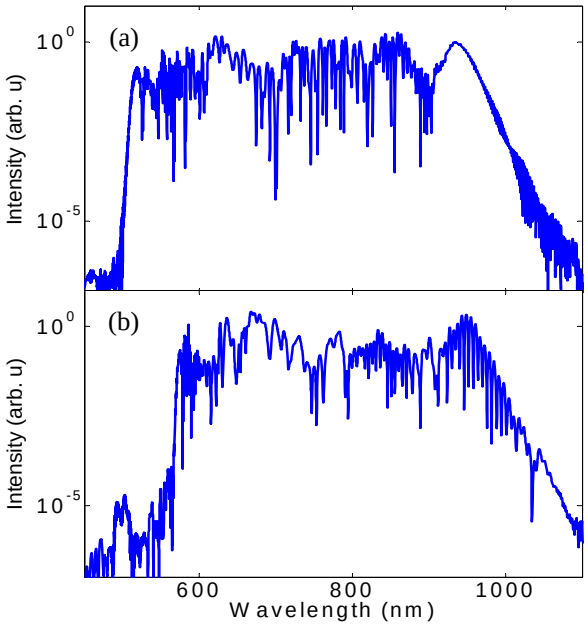

Fig. 5.4.3 The spectral properties of supercontinuum generation of (a) the even mode and (b) odd mode, respectively.

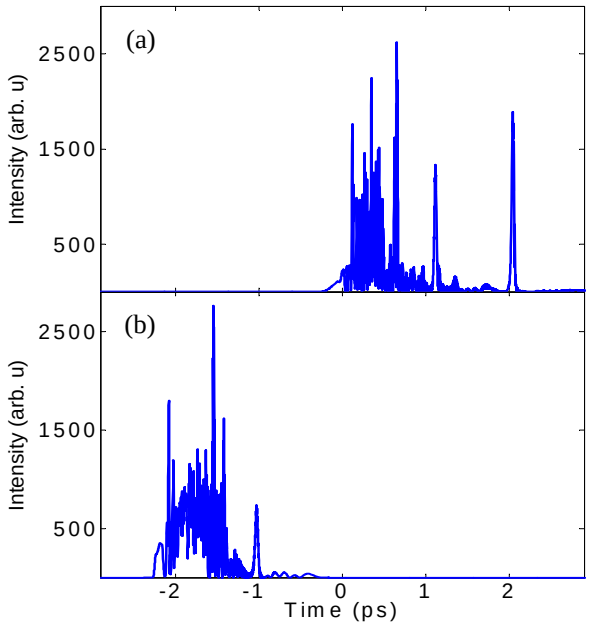

Fig. 5.4.4 The temporal properties of supercontinuum generation of (a) the even mode and (b) odd mode, respectively.

5.5 Fabrication

It is difficult to maintain the elliptical preform shape during the fabrication process of a tapered fiber, as the strong surface tension can deform the noncircular cross-section to a circular one. Therefore, the ratio between viscosity and surface tension of the fiber should be taken into account, so that high viscosity and low surface tension can prevent the fiber from such deformation. During the fiber drawing process, the softened fiber should be forceably cooled down before surface tension can stress it into a circular fiber. The method and apparatus for making non-circular fibers are described in a patent by Huey *et al*. [104]. The fabrication of microstructured optical fibers with elliptical holes has been realized by N. A. Issa et al. [96], and the fibers in his experiment are composed of a polymer which possesses a high ratio between viscosity and surface tension.

Section 6 Supercontinuum generation in liquid-core photonic crystal fibers [123]

6.1 Introduction

In the former sections, we concentrated on the properties of tapered fibers. In this section, we will design a new highly nonlinear fiber using photonic crystal fibers to generate dramatically broadened supercontinuum radiation from 700 nm to more than 3000 nm. A photonic crystal fiber has a central region of fused silica core surrounded by lower index air holes, with a cross section as shown in Fig. 6.1.1. Photonic crystal fibers have many merits to generate supercontinua, such as a simpler way to design group velocity dispersion, practical methods to fabricate an endless fiber, and so on. In the experiment, a pulse is launched into the core of the fiber and white light will be generated at the output. The group velocity dispersion (GVD) can be designed by changing the core diameter, fiber material refractive index, air hole diameter, and hole pitch.

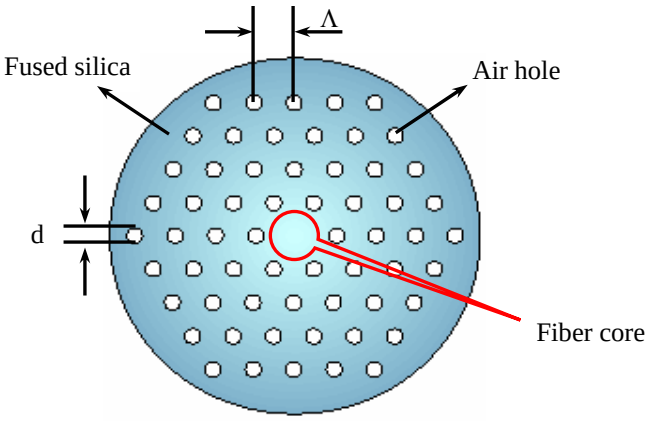

Fig. 6.1.1 The structure of photonic crystal fiber, where the blue areas represent fused silica, white areas represent air holes core, and the center area is the core of PCF. *d* is the air hole diameter and Λ is the hole pitch.

The supercontinuum generated by photonic crystal fibers, which normally ranges from 500 nm to 1200 nm, has many applications, such as pulse compression, parametric amplifiers, etc. However, in many cases a more broadened generation is needed, and therefore highly nonlinear fibers (with large nonlinear parameter γ) have long been sought after. At present, some methods were applied to enhance the nonlinear parameter of a fiber, such as reducing the diameter of fiber core, enlarging the air-filling fractions, and extruding the fiber preforms in soft lead-glass [105], *etc*.. However, there are some disadvantages of those methods. For example, if the

diameter of fiber core is reduced, it will be very difficult to couple the light into fiber and sometimes it will also result in optical damage of the fiber. Furthermore, with those methods, the spectrum can be broadened to be in the range from 500 nm to 2000 nm. No further broadening can be realized. In this section, we demonstrate a new way to realize a highly nonlinear fiber by filling the core of a hollow-core PCF with highly nonlinear liquids, such as carbon disulfide or nitrobenzene, as shown in Fig. 6.1.2. We name this kind of fiber a “liquid-core photonic crystal fiber” (LCPCF). The technique to fill the center hole of a holey fiber with liquids has been taken into practice, and the diameter of the liquid core can be reduced to a size as small as several microns [106,107].

Although highly nonlinear liquids such as carbon disulfide have been used to generate spectral broadening by filling the liquid in a hollow fiber [108,109], the resulting spectrum was not a supercontinuum. The non-continuous generation, which consists of only some distinct peaks, results from the fact that at the time of the experiment nearly two decades ago a crucial requirement to generate a supercontinuum was not fulfilled, namely that the GVD should be anomalous and close to zero at the pump wavelength. The liquid-core PCF designed in this paper on the other hand shows a zero GVD wavelength around 1.55 μm and an anomalous dispersion in the near infrared spectral region.

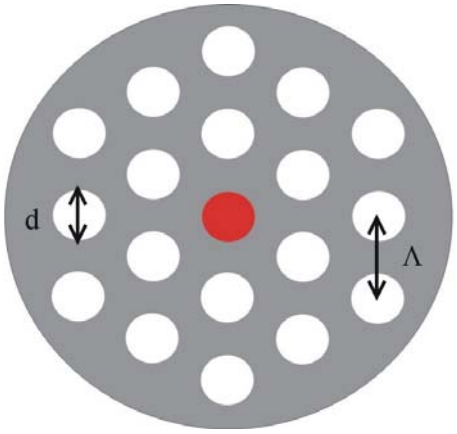

Fig. 6.1.2 The structure of the holey fiber, where the red center core is filled with liquids and the white holes are filled with air. *d* is the hole diameter and Λ is the hole pitch.

6.2 Physical properties of the high-nonlinearity liquids

6.2.1 Nonlinear coefficient

Nitrobenzene and carbon disulfide, as two candidates of the high-nonlinearity liquids, have nonlinear coefficients n_2 of $250\cdot10^{-13}\,esu$ and $120\cdot10^{-13}\,esu$ [110], which are more than 100 times and 50 times larger than that of silica, respectively.

6.2.2 Refractive index dispersion

The refractive index dispersion of carbon disulfide is given by [111]

$$n_{cs_2}(\lambda)=1.580826+1.52389\cdot10^{-2}/\lambda^2+4.8578\cdot10^{-4}/\lambda^4-8.2863\cdot10^{-5}/\lambda^6+1.4619\cdot10^{-5}/\lambda^8\,, \tag{6.2.1}$$

where λ is the wavelength of light in μm.

Unfortunately, no data in the visible and near infrared are available so far for nitrobenzene. Therefore, I and my colleague Jörn Teipel have measured the refractive indices of nitrobenzene with an Abbe refractometer, as shown in Fig. 6.2.1. Limited by the instrument, we were not able to perform the measurement at wavelengths larger than 1.1 μm.

From the measured data we extract the Sellmeier fit for the refractive index for nitrobenzene

$$n_{nitrobenzene}(\lambda)=1.5205+0.79\cdot10^{-2}/\lambda^2+1.670\cdot10^{-3}/\lambda^4-3.1\cdot10^{-4}/\lambda^6+3.0\cdot10^{-5}/\lambda^8 \quad (\lambda \text{ in } \mu\text{m}) \tag{6.2.2}$$

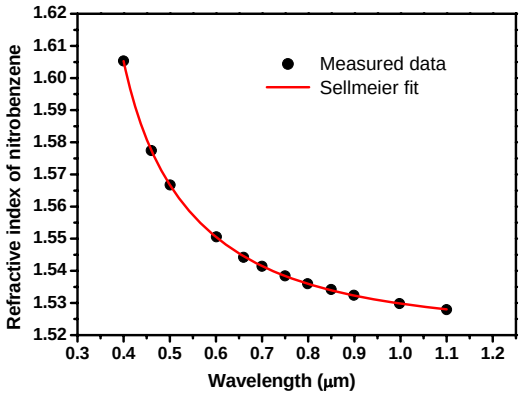

Fig. 6.2.1. The refractive index dispersion of nitrobenzene as a function of wavelengths. I and my colleague Jörn Teipel measured the data using an Abbe refractometer.

Although the equation for nitrobenzene is precise only for wavelengths smaller than 1.1 μm, the dispersion of organic compounds varies only slowly in the infrared, so that we can extrapolate them into the longer wavelength region with reasonable accuracy.

6.2.3 Transmission curves

The transmission spectra of a 9.8 mm thick cuvette filled with carbon disulfide and nitrobenzene in the visible and near infrared region are shown in Fig. (6.2.2) (corrected for the cuvette reflection). Carbon disulfide exhibits no absorption in the visible and near infrared region. Nitrobenzene has a strong absorption at wavelengths larger than 1600 nm, however, it is transparent in the whole visible region and in the range between 1200 nm and 1600 nm.

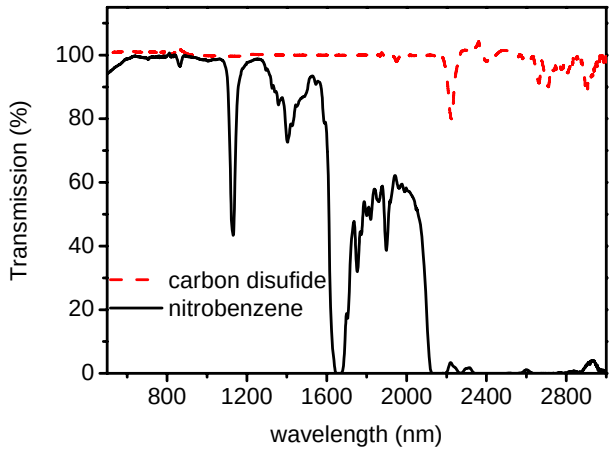

Fig. 6.2.2 The transmission curves of a 9.8 mm cuvette of carbon disulfide (red dashed), and nitrobenzene (black solid). Carbon disulfide has no absorption in the visible and near infrared region. I and my colleague Hongcang Guo measured the data using a CARY spectrophotometer in Prof. Russo's group.

6.3 Group velocity dispersion of the liquid-core photonic crystal fiber

The GVD is proportional to the second derivative of the propagation constant β with respect to ω, $D = -\frac{2\pi c}{\lambda^2}\frac{d^2\beta}{d\omega^2}$. Many methods for modeling are known to calculate the propagation constant, e.g., the effective-index method (EIM), the multipole method (MPM), and the beam-propagation method (BPM) [112-114]. In this paper, we simulate the GVD curve using a fully analytical vector approach of the effective-index method, which gives accurate results [115,116].

The propagation constant β can be characterized theoretically by solving the propagation equation in fibers:

$$\left[\frac{J_m'(\kappa r_{core})}{\kappa J_m(\kappa r_{core})}+\frac{K_m'(\gamma r_{core})}{\gamma K_m(\gamma r_{core})}\right]\left[\frac{J_m'(\kappa r_{core})}{\kappa J_m(\kappa r_{core})}+\frac{n_{eff}^2 K_m'(\gamma r_{core})}{n_{core}^2\gamma K_m(\gamma r_{core})}\right]=\left[\frac{m\beta k_0(n_{core}^2-n_{eff}^2)}{r_{core}\kappa^2\gamma^2 n_{core}}\right]^2, \quad (6.3.1)$$

where $\kappa^2 = n_{core}^2 k_0^2 - \beta^2$; $\gamma^2 = \beta^2 - n_{eff}^2 k_0^2$; $J_l(x)$ and $K_l(x)$ are the l^{th} order Bessel function and modified Bessel function, respectively. l=1 corresponds to the fundamental mode HE_{11} in the waist region; n_{core}, n_{eff} are the refractive indices of core and the effective index of cladding, respectively; r_{core} is the core radius, which is equal to $0.625\cdot\Lambda$ in silica-core PCF, however, in our case, is equal to the radius of the air hole a.

The cladding effective index n_{eff} is evaluated by the following equations:

$$\frac{I_{l+1}(w)}{I_l(w)} = -\frac{l}{w}-\frac{w}{2}\cdot\left(1+\frac{n_2^2}{n_1^2}\right)\cdot P - w\cdot\sqrt{\frac{1}{4}\cdot\left(1-\frac{n_2^2}{n_1^2}\right)^2\cdot P^2+\frac{l^2\cdot\left(\frac{1}{u^2}+\frac{1}{w^2}\right)\cdot\left(\frac{n_1^2}{w^2}+\frac{n_2^2}{u^2}\right)}{n_1^2}}; \quad (6.3.2)$$

$$P = \frac{Y_l(uR/a)\cdot J_l'(\xi)\big|_{\xi=u} - J_l(uR/a)\cdot Y_l'(\xi)\big|_{\xi=u}}{u\cdot(J_l(u)\cdot Y_l(uR/a) - Y_l(u)\cdot J_l(uR/a))}; \quad (6.3.3)$$

$$u = k_0^2\cdot(n_2^2 - n_{eff}^2)\cdot a^2 \qquad \text{and} \qquad w = k_0^2\cdot(n_{eff}^2 - n_1^2)\cdot a^2 \quad (6.3.4)$$

where, n_1 and n_2 are the refractive indices of air and silica, respectively, a is the radius of the air hole, R is the half of the pitch of the hexagonal lattice, J_l and Y_l are the l^{th} order Bessel function of the first order and second order, respectively, I_l is the l^{th} order modified Bessel function of the first kind, and l is equal to 1 for the fundamental mode EH_{11} in the cladding.

We designed one of the structures of LCPCFs which are capable to yield zero GVD in the infrared. The GVD curves are shown in Fig. 6.3.1 using the following

parameters: (a) the core is filled with nitrobenzene, the diameter of the core and air holes *d* is 4 μm, and the lattice pitch (the distance between centers of neighboring holes) Λ is 6.5 μm; (b) the core is filled with carbon disulfide, *d* is 3 μm, and Λ is 4.5 μm. The zero-dispersion wavelengths occur around 1.55 μm in the near infrared, and the GVD curves exhibit slow variations and small values.

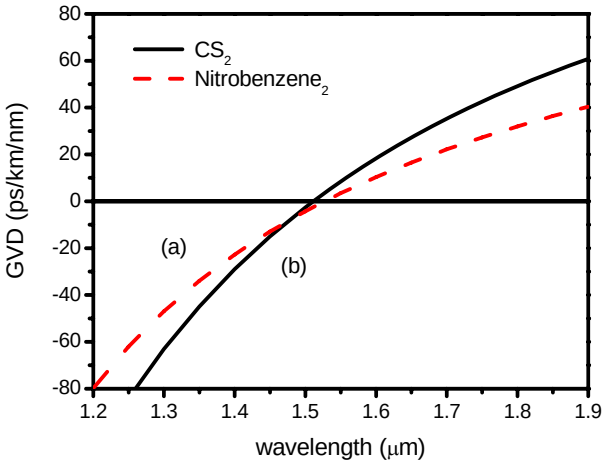

Fig. 6.3.1. GVD curves of the holey fiber with the center hole (a) filled with nitrobenzene (dashed), *d* is 4 μm and Λ is 6 μm, and (b) filled with CS_2 (solid), *d* is 3 μm, and Λ is 4.5 μm.

6.4 Response function of carbon disulfide

Although both of the LCPCF filled with carbon disulfide and nitrobenzene exhibited suitable GVD curves and showed huge potentials to generate supercontinuum, we only simulate the SC generation of LCPCF with carbon disulfide because of the capability of carbon disulfide to be transparent in the infrared region. In the simulation, the generalized scalar propagation equation, which is suitable for studying broad-band pulse evolution, is solved with split-step Fourier algorithm:

$$\frac{\partial A}{\partial z} - i \cdot \sum_{k \geq 2} \frac{i^2 \beta_k}{k!} \cdot \frac{\partial^2 A}{\partial t^k} = i\gamma \left(1 + i\tau_{shock} \frac{\partial}{\partial t} \right) \cdot \left(A \cdot \int_{-\infty}^{t} R(t') \left| A(z, t-t') \right|^2 dt' \right), \qquad (6.4.1)$$

where $A = A(z,t)$ is envelope of the electric field, β_k is the k^{th} order dispersion coefficient at center frequency ω_0, γ is the nonlinear coefficient, and *R(t)* is the response function of carbon disulfide. The timescale τ_{shock} includes the influence of the frequency-dependent effective mode area and can be written as [117]:

$$\tau_{shock} = \frac{1}{\omega_0} + \frac{d}{d\omega} \left[In \left(\frac{1}{n_{eff}(\omega) A_{eff}(\omega)} \right) \right]_{\omega_0}, \qquad (6.4.2)$$

where $n_{eff}(\omega)$ and $A_{eff}(\omega)$ are the effective index and effective area of the guided mode, respectively.

Unlike fused silica, the main mechanism responsible for the nonlinear refractive index is long-time response due to the molecular reorientation, which is induced by the tendency of molecules to become aligned in the electric field of an applied optical wave. The nonlinear refractive index, therefore, depends highly on the pulse duration. In this section, we derived the response function of carbon disulfide, which, as summarized by McMorrow *et al*. [118], includes instantaneous response due to electronic hyperpolarizability, subpicosecond response due to molecular librational motion, subpicosecond response due to collision- induced molecular polarizability, long-time response due to molecular reorientation and damped oscillation response due to Raman effect. Under the Born- Oppenheimer approximation [63], the response function, for optical pulses far from electronic resonance, can be written in the following way:

$$R(t) = f_e \cdot \delta(t) + (1 - f_e - f_R) \cdot h_m(t) + f_R \cdot h_R(t), \qquad (6.4.3)$$

where $f_e \cdot \delta(t)$, $(1 - f_e - f_R) \cdot h_m(t)$ and $f_R \cdot h_R(t)$ are electronic hyperpolarizability, molecular (including molecular librational motion, collision induced molecular

polarizability and molecular reorientation) and Raman effect contributions, respectively, with $\delta(t)$ of delta function, $\int_0^\infty h_m(t)\,dt = 1$, and $\int_0^\infty h_R(t)\,dt = 1$. f_e and f_R represent the fractional contribution of the electronic hyperpolarizability and Raman effect, respectively.

6.4.1. Contribution of electronic hyperpolarizability

According to the measurements on the third order hyperpolarizability, the electrical fractional contribution f_e is determined to be *11 %* [119].

6.4.2. Contribution of Raman effect

Following the analytic form of the Raman response function of fused silica by Keith J. Blow *et al*., we write the response function of carbon disulfide as follows:

$$h_R(t) = \frac{\tau_1^2 + \tau_2^2}{\tau_1 \tau_2^2} \exp(-t/\tau_2)\sin(t/\tau_1), \tag{6.4.4}$$

where the inverse time scale corresponds to the frequency of the peak of the Raman gain spectrum, and the decay rate corresponds to the width of the gain spectrum. Table 6.4.1 shows Raman modes of carbon disulfide in which stimulated Raman scattering was observed [120]. From the data sheet in Table 6.4.1, we choose here the values of $\tau_1 = 0.0081$ *ps* and $\tau_2 = 21.2$ *ps*. According to Eq. (6.4.5) [68], f_R is determined to be 0.3%.

$$g(\Delta\omega) = (2\omega_p / c) f_R n_2 \,\mathrm{Im}(\tilde{h}_R(\Delta\omega)), \tag{6.4.5}$$

where *Im* stands for the imaginary part, *g(Δω)* represents the Raman gain spectrum, and $\tilde{h}_R(\Delta\omega)$ is the Fourier transform of Raman response function $h_R(t)$.

Table 6.4.1 Raman modes of carbon disulfide

substance	Frequency shift (cm^{-1})	Line width (cm^{-1})	Gain factor g_R (10^{-10} *m/ W*)
Carbon disulfide	655.6	0.5	2.4

However, when using this formula as Raman response function of carbon disulfide, we should be very careful. First, besides the strongest Raman mode at 653 cm^{-1}, which is considered in Eq. (6.4.4), the weaker Raman mode at 392 cm^{-1} should be also taken into account. Although the strength of this mode is two orders weaker

than the mode at 653 cm^{-1} due to its smaller resonance frequency and much larger line width it will contribute to the Raman response function. However, lacking of experimental results on this mode, at present it is impossible to determine the its fractional contribution. Second, the Raman active mode at 653 cm^{-1} is hard to excite. Pulses with extremely large bandwidth and short pulse duration (less than 20 fs) are required to excite those Raman-active modes in the molecule. In our case, where the pulse duration is more than 100 fs, we should state that the Raman-active mode at 653 cm^{-1} can not be excited and therefore the Raman fractional contribution f_R is set to be zero. However, another problem arises and makes the situation very complex. As we know, during the initial stage of supercontinuum generation, the higher order soliton splits into its fundamental solitons (details can be found in section 2.6). Each of those fundamental solitons has a peak powers and pulse durations as follows [37]:

$$P_k = \frac{(2N-2k+1)^2}{N^2} P_p \,, \qquad T_k = \frac{T_0}{2N-2k+1}, \tag{6.4.6}$$

where N is the higher-order soliton number, P_p and T_0 represent the input peak power and input pulse duration, respectively. It is clear that the fundamental solitons can have much shorter pulse durations. In the case of input pulse duration of 100 fs and N equal to 20, the first fundamental soliton has a pulse duration around 2.5 fs. This property demonstrates that some of the fundamental solitons can indeed excite the Raman-active modes. Due to the fact that some components in a pulse can excite the Raman modes and others cannot, it is impossible for us to determine a universal Raman response function and a Raman fractional contribution at present. We are looking forward to further research on the Raman gain spectrum and temporal properties of the Raman effect in carbon disulfide. Raman gain is the main mechanism leading to soliton self-frequency shift and consequently forming the red-shifted Raman soliton. Therefore, in order to obtain conservative spectra of the supercontinuum generation, we consider the Raman fractional contribution to be zero in our simulations.

6.4.3. Molecular contribution

The molecular contribution to the nonlinear optical response including molecular librational motion, collision-induced molecular polarizability and molecular reorientation, can be determined by a time- resolved optical Kerr- effect experiment. Based on the Born- Oppenheimer approximation, the molecular time-scale response of carbon disulfide was revealed, as shown in Fig. 6.4.1. A model functional form to

express the molecular response was obtained [121], although this form was lacking rigorous physical justification. After normalization, the functional form of $h_m(t)$ can be written as follows:

$$h_m(t) = 0.5048 \cdot \exp(-\frac{t}{\tau_{diff}})(1-\exp(-\frac{t}{\tau_{rise}})) + 0.8314 \cdot \exp(-\frac{t}{\tau_{\text{int}}})(1-\exp(-\frac{t}{\tau_{rise}})) + 1.633 \cdot \exp(-\frac{\alpha^2 t^2}{2})\sin(\omega_0 t), \quad (6.4.7)$$

where τ_{diff} = 1.68 *ps*, τ_{rise} = 0.14 *ps*, τ_{int} = 0.4 *ps*, α = 5.4 */ps*, and ω_0 = 6.72 */ps*. According to the estimate of f_e and f_R above, the fractional contribution of the molecular dynamics is determined to be 89%.

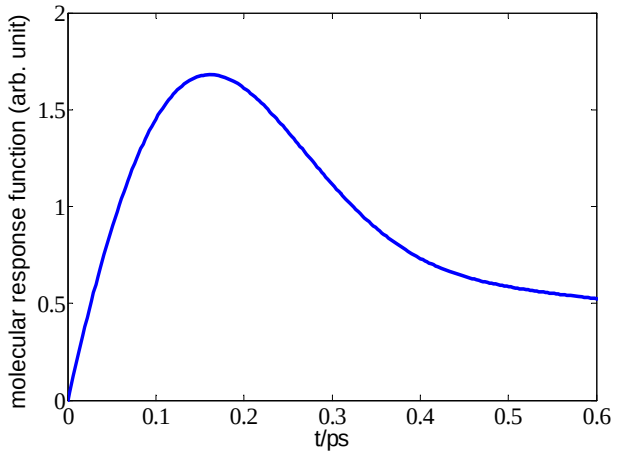

Fig. 6.4.1 The normalized molecular response function of carbon disulfide with a relaxation time of 1.68 *ps*.

6.5 Theoretical simulations of supercontinuum in liquid-core photonic crystal fiber

The fiber used in our simulations has a core diameter of 3 μm, a lattice pitch of 5 μm, and a length of 5 mm. Its centre hole was filled by CS_2. Since the resulting spectrum relies on the input pulse duration due to the molecular response, we simulated the spectra with input duration of 100 fs and 500 fs, respectively. The dispersion effects are considered up to the 14^{th} order, and the dispersion coefficients are shown in the appendix. The nonlinear parameter γ is evaluated to be 2.45 /W/m (compared with the nonlinear parameter of 0.11 /W/m in a silica PCF, which has a core diameter of 1.4 μm and pumping wavelength of 800 nm [117]), and the input peak power used in the simulation is 10 kW. Actually, the inexact evaluation of dispersion coefficients and the neglected Raman effect can lead to imprecise results of the generation, however, it is reasonable to consider the simulated bandwidths of the spectra as indicative. Figure 6.5.1 and Fig. 6.5.2 show the SC spectra generated by the CS_2-filled LCPCF with the pulse duration of 100 fs and 500 fs, respectively. The figures demonstrate that a liquid-core PCF is capable to generate supercontinua with dramatically broadened spectra, which cover a range from 700 nm to more than 2500 nm. The output spectra depend on the input pulse duration, with the longer pulse duration causing a broader spectrum. Increasing the input power and fiber length can further broaden the spectra.

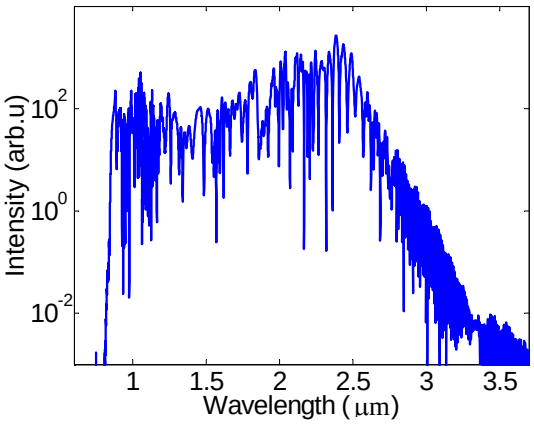

Fig. 6.5.1 The calculated output spectrum (logarithmic) generated by the LCPCF with input peak power of 10 kW and pulse duration of 100 fs.

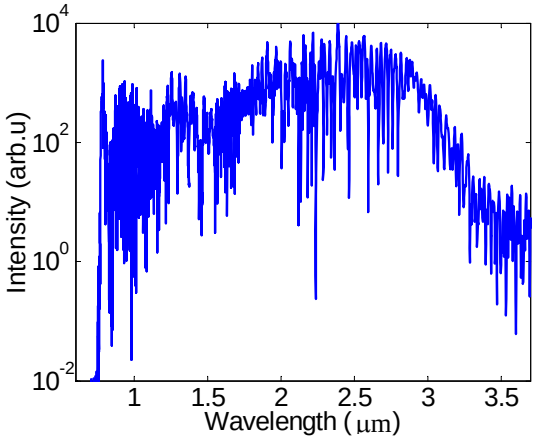

Fig. 6.5.2 The calculated output spectrum (logarithmic) generated by the LCPCF with input peak power of 10 kW and pulse duration of 500 fs.

Due to the high nonlinearity, a liquid-core PCF is of capability to generate supercontinua with low input peak power as well. We simulated the spectral property

of SC generation with the input peak power 1 kW and pulse duration 500 fs, as shown in Fig. 6.5.3. The PCF used in the simulation has a core diameter of 3 μm, a lattice pitch of 5 μm, and a length of 10 mm. With pumping wavelength at 1550 nm, the resulting spectrum covers a range of 1100 nm, from 1000 nm to 2100 nm.

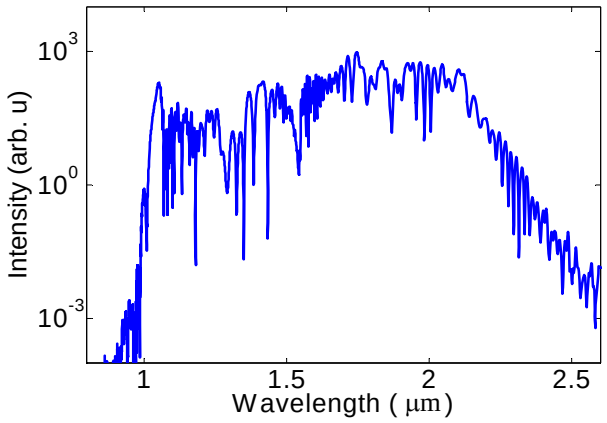

Fig. 6.5.3 The calculated output spectrum (logarithmic) generated by the LCPCF with input peak power of 1 kW and pulse duration of 500 fs.

6.6 Guided modes in liquid-core photonic crystal fiber

The high refractive index of the liquid core leads to multi-mode propagation in a liquid-core PCF. The *V*-parameter $V = \frac{\pi \cdot d}{\lambda} \cdot \sqrt{\left(n_{core}^2 - n_{eff}^2\right)}$ is equal to 4.37 in the case of the core being filled with carbon disulfide. Despite the capability to generate a supercontinuum provided by a highly nonlinear multi-moded fiber, one difficulty arises, namely when an output beam with good spatial characteristics and little mode dispersion, or more specifically, single-mode transverse characteristics, is required. Single mode propagation and output can be obtained using adiabatic coupling in the following way: A single mode PCF with the same propagation constant as that of the fundamental mode in LCPCF can be used to generate a single mode beam, which is subsequently launched into the LCPCF. The incident mode can couple only to modes with the same azimuthal symmetry and with a similar propagation constant [78], and then the fundamental mode becomes the dominant guided mode in the LCPCF. In the process of propagation in the LCPCF, negligible coupling and small power loss from the fundamental mode to the higher order modes occur, because the small core and large core-cladding index difference of the LCPCF requires a large perturbation to couple to the higher order modes. Therefore, the fundamental mode propagates within a good approximation adiabatically in the LCPCF, similar to light propagating in a single mode along a tapered fiber [24].

Section 7 Summary and outlook

7.1 Summary

Tapered fibers and photonic crystal fibers have shown huge potential to generate supercontinuum radiation, which has found numerous applications in optical coherence tomography, spectroscopy, pump-probe measurements, optical frequency metrology, and so on. In this dissertation, we comprehensively discussed the generation mechanisms of the supercontinuum generation, described the comprehensively propagation characteristics of tapered fibers, and for the first time designed the technologies to specifically tailor the group velocity dispersion of tapered fibers, realizing singly polarized supercontinuum radiation using tapered fibers, and dramatically broadened the generated spectrum with a new liquid filled highly nonlinear photonic crystal fiber. This research work has improved the spectral characteristics of tapered fibers and photonic crystal fibers, which can be applied directly in many research fields such as spectroscopy, atom trapping, and telecommunication.

I summarize our research work as follows:

- We solved the nonlinear Schrödinger equation to simulate the supercontinuum generation and studied in detail the generation mechanisms.

Using the split-step Fourier method, we solved the nonlinear Schrödinger equation to simulate the spectral and temporal properties of the supercontinuum generation. Through the comparisons of theoretical simulations and experiment results, we found the theoretical simulations can not only adequately model the width of the generated spectrum, but also precisely predict the positions of distinct spectral peaks.

The supercontinuum generation is a complex nonlinear phenomenon. The mechanisms behind SC generation arise from the interaction between dispersion and nonlinear effects, including selfphase modulation, soliton formation, soliton splitting, self steepening, soliton self frequency shift, and Raman scattering.

- We studied the mode and group velocity dispersion (GVD) evolution in the tapered transition region of a tapered fiber

Through precise calculations, we calculated for the first time the evolution of the transverse intensity distribution, the nonlinear parameter, and the GVD of the fiber

mode in the taper region of a tapered fiber. We have demonstrated this complete characterization of light propagation and nonlinear interaction processes in tapered fibers, which should be taken into account in both experimental analysis and device design. We have especially pointed out that the dispersion of the GVD and the nonlinear interaction within the taper region has significant influence on the propagation of spectrally broad supercontinuum pulses.

- We tailored the group velocity dispersion of tapered fibers by immersing them in different liquids

Our theoretical calculations revealed for the first time that the design of the GVD in tapered fibers can be tailored when we immerse the fibers in transparent liquids (such as acetonitrile, pentane, and hexane). The GVD curves exhibit slow variations and small values (<40 ps/km/nm) in the anomalous dispersion region. The second zero-dispersion wavelength (ZDW) of the GVD curve can be generated in the infrared (e.g., around 1.55 μm). When mixing pentane and hexane, the ZDW can be fine-tuned to match the center frequency of the pump pulse around 1.55 μm, which can optimize supercontinuum generation. By use of alternative fiber materials (BK7, SF6, and SF59) for the tapered fiber and immersing them into chlorobenzene, we can reduce the diameter of the fiber taper to 3 μm and position the first ZDW of the GVD curve in the telecommunication window. Finally, spectrum simulations demonstrate that a tapered fiber immersed in liquid Series AAA (Cargille) is capable to generate the supercontinuum with dramatically broadened spectrum ranging from 700 nm to 2000 nm.

- We theoretically realized the design of a singly polarized supercontinuum generation with tapered fibers

We designed a polarization-maintaining tapered fiber and calculated birefringence and group velocity dispersion as a function of wavelength of the dominant modes. For the first time our elliptically tapered fiber demonstrated an extremely large birefringence and a small beat length, which make the fiber suitable for maintaining the linear polarization state and generating a singly polarized supercontinuum. By changing the polarization state of the incident light, we could fine-tune the zero dispersion wavelength, which is critical with regards to the spectrum of the generated supercontinuum.

- We theoretically calculated the dramatically broadened supercontinuum by using a liquid-core filled photonic crystal fiber

We designed a new nonlinear fiber to generate supercontinuum radiation with dramatically broadened spectrum by filling highly nonlinear liquid into hollow photonic crystal fibers for the first time. The liquid-core photonic crystal fiber (PCF) with carbon disulfide and nitrobenzene filled into the core exhibits an extremely high nonlinear parameter γ, which can be more than 20 times larger than that of a conventional PCF. The GVD curves of the liquid-core PCF display slow variation and small absolute values in the anomalous dispersion region, and the zero dispersion wavelength lies around 1.55 μm in the near infrared, making LCPCFs ideal media for supercontinuum generation. Simulation demonstrates that the spectrum generated by this new nonlinear fiber ranges from 700 nm to more than 3000 nm. In order to accomplish this task, we had to determine a complete *quantitative* Raman response function of the liquid in the femtosecond and picosecond regime for the first time.

7.2 Outlook

Based on the present work, we suggest the following projects in the future:

- Improve the spectral characteristics by introducing a diameter variation of the waist diameter along the fiber

The nonlinear Schrödinger equation is well suited to simulate the temporal and spectral properties of supercontinuum generation. In the generation of SC radiation, phase velocity mismatch and group velocity mismatch lead to lower efficiency and narrower generated spectra. Using the nonlinear Schrödinger equation, we are able to design an optimized variation function of waist diameter along the fiber, which can minimize those conditions and improve the generated spectrum.

- Fabricate a polarization-maintaining tapered fiber

A tapered fiber with elliptical cross section in the waist region is capable to maintain an incident linear polarization state throughout the propagation path and generates a highly polarized supercontinuum. However, as we discussed in section 5.6, it is difficult to maintain the elliptical perform shape during the fabrication process of a tapered fiber, as the strong surface tension can deform the noncircular cross-section into a circular one. Therefore it is a great challenge to fabricate such a fiber in the lab. We plan to prevent the fiber from the deformation by enhancing the ratio between viscosity and surface tension of the fiber. In other words, during the fiber drawing process, we forceably cool down the softened fiber before surface tension can stress it into a circular fiber.

- Complete the response function of carbon disulfide and have the new nonlinear fiber manufactured

A full response function of carbon disulfide is of scientific interest and importance in the field of nonlinear optics. At present, lacking experimental results on a more detailed Raman gain spectrum and lacking the temporal properties of the Raman effect in carbon disulfide, it is impossible to determine its full response function. We will design an experimental setup to measure the Raman gain spectrum as well as its temporal properties, with which a full understanding of the time resolved Raman effect down to the few-*fs*-regime in carbon disulfide can be achieved.

We also plan to have the new nonlinear fiber manufactured. We will fill carbon disulfide into a hollow photonic crystal fiber by vaporizing carbon disulfide, injecting it into the core of the hollow PCF, and then cooling down the gas to condense the liquid.

- Design a liquid-crystal-core photonic crystal fiber

Liquid crystals have many favorable characteristics, which can be used to generate an adjustable supercontinuum generation by applying an external electric field. The spectral properties generated by such a fiber can be easily modulated by varying the strength and direction of the external electric field. Furthermore, applying the electric field along the fiber with different strength is able to realize quasi-phase matching and to satisfy the group velocity matching condition, which will definitely improve the spectral characteristics of the supercontinuum generation. In fact, the property to control the optical generation by external electrical fields, is favorable in many applications such as telecommunication, optical data transmission, and so on.

Cargille Laboratories
55 Commerce Rd - Cedar Grove, NJ 07009-1289
Phone : 973-239-6633 - Fax : 973-239-6096 - Web : www.cargille.com

Typical Characteristics

Refractive Index Liquid	**Series AAA**					
Refractive Index	**1.35000**	at	5893 Å	and	25	° C

Compostition	Perfluorocarbon and Chlorofluorocarbon (not the types thought to affect the ozone)
Appearance	Colorless Liquid
Odor	None
Color Stability	In sun: no visible change after 10 years
Index Change Rate	Moderate : -0.00030 to +0.00009
by Evaporation	expected after 32 days with exposed surface area to volume ratio of 0.2 cm^2/cc @ 25 °C

Pour Point	< -20	°C
Boiling Point	> 215	°C (760 mm Hg)
Flash Point	None	°C (COC)
Density	1.921	g / cc at 25 °C
Density Temp Coef	-0.0019	g / cc / °C
Coef of Thermal Expansion	0.0010	cc / cc / °C
Thermal Conductivity	0.00029	cal / sec / cm^2 / °C - 1 cm thickness
Viscosity	16	cSt at 25 °C
Surface Tension	18	dynes/cm at 25 °C

Soluble	Other Chlorofluorocarbons
Partly Soluble	Most organic solvents
Insoluble	Water

Compatible	10 Month Immersion at 25 °C: Acrylic, Cellulose Acetate, Epoxy, Mylar, Nylon, Polycarbonate, Polyester, Polyethylene, Polypropylene, Polystyrene, Polyurethane, Polyvinyl Chloride, Phenolic, Teflon, Latex, Neoprene, Silicone (Sylgard 184, 3140 RTV), and Fluorosilicone (Silastic 730 RTV) Rubbers ; Tygon F-4040-A, Tygothane, Brass, Copper, Steel
Incompatible	Burna-S, Natural, and some Silicone Rubbers; Tygon S-50-HL, R-3603, B-44-3; Chlorotrifluoro Ethylene Polymers, Aluminum

Toxicity	None (Request MSDS)

Refractive Index Liquid **Series AAA**
Refractive Index **1.35000** at 5893 Å and 25 ° C

Cauchy Coefficients	A	B	C
	1.3432154	237036	-4.943692E+10

Cauchy Formula $A + B / \lambda^2 + C / \lambda^4$ (λ = Wavelength in Angstroms)

		Transmittance			
Wavelength (in Å)	Refractive Index	0.1 mm	1 mm	1 cm	10 cm
2250	-	-	-	-	-
2400	1.38	99	91	37	0
2480	1.38	99	95	57	0
2700	1.375	100	98	80	11
2900	1.371	100	99	88	27
3080	1.368	100	99	92	43
3370	1.364	100	100	96	64
3650	1.3607	100	100	97	78
4047	1.3575	100	100	98	83
4861	1.3532	100	100	99	95
5461	1.3511	100	100	99	95
5893	1.3500	100	100	100	96
6328	1.3491	100	100	100	97
6563	1.3487	100	100	100	97
6943	1.3481	100	100	100	98
8400	1.3466	100	100	100	96
10648	1.3453	100	100	100	96
13000	1.345	100	100	100	96
15500	1.344	100	100	99	89
25000	1.34	100	99	91	39
37000	1.34	98	81	11	0

$(n_F - n_C)$	0.0045	
Abbe v_D	78.4	
Temp. Coefficient	-0.000339	dn_D/dt (15 - 35 °C)

Literature:

1. T. A. Birks, W. J. Wadsworth, and P. St. J. Russell, "Supercontinuum generation in tapered fibers," Opt. Lett. **25**, 1415-1417 (2000).
2. J. Teipel, K. Franke, D. Tuerke, F. Warken, D. Meiser, M. Leuschner, and H. Giessen, "Characteristics of supercontinuum generation in tapered fibers using femtosecond laser pulses," Appl. Phys. B **77**, 245-250 (2003).
3. W. J. Wadsworth, A. Ortigosa-Blanch, J. C. Knight, T. A. Birks, T. P. M. Man, and P. St. J. Russell, "Supercontinuum generation in photonic crystal fibers and optical fiber tapers: a novel light source," J. Opt. Soc. Am. B **19**, 2148-2155 (2002).
4. J. M. Harbold, F. Oe. Ilday, F. W. Wise, T. A. Birks, W. J. Wadsworth and Z. Chen, "Long-wavelength continuum generation about the second dispersion zero of a tapered fiber," Opt. Lett. **27**, 1558-1560 (2002).
5. T. P. M. Man, T. A. Birks, W. J. Wadsworth, and P. St. J. Russell, "Fabrication of indefinitely long tapered fibers for supercontinuum generation," Nonlinear Guided Waves and Their Applications, Vol. **55** of OSA Trends in Optics and Photonics, paper WB4 (2001).
6. R. R. Alfano and S. L. Shapiro, "Emission in the Region 4000 to 7000 Å Via Four-Photon Coupling in Glass", Phys. Rev. Lett., **24,** 584 (1970).
7. D. A. Jones, S. A. Diddams, J. K. Ranka, A. Stentz, R. S. Windeler, J. L. Hall, and S. T. Cundiff, "Carrier-envelope phase control of femtosecond mode-locked lasers and direct optical frequency synthesis," Science **288**, 635-639 (2000).
8. S. A. Diddams, D. J. Jones, J. Ye, S. T. Cundiff, J. L. Hall, J. K. Ranka, and R. S. Windeler, "Direct rf to optical frequency measurements with a femtosecond laser comb," IEEE Trans. Instrum. Meas. **50**, 552-555 (2001) .
9. R. Holzwarth, Th. Udem, T. W. Hänsch, J. C. Knight, W. J. Wadsworth, and P. St. J. Russel, "Optical frequency synthesizer for precision spectroscopy," Phys. Rev. Lett. **85**, 2264 (2000).
10. I. Hartl, X. D. Li, C. Chudoba, R. K. Ghanta, T. H. Ko, and J. G. Fujimoto, "Ultrahigh-resolution optical coherence tomography using continuum generation in a air-silica microstructure optical fiber," Opt. Lett. **26**, 608-610 (2001).

11. R. E. Drullinger, S. A. Diddams, K. R. Vogel, C. W. Oates, E. A. Curtis, W. D. Lee, W. M. Itano, L. Hollberg, and J. C. Bergquist, “All-optical atomic clockes,” International Frequency Control Symposium and PDA Exhibition, 69-75 (2001).
12. Robert R. Alfano, “*The Supercontinuum Laser Source- Fundamentals with Updated References*”, Second Edition, 2006, Springer Science + Business Media, Inc.
13. P. Rigby, “A photonic crystal fibre,” Nature, **396**, 415-416 (1998).
14. P. St. J. Russell, “Photonic crystal fibres,” Science **299**, 358-362 (2003).
15. J. C. Knight, T. A. Birks, P. St. J. Russell, and D. M. Aktin, “All-silica single-mode optical fiber with photonic crystal cladding,” Opt. Lett. **21**, 1547-1549 (1996).
16. J. K. Ranka, R. S. Windeler, and J. Andrew, “Visible continuum generation in air-silica microstructure optical fibers with anomalous dispersion at 800 nm,” Opt. Lett. **25**, 25-27 (2000).
17. T. P. Hansen, J. Broeng, S. E. B. Libori, A. Bjarklev, “Highly birefringent index-guiding photonic crystal fibers,” IEEE Photon. Tech. Lett. **13**, 588-590 (2001).
18. J. C. Knight, T. A. Birks, R. F. Cregan, P. S. Russell, J. P. de Sandro, “Large mode area photonic crystal fibre,” IEE Electron. Lett. **34**, 1347-1348 (1998).
19. C. M. B. Cordeiro, W. J. Wadsworth, and T. A. Birks, “Engineering the dispersion of tapered fibers for supercontinuum generation with a 1064 nm pump laser,” Opt. Lett. **30**, 1980-1982 (2005).
20. F. Warken and H. Giessen, “Fast profile measurement of micrometer-sized tapered fibers with better than 50-nm accuracy,” Opt. Lett. **29**, 1727-1729 (2004).
21. R. Zhang, X. Zhang, D. Meiser, and H. Giessen, “Mode and group velocity dispersion evolution in the tapered region of a single-mode tapered fiber,” Opt. Express **12**, 5840-5849 (2004).
22. D. Türke, J. Teipel, A. Zintl, B. Braun, and H. Giessen, “Compact high power (5.6 W) picosecond white light source,” *CLEO/IQEC and* PhAST *Technical Digest on* CD-ROM (The Optical Society of America, Washington, DC, 2004), CThHH5.

23. J. Teipel, D. Türke, and H. Giessen, "Diode-pumped, ultrafast, multi-octave supercontinuum source at repetition rates between 500 kHz and 20 MHz using Yb:glass lasers and tapered fibers," Opt. Express, **13**, 1477 (2005).

24. R. Zhang, J. Teipel, X. Zhang, D. Nau, and H. Giessen, "Group velocity dispersion of tapered fibers immersed in different liquids," Opt. Express **12**, 1700-1708 (2004).

25. G. P. Agrawal, "*Nonlinear Fiber Optics – Optics and Photonics*", Third Edition, 2001, Academic Press.

26. M. J. Adams, "An introduction to Optical Waveguides", 1981, Wiley, New York.

27. F. Shimizu, "Frequency Broadening in Liquids by a Short Light Pulse," Phys. Rev. Lett., **19**, 1097-1100 (1967).

28. Y. R. Shen and M. M. T. Loy, "Theoretical Interpretation of Small-Scale Filaments of Light Originating from Moving Focal Spots," Phys. Rev. A **3**, 2099-2105 (1971).

29. R. H. Stolen and C. Lin, "Self-phase-modulation in silica optical fibers," Phys. Rev. A **17**, 1448-1453 (1978).

30. R. H. Stolen, J. E. Bjorkholm, and A. Ashkin, "Phase-matched three-wave mixing in silica fiber optical waveguides ," Appl. Phys. Lett. **24**, 308-310 (1974).

31. W. J. Wadsworth, N. Joly, J. C. Knight, T. A. Birks, F. Biancalana, P. St. J. Russell, "Supercontinuum and four-wave mixing with Q-switched pulses in endlessly single-mode photonic crystal fibres," Opt. Express **12**, 299-309 (2004).

32. S. Coen, AHL. Chau, R. Leonhardt, J. D. Harvey, J. C. Knight, W. J. Wadsworth, P. St. J. Russell, "Supercontinuum generation by stimulated Raman scattering and parametric four-wave mixing in photonic crystal fibers," J. Opt. Soc. Am. B, **19**, 753-764, (2002).

33. J. C. Travers, S. V. Popov, and J. R. Taylor, "Extended blue supercontinuum generation in cascaded holey fibers," Opt. Lett., **30**, 3132-3134 (2005).

34. S. A. Akhmanov, R. V. Khokhlov, and A. P. Sukhorukov, "Laser Handbook", 1972, North-Holland, Amsterdam.

35. G. Genty, M. Lehtonen, and H. Ludvigsen, "Effect of cross-phase modulation on supercontinuum generated in microstructured fibers with sub- 30 fs pulses," Opt. Express **12**, 4614-4624 (2004).

36. G. Genty, M. Lehtonen, and H. Ludvigsen, “Route to broadband blue-light generation in microstructured fibers,” Opt. Lett. **30**, 765-758 (2005).

37. T. Schreiber, T. V. Andersen, D. Schimpf, J. Limpert, A. Tünnermann, “ Supercontinuum generation by femtosecond single and dual wavelength pumping in photonic crystal fibers with two zero dispersion wavelengths, ” Opt. Express **13**, 9556-9569 (2005).

38. Y. R. Shen, “The Principles of Nonlinear Optics,” 1984, Wiley, New York.

39. R. W. Boyd, “Nonlinear optics”, 1992, Academic Press.

40. G. Genty, M. Lehtonen, H. Ludvigsen, J. Broeng, and M. Kaivola, “Spectral broadening of femtosecond pulses into continuum radiation in microstructured fibers,” Opt. Express **10**, 1083-1098 (2002).

41. A. V. Husakou and J. Herrmann, “Supercontinuum Generation of Higher-Order Solitons by Fission in Photonic Crystal Fibers,” Phys. Rev. Lett. **87**, 203901 (2001).

42. J. Herrmann, U. Griebner, N. Zhavoronkov, A. Husakou, D. Nickel, J. C. Knight, W. J. Wadsworth, P. St.J. Russell, and G. Korn, “Experimental Evidence for Supercontinuum Generation by Fission of Higher-Order Solitons in Photonic Fibers,” Phys. Rev. Lett. **88**, 173901-1-173901-4 (2002).

43. A. V. Husakou and J. Herrman, “Supercontinuum generation, four-wave mixing, and fission of higher-order solitons in photonic-crystal fibers**,**” J. Opt. Soc. Am. B, **19**, 2171 (2002).

44. J. M. Dudley, and S. Coen, “Numerical simulations and coherence properties of supercontinuum generation in photonic crystal and tapered optical fibers”, IEEE J. of Selected Topics in Quantum Electronics **8**, 651-659 (2002).

45. R. A. Fisher and W. K. Bischel, “The role of linear dispersion in plane-wave self-phase modulation,” Appl. Phys. Lett. **23**, 661-663 (1975).

46. K. J. Blow and D. Wood, “Theoretical description of transient stimulated Raman scattering in optical fibers,” IEEE J. Quantum Electron., **25**, 2665-2673 (1989).

47. H. J. R. Dutton, “Understanding optical communications”, 1998, International Business Machines Corporation.

48. C. Yeh, “Handbook of Fiber Optics”, 1990, Academic Press, Inc.

49. A. W. Snyder, “Asymptotic expressions for eigenfunctions and eigenvalues of a dielectric or optical waveguide,” IEEE Trans. Microwave Theory Tech. MIT **17**, 1130-1138, 1969.

50. L. B. Jeunhomme, “Single-mode Fiber Optics,” 1990, Marcel Dekker, Inc.
51. A. Ghatak; K. Thyagarajan, “Introduction to fiber optics”, 1998, Cambridge University Press.
52. J. Teipel, D. Türke, and H. Giessen, “Compact multi-Watt picosecond coherent white light sources using multiple-taper fibers,” Opt. Express, **13**, 1734 (2005).
53. T. Schneider, “Nonlinear Optics in Telecommunications,” 2004, Springer-Verlag Berlin Heidelberg.
54. P. Diament, “Wave Transmission and Fiber Optics,” 1990, Macmillan, New York.
55. A. W. Snyder, J. D. Love, “Optical waveguide theory”, 2000, Kluwer Academic Publishers.
56. D. Marcuse, “Theory of Dielectric Optical Waveguides”, 1991, Academic Press.
57. J. A. Buck, “Fundamentals of Optical Fibers”, 1995, Wiley.
58. A. Hasegawa and F. Tappert, “Transmission of stationary nonlinear optical pulses in dispersive dielectric fibers. I. Anomalous dispersion,” Appl. Phys. Lett. **23**, 142-144 (1973).
59. R. K. Bulough, P. M. Jack, P. W. Kitchenside, and R. Saunders, “Solitons in laser physics,” Phys. Scr. **20**, 364-381 (1979).
60. P. K. A. Wai, C. R. Menyuk, H. H. Chen, and Y. C. Lee, “Soliton at the zero-group-dispersion wavelength of a single-mode fiber,” Opt. Lett. **12**, 628-630 (1987).
61. N. Akhmediev and M. Karlsson, “Cherenkov radiation emitted by solitons in optical fibers,” Phys. Rev. A **51**, 2602-2607 (1995).
62. J. N. Elgin, T. Brabec, and S. M. J. Kelly, “A perturbative theory of soliton propagation in the presence of third-order dispersion,” Opt. Commun. **114**, 321-328 (1995).
63. R. W. Hellwarth, “Third-order optical susceptibilities of liquids and solids,” Prog. Quant. Electr., **5**, 1-68, (1977).
64. G. P. Agrawal, “*Nonlinear Fiber Optics – Optics and Photonics*”, Page 104-106, Third Edition, 2001, Academic Press.
65. G. P. Agrawal, “*Nonlinear Fiber Optics – Optics and Photonics*”, Page 154, Third Edition, 2001, Academic Press.

66. R. H. Stolen, E. P. Ippen, and A. R. Tynes, “Raman Oscillation in Glass Optical Waveguide,” Appl. Phys. Lett. 20, 62-64 (1972).

67. R. H. Stolen and E. P. Ippen, “Raman gain in glass optical waveguides,” Appl. Phys. Lett. **22**, 276-278 (1973).

68. R. H. Stolen and J. P. Gordon, “Raman response function of silica-core fibers”, J. Opt. Soc. Am. B, **6**, 1159 (1989).

69. R. Hellwarth, J. Cherlow, and T. Yang, “Origin and frequency dependence of nonlinear opical susceptibilities of glasses,” Phys. Rev. B, **11**, 964-967 (1975).

70. G. P. Agrawal, “*Nonlinear Fiber Optics – Optics and Photonics*”, Page 46-48, Third Edition, 2001, Academic Press.

71. C. Cheng, X. Wang, Z. Fang and B. Shen, “Nonlinear copropagation of two optical pulses of different frequencies in photonic crystal fibers,” Appl. Phys. B, **80**, 291-294 (2005).

72. F. M. Mitschke and L. F. Mollenauer, “Discovery of the soliton self-frequency shift,” Opt. Lett., **11**, 659-661 (1986).

73. D. V. Skryabin, F. Luan, J. C. Knight, P. St. J. Russell, “Soliton Self-Frequency Shift Cancellation in Photonic Crystal Fibers,” Science, **19**, 1705-1708 (2003).

74. K. M. Hilligsøe, H. N. Paulsen, J. Thøgersen, S. R. Keiding, and J. J. Larsen, “Initial steps of supercontinuum generation in photonic crystal fibers,” J. Opt. Soc. Am. B **20**, 1887-1893 (2003).

75. I. Cristiani, R. Tediosi, L. Tartara, and V. Degiorgio, “ Dispersive wave generation by solitons in microstructured optical fibers,” Opt. Express **12**, 124-135 (2004).

76. L. Tartara, I. Cristiani, and V. Degiorgio, “Blue light and infrared comtinuum generation by soliton fission in microstructured fibers,” Appl. Phys. B, **77**, 307 (2003).

77. J. Teipel and H. Giessen, “Tapered fiber femtosecond optical parametric oscillator,” presented at CLEO/QELS, Baltimore, Maryland, USA, 1-6 June (2003), Paper CMO3.

78. J. D. Love, W. M. Henry, W. J. Stewart, R. J. Black, S. Lacroix, and F. Gonthier, “Tapered Single-mode Fibres and Devices Part 1: Adiabaticity Criteria,” IEE Proceedings-J, **138**, 343-354 (1991) .

79. M. Monerie, “Propagation in Doubly Clad Single-mode Fibers,” IEEE Transactions on Microwave Theory and Techniques, **MTT-30**, 381-388 (1982).

80. A. J. Fielding, K. Edinger, and C. C. Davis, “Experimental Observation of Mode Evolution in Single-Mode Tapered Optical Fibers,” Journal of Lightwave Technology, **17**, 1649-1656 (1999).

81. R. J. Black and R. Bourbonnais, “Core-mode cutoff for finite-cladding lightguides,” IEE Proceedings-J, **133**, 377-384 (1986).

82. W. H. Reeves, J. C. Knight, P. S. J. Russell, and P. J. Roberts, "Demonstration of ultra-flattened dispersion in photonic crystal fibers," Optics Express **10**, 609-613 (2002).

83. C. Kerbage, R.S. Windeler, B.J. Eggleton, P. Mach, M. Dolinski, and J.A. Rogers, “Tunable devices based on dynamic positioning of micro-fluids in micro-structured optical fiber,” Opt. Comm. **204**, 179-184 (2002).

84. Warren J. Smith, “Modern optical engineering”, the second edition., McGraw Hill, 1990, p. 174.

85. J. Bertie, “Acetonitrile-water mixtures,” J. Phys. Chemistry, **101**, 4111 - 4119 (1997).

86. IAPWS 5C: "Release on refractive index of ordinary water substance as a function of wavelength, temperature and pressure," (September 1997), published by International Association for the Properties of Water and Steam.

87. V. V. Ravi Kanth Kumar, A. K. George, W. H. Reeves, J. C. Knight, and P. St. J. Russell, “Extruded soft glass photonic crystal fiber for ultrabroad supercontinuum generation,” Opt. Express **10**, 1520-1525 (2002).

88. Schott Optisches Glas Catalog (1997).

89. Technical information “Optisches Glass” from Schott Glass company (1988).

90. Cargrille Labs data sheet.

91. K, J. Ranka, S.R. Windeler, and A. J. Stentz, “Visible continuum generation in air-silica microstructure optical fibers with anomalous dispersion at 800 nm”, Opt. Lett. **25**, 25-27 (2000).

92. J. Hansryd and P.A. Andrekson, “Broad-band continuous-wave-pumped fiber optical parametric amplifier with 49-dB gain and wavelength-conversion efficiency”, IEEE Photon. Tech. Lett., **13**, 194-196 (2001).

93. H. Takara, T. Ohara, K. Mori, K. Sato, E. Yamada, M.Abe, Y. Inoue, T. Shibata, T. Morioka, and K. I. Sato, “More than 1000 channel optical

frequency chain generation from single supercontinuum source with 12.5 GHz channel spacing", Electron. Lett. **36**, 2089-2090 (2000).

94. A. Ortigosa-Blanch, J. C. Knight, W. J. Wadsworth, J. Arriaga, B. J. Mangan, T. A. Birks and P. S. J. Russell, "Highly birefringent photonic crystal fibers", Opt. Lett. **25**, 1325-1327 (2000).
95. M. Lehtonen, G. Genty, H. Ludvigsen, and M. Kaivola, "Supercontinuum generation in a highly birefringent microstructured fiber", App. Phy. Lett. **82**, 2197-2199 (2003).
96. N. A. Issa, M. A. van Eijkelenborg, M, Fellew, F. Cox, G. Henry and M. C. J. Large, "Fabrication and study of microstructured optical fibers with elliptical holes", Opt. Lett. **29**, 1336-1338 (2004).
97. J. R. Folkenberg, M. D. Nielsen and C. Jakobsen, "Broadband single-polarization photonic crystal fiber", Opt. Lett. **30**, 1446-1448 (2005).
98. C. Yeh, "Elliptical dielectric waveguides", J. Appl. Phy. **33**, 3235-3243 (1962) .
99. R. B. Dyott, "*Elliptical Fiber Waveguides*", 1995, Artech House Publishers.
100. S. R. Rengarajan and J. E. Lewis, "Single-mode propagation in multi-layer elliptical fiber waveguides", Radio Science, **16**, 541-547, (1981).
101. N. W. Mclachlan, "Theory and application of Mathieu functions " , 1947, Clarendon Press.
102. Data sheet from *Thorlabs*.
103. J. K. Shaw, W. M. Henry, and W. R. Winfrey, " Weakly guiding analysis of elliptical core step index waveguides based on the characteristic numbers of Mathieu's equation," J. Lightwave Tech., **13**, 2359 (1995).
104. J. L. Huey and D. P. Beuther, "Method and apparatus for making non-circular mineral fibers", United States Patent 4622054, 1986.
105. T. M. Monro, K. M. Kiang, J. H. Lee, K. Frampton, Z. Yusoff, R. Moore, J. Tucknott, D. W. Hewak, H. N. Rutt, and D. J. Richardson, "High nonlinearity extruded single-mode holey optical fibers", Anaheim, CA, Postdeadline Paper FA1, 19-21, Mar. 2002.
106. C. Martelli, J. Canning, K. Lyytikainen, and N. Groothoff, "Water-core Fresnel fiber", Optics Express, **13**, 3890-3895, (2005).
107. M. Böhm, H. Hartwig, and F. Mitschke, "Präparation von mit Flüssigkeiten gefüllten mikrostrukturierten Glasfasern", Frühjahrstagung der DPG Berlin 2005, Q 29.2 (2005).

108. G. S. He and P. N. Prasad, “Stimulated Kerr scattering and reorientation work of molecules in liquid CS_2”, Phys. Rev. A, **41**, 2687–2697 (1990).

109. T. J. Bridges, A. R. Chraplyvy, J. G. Bergman, Jr., and R. M. Hart, “Broadband infrared generation in liquid-bromine-core optical fibers”, Opt. Lett. **7**, 566-568 (1982).

110. R. L. Sutherland, “Handbook of nonlinear optics”, (Marcel Dekker, Inc., New York, USA, 1996), pp. 457.

111. A. Samoc, “Dispersion of refractive properties of solvents: Chloroform, toluene, benzene, and carbon disulfide in ultraviolet, visible, and near-infrared”, J. of Appl. Phys. **94**, 6167-6174 (2003).

112. T. Birks, J. Knight, and P.St. J. Russell, “Endlessly single-mode photonic crystal fiber”, Optics Letters, **22**, 961-963 (1997).

113. T. P. White, R. C. McPhedran, L. C. Botten, G. H. Smith, and C. M. de Sterke, “Calculations of air-guided modes in photonic crystal fibers using the multipole method”, Optics Express, **11**, 721-732 (2001).

114. B. J. Eggleton, P.S. Westbrook, R. S. Windeler, S. Spalter, and T. A Strasser, “Grating resonances in air/silica micro structured optical fibers”, Optics Letters, **24**, 1460-1462 (1999).

115. M. Midrio, M. P. Singh, and C. G. Someda, “The space filling mode of holey fibers: an analytical vectorial solution”, J. Lightwave Technology, **18**, 1031-1037 (2000).

116. Y. Li , C. Wang, M. Hu, “ A fully vectorial effective index method for photonic crystal fibers: application to dispersion calculation”, Optics Communications, **238**, 29-33 (2004).

117. B. Kibler, J. M. Dudley, and S. Coen, “Supercontinuum generation and nonlinear pulse propagation in photonic crystal fiber: influence of the frequency-dependent effective mode area,” Appl. Phys. B, **81**, 337-342 (2005).

118. D. McMorrwo, W. T. Lotshaw, and G. A. Kenney-Wallace, “Femtosecond optical Kerr studies on the origin of the nonlinear responses in simple liquids”, IEEE J. Quantum Electron. **24**, 443-454 (1988).

119. B. F. Levine and C. G. Bethea, “Second and third order hyperpolarizabilities of organic molecules”, J. Chem. Phys., **63**, 2666-2682 (1975).

120. F. T. Arecchi and E. O. Schulz-Dubois, “Laser Handbook”, Volume 2, 1972, North-Holland Publishing Company.

121. I. A. Heisler, R. R. B. Correia, T. Buckup, and S. L. S. Cunha, “Time-resolved optical Kerr-effect investigation on CS_2/polystyrene mixtures”, J. Chem. Phys., **123**, 054509 (2005).

122. R. Zhang, J. Teipel, and H. Giessen, “Theoretical design of a liquid-core photonic crystal fiber for supercontinuum generation”, Opt. Express **14**, 6800-6813 (2006).

123. R. Zhang and H. Giessen, “Polarization maintaining tapered fiber”, submitted (2006).

Acknowledgments

To finish this doctoral work, I would like to thank many people. They gave me a lot of help not only in the research of my subject but also in the guidance to make my life in Germany full of happiness and success. I would like to take this opportunity to thank

- my supervisor Prof. Harald Giessen for providing me an opportunity to work in my favorate subject. The life working in his group was enjoyable. He gave me a lot of suggestions and fruitful discussions in the research, encouraged me to go further in physics, and friendly trained me to become an eligible scientific researcher
- Prof. John Dudley for many valuable discussions in the research and many important comments on my publications
- Prof. Hans Kroha for his very nice concern on my dissertation as the second Gutachter
- Xinping Zhang, Jörn Teipel, Hongcang Guo, Diana Türke, Dominc Meiser, Xiulun Yang, Anja Schönhardt, Sebastian Pricking, Felix Hoos for their really nice help both in my research and in my daily life. They provided me very friendly atmosphere, discussed with me on the problems in the reasearch, and taught me German as my second foreign language
- Prof. K. Buse and his group for help of measuring transmission curves with CARY spectrometer
- Prof. M. Griebel and his group for the supercomputer time
- Prof. A. Laubereau, Chris Milne, Prof. R. J. Dwayne Miller and Prof. L. Kaufman for the discussion of the response function of carbon disulfide
- all the colleague in our institute for their friendly help. Especially I would like to thank Herr Krause and his group for the technical support on my computers, which made my theoretical simulations much faster
- my husband Xin Guo and my parents for providing me a lot of support. They encouraged me when I felt frustrated and took good care of me when I was ill. Withouth them I could never lead such a happy life in my Ph. D study.